Chapter 1

Introduction

In the quest to move from the traditional dependence on fossil fuels for energy, the field of renewable and green (environmentally friendly) energy has received a lot of attention in the recent past. Within the many facets of renewable and green energy is solar energy that can be harnessed by the use of solar cells. Solar cells are largely divided into two types, namely inorganic (non-carbon based) and organic (carbon based).

This study focuses on the optimization and characterization of organic solar cells based on two semiconducting organic polymers, regio-regular poly (3-hexylthiophene), abbreviated as regio-P3HT or simply P3HT (conjugated polymer) and [6,6]-phenyl C_{61} butyric acid methyl ester, abbreviated as C_{60}-PCBM or simply PCBM (a fullerene). These two polymers are used as active layer materials to absorb the incident solar energy, which in turn excite the charge carriers within these semiconducting polymers. The excited charges are subsequently separated at the interface between the two polymers, and are then appropriately collected to provide the needed electric power for various applications. The need to meet the energy demand of the world cannot be overemphasized.

The subsections that follow looks at the amount of energy the earth receives from the sun and compares it with the world's future energy demand projection. Within the subsections is discussed the various parameters involved in the process of harnessing solar energy such as air mass and global solar energy distribution.

1.1 Global Energy Demand and Solar Energy

Many developing countries depend heavily on fossil fuels and hydro electricity for the provision of electrical power for both domestic and commercial use. However, fossil fuels are a diminishing resource whilst hydro electricity remains largely unavailable in many remote areas of these countries. There is therefore a need to search for an alternative clean and renewable source of energy that can be readily made available for both domestic and commercial applications. One possible source of clean and renewable energy is solar energy.

In photovoltaic cells, solar energy is harnessed by capturing sunlight in solar cells that convert photon energy into electricity. Solar cells can be made from both inorganic and organic materials. However, solar cells presently (2009) are made primarily from inorganic materials whilst organic solar cells are yet to break into commercial market. Because solar cells made from organic materials have not yet reached commercial level, it is not possible at the moment to make a comparison of the two based on commercial capital cost, because such literature is not yet available at the moment. However one can compare the two types of cells based on manufacturing method and mechanical properties.

The major hurdles hindering the commercialisation of organic solar cells are their low power conversion efficiency and rapid degradation compared to conventional inorganic based cells. In contrast to the traditional commercial inorganic solar cells, with power practical conversion efficiency of above 12 %, organic solar cells for a long time have been known to have practical efficiency of only up to 2.5 % [1, 2]. This is quite low compared with current inorganic solar cells, that are made chiefly from silicon and gallium arsenide, with theoretical and practical efficiency of about 33 % and above 12 % respectively [3, 4]. Fabrication using these inorganic materials is however costly often requiring very expensive clean processes. Additionally, the solar cells tend to be heavy and rigid. The high cost involved in manufacturing the

traditional inorganic solar cells make them unaffordable by most people, as it makes use of solar energy capital intensive.

Recent statistics has shown that solar energy is at an average cost of about 20 to 25 cents per kWh compared with 8 cents per kWh for hydro electricity [2, 5]. In order to reduce the high cost associated with traditional solar cells, current research is focusing on materials that are cheap to fabricate, light in weight, flexible, with long life span, less toxic in manufacturing, and have photo-efficient sufficient for commercial purposes. Organic materials for manufacturing organic solar cells meet most of these requirements with the exceptions of high power conversion efficiency and long life span. Therefore recent research in the development of organic solar cell is concentrating on improving the efficiency of these solar cells and reducing degradation [2, 4].

1.2 Air Mass and Solar Energy Distribution

The amount of energy that the Earth's atmosphere receives from the sun is enormously at 1.75 x 10^{17} W per hour. The world energy consumption is projected at 5.1 x 10^{20} J (1.61 x 10^{13} W) for the year 2010. Thus the Earth receives enough energy to fulfil the world's yearly demand of energy in less than an hour [6 - 8]. However, not all of that energy reaches the Earth's surface due to atmospheric attenuations through absorption and scattering. The atmosphere attenuates the solar radiation before it reaches the earth's surface mainly through water vapor which absorbs solar radiation in the infra-red region, the ozone layer which absorbs radiation in the ultraviolet region, dust and aerosols which scatter the radiation in the visible region. This problem of energy loss is further compounded by the low power conversion efficiency exhibited by solar energy converters such as photovoltaic cells.

1.2.1 Air Mass (AM)

The degree to which the atmosphere attenuates solar radiation is determined by the *air mass*. Air mass is the measure of the atmospheric path length of

the sun relative to the minimum path length when the sun is directly overhead as depicted by Figure 1.1.

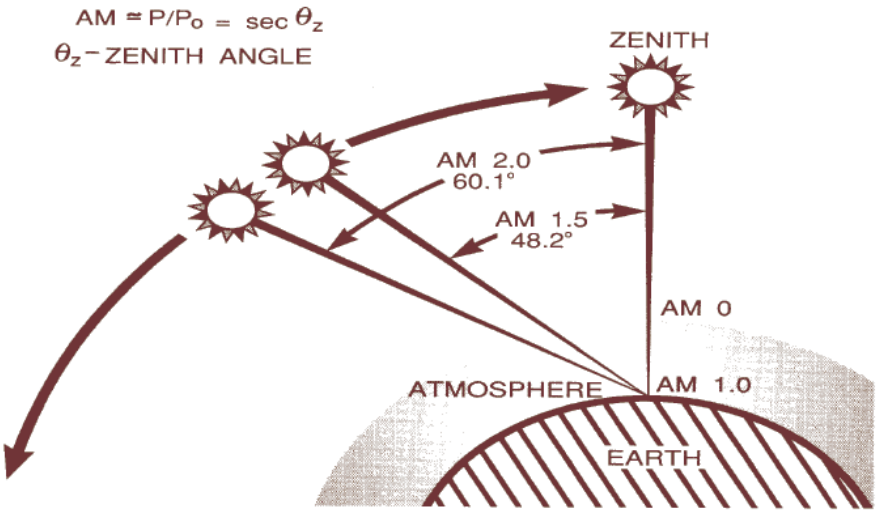


Figure 1.1: AM measurements showing angles of sun's position relative to the vertical [9]

AM is basically divided into 4 levels, namely AM 0, AM 1, AM 1.5, and AM 2. It is expressed as the secant of the angle between the zenith and the position of the sun in the sky as shown in the equation below [9 - 12].

$$Sec(\theta) = 1/Cos(\theta) \qquad (1.0)$$

The Air Mass value is then expressed as

$$AM\ \ Sec(\theta) \quad \text{or} \quad AM\ \ 1/Cos(\theta)\ ) \qquad (1.1)$$

For example, for θ = 0 °, at zenith, Sec (0 °) = 1, hence the AM value is expressed as AM 1. One of the easiest way to estimate the AM in practice is to measure the length of the shadow (*s*) cast by a vertical structure of height (*h*) using the equation below.

$$AM = \sqrt{1-(s/h)^2} \qquad (1.2)$$

The larger the value of the AM, the more the atmospheric attenuation on the solar radiation and the weaker the radiation received. The AM 0 spectrum is only relevant for satellite and space-vehicle applications while the AM 1 spectrum represents the radiation at the earth's surface when the sun is exactly at zenith i.e. when $\theta = 0\ ^\circ$ with incident power of 925 W/m^2. The AM 1.5 conditions (sun at 48.2 $^\circ$ above the horizon as in Figure 1.1) represent a satisfactory energy-weighted average for terrestrial applications. The total incident power for AM 1.5 is 844 W/m^2. On the other hand The AM 2 spectrum is for $\theta = 60\ ^\circ$ and has an incident power of about 691 W/m^2.

Figure 1.2 shows four curves related to solar spectral irradiance (power per unit area per unit length) as function of wavelength. The curves show maximums occurring in the visible region for each level of AM. The highest spectral irradiance being observed at AM 0 and the lowest at AM 2 with the irradiance for AM 1.5 in-between (not shown in Figure 1.2). These have corresponding spectral incident powers of 1353, 925 and 691 W/m^2 respectively. The earth's outer atmosphere is at AM 0 and is equivalent to the extraterrestrial spectral radiation with a power per unit area given by the solar constant of about 1353 W/m^2 and can be approximated by a 5800 K black body temperature as shown by the dashed-dotted curve.

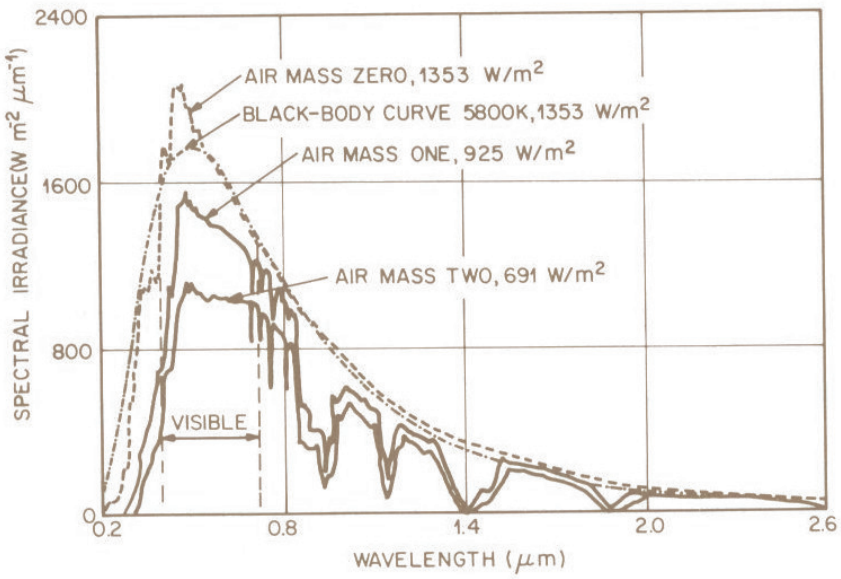


Figure 1.2: Four curves related to solar spectral irradiance [10].

1.2.2 Solar Energy Distribution

For effective solar energy utilization, it is necessary to know how much solar energy is expected during the year in various locations. The worldwide distribution of solar energy in terms of sunshine duration (also known as insolation) is shown in Figure 1.3. The bold contour lines enclose regions that receive an average of about 8 or more hours of sunshine daily. Since all continents have sufficiently large areas covered by high average insolation, it can be anticipated that there shall be extensive worldwide utilization of solar energy in the future. It is also clear from Figure 1.3 that the continent of Africa receives the highest amount of solar energy. This therefore presents a large opportunity for utilization of solar energy for photovoltaic applications in Africa.



Figure 1.3: Worldwide distribution of solar energy in terms of sunshine duration. The contours refer to insolation in hundreds of hours per year [10].

Figure 1.4 shows the two types of air masses at 1.5 and the major atmospheric attenuation factors representing the direct and global AMs. The atmosphere attenuates solar radiation mainly through water vapor which absorbs solar radiation in the infra-red region, while the ozone layer absorbs radiation in the ultraviolet region. Additional loss of solar radiation occurs through scattering by dust and aerosols in the visible region. The

standardised terrestrial spectra for direct and global sunlight are shown in Fig.1.4 where the global spectra comprises the direct *plus* the diffuse components. The diffuse component generally has a different spectral composition from that of direct in that it is richer in the shorter (blue) wavelengths whereas the direct is richer in longer (red) wavelengths.

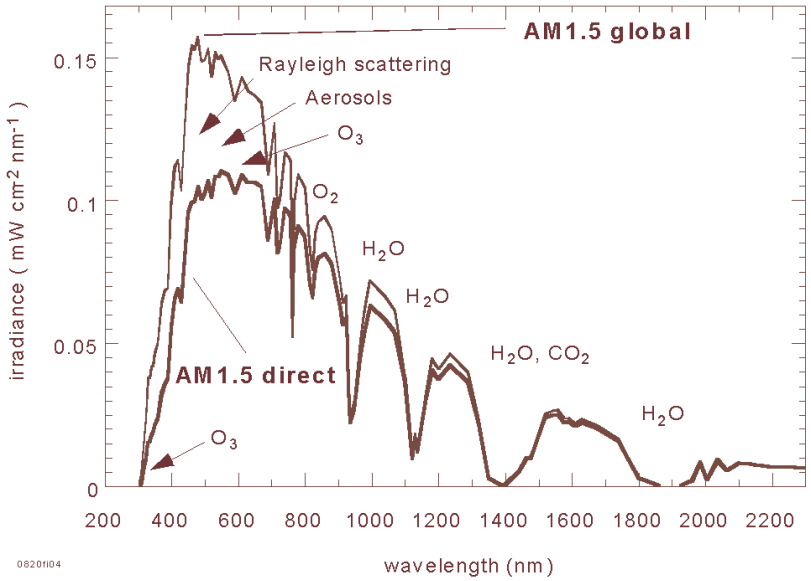


Figure 1.4: The spectra of AM1.5 direct and AM1.5 global, and the light scattering molecules [10].

The difference between direct and global sunlight occurs mainly in the shorter wavelength region because molecular scattering scales up proportionally to λ^4. The main attenuators of solar radiation in the Earth's atmosphere are water molecules (H_2O), ozone (O_3) and carbon dioxide (CO_2).

The fraction of diffuse radiation received by a horizontal surface can go up to between 10 to 20 % even in clear cloudless skies. For completely covered skies most of the radiation will be diffuse. Hence, for days between the sunny and cloudy extremes mentioned above, about 50 % of the solar radiation will be diffuse.

(eV) :	4.1	3.5	3.1	2.8	2.5	2.3	2.1	1.9	1.8	1.7	1.6	1.5	1.4	1.3	1.24	1.18	1.13	1.08	1.03	0.99	0.95	0.69	0.62	0.5
(nm):	300	350	400	450	500	550	600	650	700	750	800	850	900	950	1000	1050	1100	1150	1200	1250	1300	1800	2000	2500
300	0	0.7	2.9	7.6	14	21	28	35	42	48	54	59	64	67	70	74	77	79	81	84	86	96	96	100
350		0	2.2	6.9	14	21	28	35	41	47	53	58	63	66	69	73	77	78	80	83	85	95	96	99
400			0	4.7	11	18	25	33	39	45	51	56	61	64	67	71	74	76	78	81	83	93	93	97
450				0	6.7	14	21	28	34	40	46	51	56	59	62	66	70	71	73	76	78	88	89	92
500					0	7.0	14	21	28	34	39	44	50	52	56	60	63	64	67	69	72	81	82	86
550						0	7.1	14	21	27	32	37	42	45	49	53	56	57	60	62	65	74	75	79
600							0	7.1	14	20	25	30	35	38	42	46	49	50	52	55	58	67	68	72
650								0	6.5	13	18	23	28	31	35	39	42	43	45	48	51	60	61	65
700									0	6.1	12	17	22	25	28	32	35	37	39	42	44	54	54	58
750										0	5.6	11	16	19	22	26	29	30	33	35	38	48	48	52
800											0	5.1	10	13	16	20	24	25	27	30	32	42	43	46
850												0	5.1	8.0	11	15	19	20	22	25	27	37	37	41
900													0	2.9	6.3	10	13	15	17	20	22	32	32	36
950														0	3.3	7.3	11	12	14	17	19	29	29	33
1000															0	3.9	7.2	8.4	11	13	16	26	26	30
1050																0	3.2	4.5	6.8	9.5	12	22	22	26
1100																	0	1.2	3.5	6.2	8.7	18	19	23
1150																		0	2.3	5.0	7.5	17	18	21
1200																			0	2.7	5.2	15	15	19
1250																				0	2.5	12	13	16
1300																					0	10	10	14
1800																						0	0.5	4.3
2000																							0	3.8
2500																								0

solenergy.xls

Figure 1.5: Distribution of energy (in percent) within the AM1.5d spectrum at various wavelengths [10].

Figure 1.5 shows the distribution of energy within AM1.5 diffuse spectrum at various wavelength. For a solar cell, for example silicon cell, with a band gap of 1.13 eV (1100 nm) can maximally absorb 77 % of the terrestrial solar energy. Taking into account the region with the highest energy content (400-900 nm, see values in the diagonal) a material with a band gap of 1.4 eV can only absorb up to 61 % of the terrestrial solar radiation or 80 % of the value for silicon [12 - 14].

1.2.3 Simulation of Solar Radiation

The ultimate method to test the overall performance of solar cells is outdoor exposure. From the preceding section, however, it has been shown that outdoor conditions vary from one location to the other and from time to time. Therefore, in order to produce reliable and reproducible results, solar simulators whose illumination conditions are designed to match an internationally standardised solar spectrum must be used. Commercially available solar simulators usually use a xenon arc lamp in conjunction with a spectral correction filter which approaches the terrestrial solar spectrum that it is good enough for many applications [13 - 15]. A simulator based on a quartz tungsten halogen-lamp (QTH) can be used as a much cheaper alternative to the expensive xenon lamp.

Chapter 2

Properties and Processes in Organic and Inorganic Semiconductors

Due to the strong electron-phonon interaction in organic materials the photo-physics in this class of materials is often different compared to the inorganic semiconductors and not yet fully understood [10, 16]. The formation of excitons in the process of photo-conversion is one of the main differences between inorganic and organic based solar cells. Photo-absorption is influenced by macroscopic properties of the material whereas the second step is related to the materials band gap. Excitons are strongly bound in organic photovoltaics with energies of about 0.1 – 1.4 eV. Photo-conversion in organic solar cells follows four major steps comprising absorption of incident photons, generation of excitons, dissociation of excitons into free charge carriers, and transport of free charge carriers.

The excitons need to be split up (or dissociated) before the charges can be transported through the film and collected at the electrodes. Exciton dissociation can occur at a rectifying interface (Schottky contact) in single layer devices or at the interface between an electron-donor and an electron-acceptor semiconductor material in a bulk hetero-junction (BHJ). The larger the interface, the more the excitons reaching it and the more the dissociation will occur. In addition, the small diffusion range of the excitons (typically about 8 - 10 nm) compared to the film thickness necessary to absorb the major portion of light (typically > 100 nm) has made it difficult to reach high conversion efficiencies in organic solar cells [16, 17]. Thus, any effort to increase the efficiency of organic solar cells must attempt to address the factors discussed in the preceding section. Factors that are important to solving these problems are discussed in the sections that follow.

2.1 p-Type and n-Type Organic Semiconductors

A semiconductor can basically be in one of two forms, p-type and n-type. In p-type the majority carriers are holes whereas in n-type the majority carriers are electrons. Alternatively, the semiconductor can also be described in terms of Fermi level.

2.1.1 Fermi-level

The energetic position of the Fermi-level in semiconductors is important for two reasons.

(1) Together with the work function of the metal the Fermi level determines whether a blocking or ohmic contact is formed at the semiconductor/metal interface.
(2) The relative position of the Fermi level is a measure for the type of conductivity, whether the semiconductor conducts preferably holes in the valence band (VB) resulting in p-type or electrons in the conduction band (CB) resulting in n-type semiconductors.

The energetic position of the Fermi level (E_F) in a semiconductor represents the balance between the concentration of holes and electrons that occupy allowed energy levels under equilibrium condition (dark, no applied voltage). If the Fermi-level is closer to the CB the material is called n-type conductor since more electrons are available for conduction than holes. Otherwise it is called p-type conductor. The position of the Fermi level can be written as a function of both the effective density of states in the conduction band N_C and valence band N_V as well as the concentration of donors N_D and acceptors N_A respectively. For n-type semiconductors this gives the following equation [17, 18].

$$E_F = E_C . k_B T . Ln(\frac{N_C}{N_D}) \qquad (2.1)$$

Whereas for p-type semiconductors the relation is

$$E_F = E_V . k_B T . Ln(\frac{N_V}{N_A}) \qquad (2.2)$$

E_V and E_C stand for the top edge of the VB and the bottom edge of the conduction band respectively. k_B is the Boltzmann constant and T is the ambient temperature.

When voltage is applied and/or the semiconductor is illuminated, the concept of a single Fermi level can no longer be applied. Upon illumination, for example, the increased concentration of electrons in the CB would shift E_f up while the higher concentration of holes in the VB shifts E_f down at the same time. As a consequence two separate Fermi levels, referred to as *quasi* Fermi-levels. The situation under this non equilibrium condition is represented by the following equations [17, 18]:

$$E_{FN} = E_C + k_B T . Ln(\frac{n}{N_C}) \qquad (2.3)$$

and

$$E_{FP} = E_V + k_B T . Ln(\frac{N_V}{p}) \qquad (2.4)$$

where n and p denote the concentration of electrons in the CB and holes in the VB respectively. E_{FN} and E_{FP} are the quasi Fermi-levels that are associated with the balance of electrons and holes, both exist at the same time in one semiconductor.

2.1.2 Doping in Semiconductors

The conductivity of certain semiconducting materials can be raised by addition of electrons (in a process referred to as reduction) or removal of electrons (in a process referred to as oxidation), achieved by the introduction of foreign

atoms into the semiconducting material. The deliberate controlled addition of foreign atoms or molecules into a semiconducting material is referred to as doping. The doping of an organic polymer achieves the same result as that of doping of a classical inorganic semiconductor, in that very large increase in conductivity is observed when the material takes up very small amounts of certain chemical species. For example the conductivity of polyaniline (PANI) increases when doped with small amounts of an acid, whilst the conductivity of silicon increases when doped with small amounts arsenide. The doping process, however, is different.

In inorganic semiconductors doping occurs via the introduction of dopant atoms that provide additional free charge carriers at room temperature so that the extra charges increase the conductivity for this type of semiconductor. The Fermi level is moved towards the CB if extra electrons are introduced or towards the VB if the concentration of mobile holes has been increased.

For organic semiconductors the mechanism is different in that the doping of an organic polymer involves simply the partial oxidation or reduction of the polymer. Each oxidation state exhibits its own characteristic reduction potential. The doping material (dopant) ion incorporated may be derived from the chemical species to be doped or it may be completely unrelated to it [18].

2.1.3 Polymer Blending

Conductivity of polymers can be increased by blending of different polymers and is synonymous to doping in inorganic materials. It is also an alternative approach to obtaining new materials with desirable properties based on the available polymers rather than designing and synthesizing completely new ones. Polymer blending can be used to fine-tune properties of polymeric materials and enhance their range of usefulness by bringing together the properties of different polymers. Besides increasing conductivity, polymer blending can impart improved processability, impact strength, resistance to

solvents and chemicals [18]. Polymer blending is therefore an important technique to achieving desirable properties in organic devices including organic solar cells.

2.1.4 Conjugated polymers

Conjugated polymers are polymers with alternating single and double bonds (Figure 2.1). Single bonds are known as sigma (σ) bonds whilst double bonds are known as Pi (π) bonds. In the conjugated system, the σ-bonds are formed by the overlap of sp^2 hybrid orbitals on the carbon atom with the remaining out of plane P_z overlapping to form π-bonds [2, 19 - 20]. In the backbone of a conjugated polymer, each carbon atom bonds to only three adjacent atoms, leaving one electron per carbon atom in a P_z orbital. The π-bonds along the conjugated backbone cause the delocalisation of the π electrons on the entire conjugation path. The mutual overlap between these P_z orbitals results in the formation of a bonding (π-orbital) and anti-bonding (π^*-orbital). The π-orbital forms the lower energy band called the highest occupied molecular orbital (HOMO) whilst the π^*-orbital forms the higher energy band which is called the lowest unoccupied molecular orbital (LUMO). The delocalized π electrons fill up the HOMO levels and, therefore, conjugated polymers are intrinsic semiconductors.

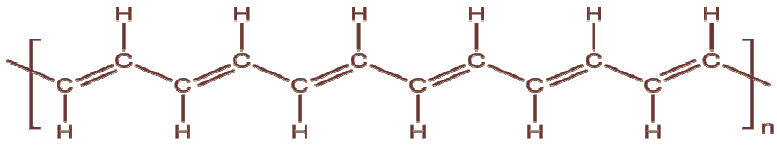


Figure 2.1: In polyacetylene the bonds between adjacent carbon atoms are alternating single and double [20].

The structure in the π- system can be excited without affecting the sigma bonds in the polymer structure. Therefore, it is possible to promote an electron from the HOMO to the LUMO level upon, for example, through photo absorption of light. As the band gap (energy difference between the HOMO and LUMO) of a conjugated system depends on the system's arrangement and orderliness, any disturbance of the conjugation along the polymer's

backbone will change the local HOMO and LUMO positions. Real conjugated polymers are therefore subject to energetic disorders due to molecular disturbances. The density of states of these systems is often approximated by a Gaussian distribution [2, 19 - 22].

2.1.5 Exciton Creation and Dissociation in Polymers

An exciton is an electrically-neutral electron-hole pair created upon excitation of an electron across the band gap in a semiconductor following photon absorption. The excitons must be dissociated to generate free charge carriers. One of the main differences between inorganic and organic semiconductors (here conjugated polymers) is the magnitude of exciton binding energy that must be overcome to dissociate them.

For most inorganic semiconductors the exciton binding energy is small compared to the thermal energy at room temperature (k_BT~25 meV). Therefore, excitons readily dissociate thereby generating free charges are under ambient conditions. On the other hand organic semiconductors typically have exciton binding energies exceeding the thermal energy at room temperature by a large magnitude. Consequently, excitons formed upon excitation do not readily dissociate into free charges. This fundamental difference between inorganic and organic semiconductors is of critical importance for the design of organic based PV devices. Whereas in conventional, inorganic solar cells free charges are created upon light absorption, organic solar cells need an additional mechanism to dissociate the excitons [12]. This is an important factor to be considered in increasing the photo-conversion efficiency of organic solar cells.

A successful technique to dissociate excitons in organic semiconductors is at a donor/acceptor heterojunction interface. This interface is formed between two organic semiconductors with dissimilar valence (VB) and conduction (CB) bands. If an exciton is created in the donor and reaches the donor/acceptor interface, the electron will be transferred to the acceptor material and the hole

will recede in the donor material (similarly, a hole will be injected in the donor material after excitation of the acceptor material).

An exciton created in either the donor or acceptor will reach the interface within its lifetime only if it is created within a slab of material around the interface with a thickness less than the exciton diffusion length, which is limited to about 10 nm for organic semiconductors. Since the absorption coefficient of most of these organic semiconductors is ~10^{7} m^{-1}, a layer of 100-300 nm is required to absorb all the visible light [12]. In order to solve this dilemma, efficient polymer solar cells require a nano-scale interpenetrating bicontinous network of donor/acceptor materials within the whole photoactive layer. This ensures an efficient dissociation of photo-generated excitons and transport of the charges to the electrodes.

A typical BHJ system that has received much attention is the poly (3-hexylthiophene-2, 5- diyl) (P3HT): [6, 6] Phenyl-C_{61}-butyric acid methyl ester (C_{60}-PCBM) blend system. In P3HT: C_{60}-PCBM blend based BHJ OPV cells energy is absorbed mostly by the conjugated polymer (P3HT) which has smaller band gap (Eg ≈ 2.0 eV). The fullerene (PCBM) has larger band gap of about 2.5 eV making its absorption to be narrowed mainly to the ultraviolet region. After light is absorbed, excitons must get to the interface between the two semiconductors to dissociate into free electrons and free holes. In P3HT: C_{60}-PCBM blend excitons are formed right at the interface. Exciton diffusion is therefore not a limiting factor on the performance of the cells. In many other non-blended OPV cells such as bilayers, excitons should reach the interface within their diffusion length to dissociate otherwise they decay off to their ground states. For this reason exciton diffusion is a very important process to understand and optimize for both blended and non-blend devices.

2.1.6 Transport of Charges in Conjugated Polymers

Since polymers do not have a three dimensional periodical lattice structure, charge transport in polymers cannot be described by standard semiconductor

models. As these systems show energetic and spatial disorder, the concept of band conduction of free charge carriers does not apply. In this section, a summary is given of how charge carrier transport in conjugated polymers and similar materials is determined theoretically and its methods of experimental characterisation.

The field of molecularly doped polymers is much older than that of conjugated polymers and valuable insights can be gained from studying this field. As early as in the 1970s the charge transport in molecularly doped polymers was studied by performing time-of-flight (TOF) measurements [6, 23 - 24]. In this type of experiment, a sample is sandwiched between two non-injecting electrodes and short light pulse is used to illuminate one side of the sample through a transparent electrode. Under the action of an applied field, charge carriers of the same electrical polarity as the illuminated electrode will traverse the sample. By monitoring the current flow in the external circuit, the charge carrier mobility can be determined as a function of the applied voltage. In these TOF experiments the mobility, μ, of carriers in molecularly doped polymers can empirically be described by the equation below [25].

$$\mu = \mu_0 \exp(\Upsilon\sqrt{F}) \qquad (2.5)$$

where μ_0 is the zero-field mobility, F is the field strength, and Υ is the field activation parameter.

2.1.7 Hopping transport in Conjugated Polymers

Since organic materials are disordered, the concept of band conduction does not apply in explaining their conductivity. Instead, localized states are formed and charge carriers proceed from one such a state to another (*hopping*), thereby absorbing or emitting phonons to overcome the energy difference between those states as shown by Figure 2.2 (A) and (B).

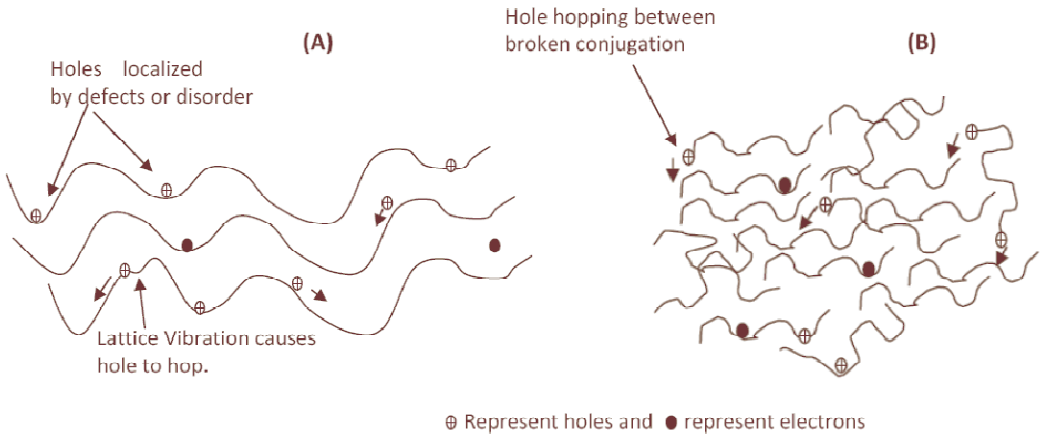


Figure 2.2: (A) hopping transport of charge carriers through lattice vibration, and (B) broken conjugation producing defects in the polymer system. [26]

Conwell and Mott proposed the concept of hopping conduction in 1956 to describe impurity conduction in inorganic semiconductors [6, 27 - 28]. Miller and Abrahams calculated that the transition rate W_{ij} for phonon-assisted hopping from an occupied state i with an energy ε_i to an unoccupied state j with energy ε_j is described by [29, 30]

$$W_{ij} = \upsilon_o \exp(-2\gamma R_{ij}) \begin{cases} \exp(-\dfrac{\varepsilon_j - \varepsilon_i}{k_B T}) & \varepsilon_i < \varepsilon_j \\ 1 & \varepsilon_i \geq \varepsilon_j \end{cases} \qquad (2.6)$$

where υ_0 is the attempt-to-jump frequency, R_{ij} is the distance between the states i and j, γ is the inverse localization length, k_B is Boltzmann's constant, and T is ambient temperature. The wave function overlap of states i and j is described by the first exponential term in Equation. (2.6), while the second exponential term accounts for the temperature dependence of the phonon density.

The hopping rates between sites are assumed to obey Equation. (2.6) and the site energies vary according to a Gaussian distribution with a standard deviation σ. Such a system of equations cannot be solved analytically. By

performing Monte Carlo simulations, the following expression for the charge carrier mobility μ was proposed [24, 25].

$$\mu = \mu_\infty e^{-(\frac{2\delta}{3k_BT})^2} \begin{cases} \exp\left(C\left[(\delta/k_BT)^2 - \Sigma^2\right]\sqrt{F}\right) & \Sigma \geq 1.5 \\ \exp\left(C\left[(\delta/k_BT)^2 - 2.25\right]\sqrt{F}\right) & \Sigma < 1.5 \end{cases} \quad (2.7)$$

where μ_∞ is the mobility in the limit $T \rightarrow \infty$, C is a constant that is related to the lattice spacing, and Σ describes the positional disorder. Although Equation. (2.7) predicts a functional dependence on field strength similar to Eq. (2.5), the agreement with experiments is limited to high fields. It has been found that the agreement with experiments could be improved by taking spatial correlations between site energies into account. In this model, the mobility takes the form indicated in Equation (2.8) [31 - 33].

$$\mu = \mu_\infty \exp\left[-\left(\frac{3\delta}{5k_BT}\right)^2 + 0.78\left(\left(\frac{\delta}{k_BT}\right)^{3/2} - \Gamma\right)\sqrt{\frac{qaF}{\delta}}\right] \quad (2.8)$$

Where q is the elementary charge, a is the intersite spacing, F is the field strength, δ is Gaussian distribution standard deviation, k_B is Boltzmann constant, T is temperature in degrees Celsius, and Γ is the positional disorder of transport sites. Since Equation (2.8) is an expression which describes the outcome of Monte Carlo simulations, this is a purely mathematical definition of μ_∞ and does not mean that it has the physical meaning of the mobility at infinite temperature. At best, it may be interpreted as the mobility if there were no barriers to hopping at all. This model was successfully used to describe the transport of charges in molecularly doped polymers [34]. Subsequently Equation (2.8) was also applied successful to explain the charge transport in conjugated polymers systems such P3HT/PCBM as well as other organic systems [20, 35 - 36]. In the foregoing discussion, only the dependence of the mobility on temperature and field strength was taken into account.

Increasing the applied voltage in a TOF experiment generally only changes the field across the sample. However, in organic solar devices such as organic solar cells, changing the applied voltage does not merely change the field. It influences the charge carrier density as well as a result of the nature of the contacts. Recently, it has been shown that the mobility of charge carriers in conjugated polymers also has a significant dependence on charge carrier density [37, 38]. Moreover, it was observed that the increase of the mobility with increasing bias voltage (and concomitant increase in carrier density) in polymer diodes is, at least for some systems and temperatures, completely due to an increase in charge carrier density. Throughout this thesis, the increase of the mobility with increasing bias voltage is interpreted as an effect of the field only.

Several alternative models exist for explaining charge transport. One of them is based on the polaron model which was first applied to inorganic crystals and later to conjugated polymers [39]. An excess charge carrier in a solid causes a displacement of the atoms in its vicinity thus lowering the total energy of the system. This displacement of atoms results in a potential well for the charge carrier thereby localizing it. The charge carrier and its concomitant atomic deformation are called a polaron. The transition rate for polaron hopping from site *i* to site *j* is given by [40].

$$W_{ij} \propto \frac{1}{\sqrt{E_r T}} \exp\left(- \frac{\left(E_j - E_i + E_r \right)^2}{4 E_r k_B T} \right) \qquad (2.9)$$

E_r is the intramolecular reorganization energy, k_B is Boltzmann's constant, and T is the ambient temperature. The resulting charge carrier mobility is of the form

$$\mu = \mu_0 \exp\left[-\left(\frac{E_r}{4 k_B T} \right) - \frac{(aF)^2}{4 E_r k_B T} \right] \frac{\sinh(aF / 2 k_B T)}{aF / 2 k_B T} \qquad (2.10)$$

The polaron contribution to the activation of the mobility predicted by this model is rather low and is typically in the range 25–75 meV, which is much smaller than the activation due to disorder [20].

2.2 Free Charge Carrier Collection

After the photo - excitons dissociate, free electrons and free holes are formed in a BHJ system. The holes are transported via the hole-transporting conjugated polymer (in this case, P3HT) and the electrons via the electron-transporting fullerene (in this case, C_{60}-PCBM) as shown in Figure 2.3. The free charges travel by a combination of drift velocity and diffusion. Drift velocity is influenced by the symmetry in the work functions of the different electrodes. Since the cathode (aluminium in this case) has a lower work function (≈ 4.2 eV) compared to the anode (ITO) with work function of ≈ 4.8 eV, the electrons will preferably drift to the lower work function aluminium cathode and the holes towards the higher work function ITO anode (Figure 2.4).

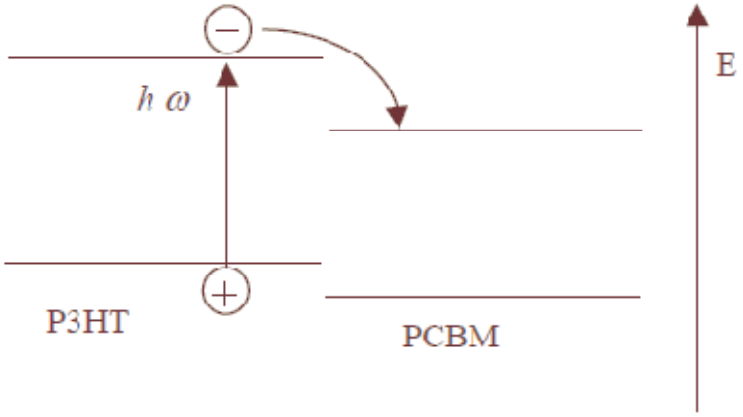


Figure 2.3: Exciton dissociation at the P3HT: PCBM interface due a difference in LUMO levels. Positive circle represents a hole while a negative circle represents an electron. $h\omega$ is the absorbed photon energy by an electron, and **E** represents energy levels.

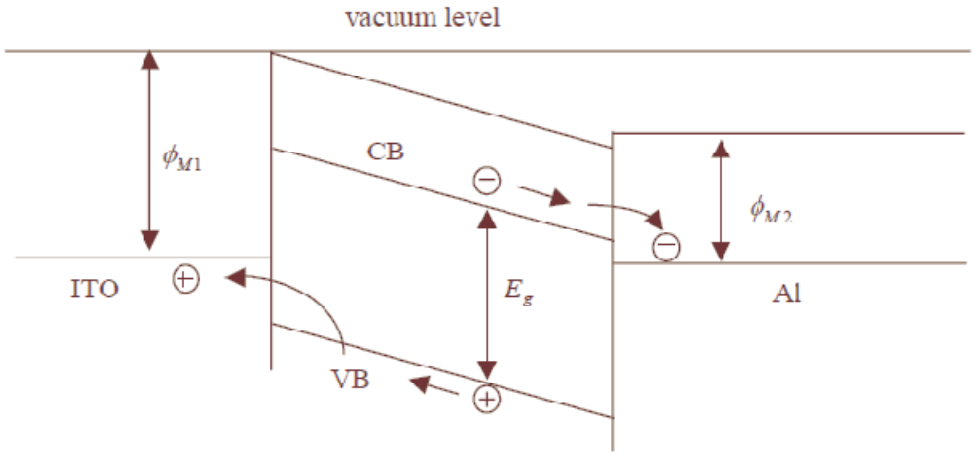


Figure 2.4: Transport of free charges in P3HT: PCBM BHJ to the electrodes. ϕ_{M1} and ϕ_{M2} are work functions of metal 1(ITO) and 2 (AL), respectively. CB and VB are conduction and valence bands, respectively. E_g is the band gap.

To further lower down the work function of the cathode, in this study, magnesium (Mg) thin film (100 nm) with a work function ≈ 3.8 eV is coated on aluminium. Silver (Ag) thin film (60 nm) with work function ≈ 4.6 eV is then coated on top of Mg to protect Mg from forming an oxide while the ITO surface is coated with a thin layer of PEDOT: PSS with work function of ≈ 5.2 eV to increase anode work function. An additional layer of TiO_2 is coated on top of the Ag layer to act as a hole blocking layer.

2.3 General Considerations of Photovoltaic (PV) Cells

The theoretical overview of PV cells helps us understand the working mechanisms of the cells at both small and large scales levels. It also assists in understanding the parameters that can be manipulated or altered to influence the performance of the cells. Furthermore, It allows knowledge of the hard limits of performance of these devices.

This chapter looks at the general operations of both inorganic and organic solar cells. It looks at the donor/acceptor interface and the resulting Schottky barrier at this interface. It further explores the method of determining the power conversion efficiency and solar cell modelling through the metal-insulator-metal (MIM) model. The chapter ends by looking at the strategies

aimed at improving the performance of the OPV, a review of literature, the aims and objectives of the experiments to be carried out within these strategies.

2.3.1 Inorganic Photovoltaic (IPV) Solar Cells

At present (2009), solar cells comprising an inorganic semi-conductor such as mono- and multi-crystalline silicon have found markets for small scale devices in everyday life such as solar panels on roof tops, water pumps and pocket calculators. These conventional solar cells can harvest light up to 24 % of the incoming solar energy which is close to the theoretically predicted upper limit of 30 %.

Despite these high conversion levels, IPV solar cells are associated with high costs of production. Hence technologies which enable for low fabrication costs and yet have high conversion efficiencies are desired. Currently, the production of inorganic solar cells still require many energy intensive processes taking place at high temperatures (400-1400 $^{\circ}$C) and high vacuum conditions with numerous lithographic steps. These combined factors lead to relatively high manufacturing costs [17, 41 - 42]. Since the technology is well established, it is unlikely that any major changes can be made to alter the techniques to substantially reduce the fabrication costs.

2.3.2 Organic Photovoltaic (OPV) Solar Cells

There are several approaches being attempted by researchers to produce cheaper and more efficient solar cells [43, 44]. For example, electro-chemical solar cells using titanium dioxide in conjunction with an organic dye and a liquid electrolyte already exceeded 6 % power conversion efficiencies and are about to enter the commercial market because of their relatively low production costs. Another type of organic solar cells is given by the semi - conducting polymers, which combine the opto-electronic properties of conventional semiconductors with the good mechanical and processing properties associated with polymeric materials. These can be processed from

solution at room-temperature onto flexible substrates using simple and cheaper deposition methods such as spin or blade coating [26, 45]. The advantage of polymeric photovoltaic cells when compared to electro-chemical cells is predominantly the absence of a liquid electrolyte, which creates problems of sealing against leakages.

In contrast to many inorganic semiconductors, in which photon absorption directly produces free electrons and holes, optical absorption in organic molecular and polymer semiconductors mainly creates electron-hole pairs (excitons) that are bound at room temperature (see section 2.1.5). In BHJ photovoltaic cells the creation of free electrons and holes is accomplished by the spontaneous dissociation of the excitons at the donor/acceptor interface. Subsequent transport and collection of the photo-induced charges at the appropriate electrodes then provides the required electric field polarity [46, 47]. Considerably less effort and production energy is necessary if organic semiconductors are used because of simpler processing at much lower temperatures (20 – 200 ^{o}C) than the above mentioned inorganic cells.

2.3.3 Charge Generation in OPV Cells

Understanding of the several processes that lead to generation of free charge carriers is important to increasing the photo-conversion efficiency of organic solar cells. Figure 2.5 shows the solar energy conversion steps following photon absorption, charge generation and separation as it takes place in an organic solar cell. The conversion steps in photon absorption leading to the creation of bound electron-hole pairs (excitons) rather than free charges are shown. The symbols in the brackets represent the equivalent loss mechanisms as used in ordinary equivalent circuit diagrams (ECD).

The excitons carry energy but no net charge and may diffuse to dissociation sites where their charges can be separated. Recombination of excitons presents a major loss mechanism that occurs during the diffusion process following charge separation. The separated free charges need to travel to the

respective device electrodes. Holes move to the anode whilst electrons move to the cathode to provide the electric field polarity and become available for injection into an external circuit. The individual steps affecting conversion efficiency in organic solar cells is discussed in details in the sections that follow.

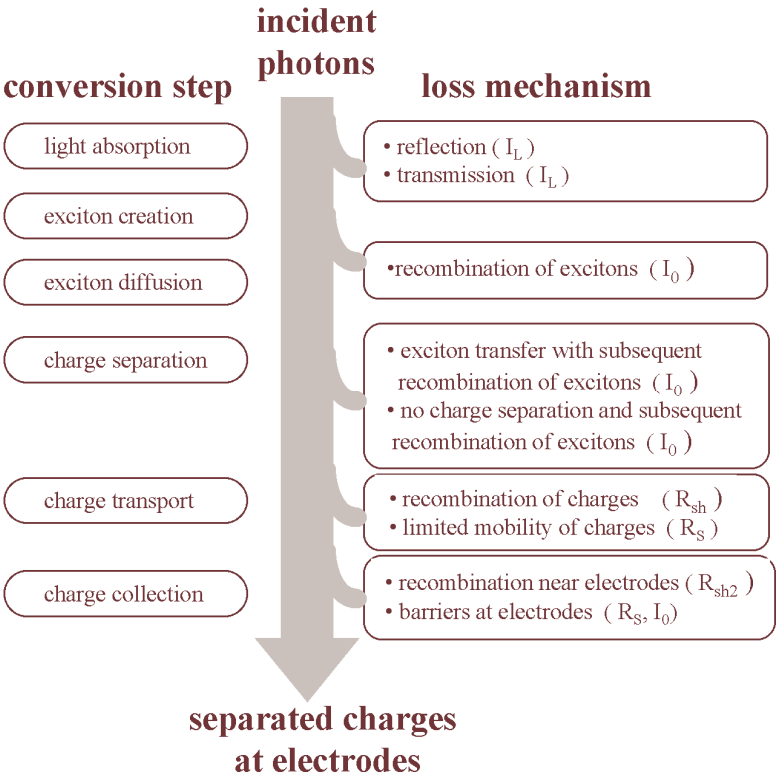


Figure 2.5: Specific conversion steps and loss mechanisms in an organic solar cell. The symbols in brackets represent the quantities that allow for the specific loss mechanism in the ECD [48]. I_0 represents zero current, I_L is the light current, Rs is series resistance and R_{sh} is shunt resistance.

2.3.4 Absorption of photons

In most organic devices only a small portion of the incident light is absorbed for the following reasons. Firstly, the semiconductor band gap is too high. A band gap of 1.1 eV (1100 nm) is required to absorb 77 % of the solar radiation on earth (Figure 1.5) whereas the majority of semiconducting polymers have Band gaps higher than 2.0 eV (600 nm) limiting the possible absorption to about 30 %. Secondly, the typically low charge carrier mobility requires layer

thickness in the order of 100 nm so as to avoid recombination. However, a thin photon absorbing layer implies high photon transmission and hence increased energy losses [47]. The presence of reflection mechanisms is the third factor. Reflection losses are significant through surface and internal reflections. Anti-reflection coatings as used in inorganic devices may then prove useful once other losses such as recombination become less dominant.

2.3.5 Exciton diffusion

Ideally, all photo-excited excitons should reach a dissociation site. The distance between the point of exciton formation and hetero-junction interface should be less or equal to the diffusion length of the exciton. The active layer thickness should be in the order of 300 nm so as to absorb enough of solar energy. Active Layers thinner than 300 nm may not absorb enough of the solar energy, whilst active layers thicker than 300 nm may lead to recombination of the free charge carriers before reaching electrodes. Exciton diffusion ranges in polymers and pigments are typically around 10 nm [47, 48]. However, some pigments like perylenes are believed to have exciton diffusion length of several 100 nm [49, 50].

2.3.6 Charge separation

Charge separation is known to occur at organic semiconductor/metal interfaces, impurities points (such as oxygen molecules) or between materials with sufficiently different electron affinities (EA) and ionization potentials (IP). In the latter case one material can then act as electron acceptor (A) while the other keeps the positive charge and is referred to as the electron donor (D). If the difference in IP and EA is insufficient, the exciton may simply hop onto the material with the lower band gap without splitting up the charges. On the other hand, free charges may recombine just after separation [50, 51].

2.3.7 Charge transport

The transport of charges is affected by recombination during the journey to the electrodes, particularly if the same material serves as transport medium for both electrons and holes. Also, interaction with atoms or other charges may slow down the movement of the charges thereby limiting the current.

2.3.8 Charge collection

In order for an electron to drift to an electrode, the electrode material must have a relatively low work function compared to the anode. However, before reaching the electrodes the charges often have to overcome the potential barrier of a thin oxide layer. Additionally, the metal may have formed a blocking contact with the semiconductor so that charges can not immediately reach the metal. Semiconductor/metal interfaces are discussed in more detail in the Sections that follow.

2.3.9 The Donor/Acceptor Interface

In a BHJ system, exciton dissociation occurs at the donor/acceptor (D/A) interface. Though there are dissociation contributions from impurity points, the dominating factor is the D/A interface. Figure 2.6 a) shows that the required transfer of charges can be realised at the interface between two materials, if one material has a higher electron affinity (EA) whilst the other has a lower ionisation potential (IP). The one with the larger EA can accept an electron from the CB of the other and is referred to as electron acceptor. At the interface, the material with the lower IP can accept the hole from the VB of the contacting semiconductor, termed hole acceptor or electron donor since it donates electrons to the contacting acceptor. The difference (offset) of IP and EA needs to be large enough so that the resulting field (the potential gradient at the junction) can overcome the exciton binding energy which is typically around 0.4 eV. Otherwise charge transfer may occur but the excitons do not

split into their constituent charges and recombine eventually at the D/A interface [52].

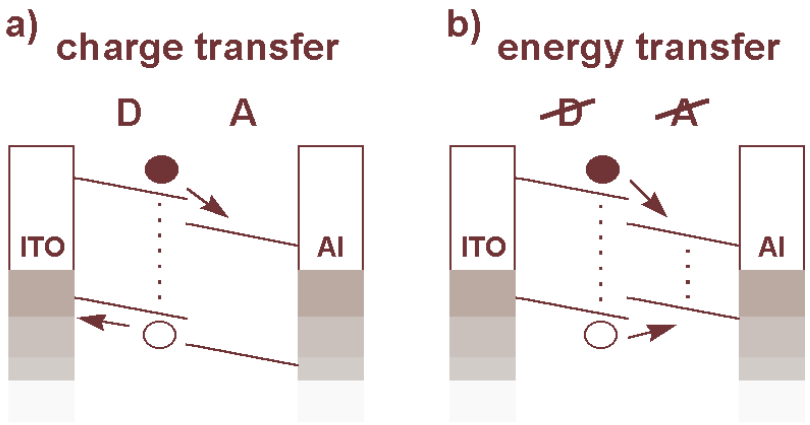


Figure 2.6: The interface between two different organic semiconductors can either: **a**) facilitate charge transfer (D/A interface), **b**) energy transfer with no exciton splitting. Empty circles represent holes and filled circles represent electrons [52].

Figure 3.2 b) shows that an exciton that carries its excitation energy can be transferred from the material with the higher band gap to the other if both the hole and the electron can lower their energy and become more stable eventually. This process of excitation energy transfer is also known as Foerster transfer and can be used to shift the emission band of the exciton towards lower energies [52, 53].

2.3.10 Schottky Barrier

While discussing the performance of the photo-charges it is necessary to know what goes on at the interface between the semiconductor and a metal when the contact is made. Figure 2.7 and Figure 2.8 below may be used to explain the Schottky barrier theory. Where Φ_M is the metal work function, Φ_B is the barrier potential and q is the electronic charge. E_C and E_V are the energy of the conduction and valence bands, respectively. E_F is the Fermi level whilst E_i is the ith energy level. E_{EM} represents the electromagnetic field.

The difference in energy between the LUMO level of the semiconductor and the vacuum level (E_{vacuum}) is denoted as χ

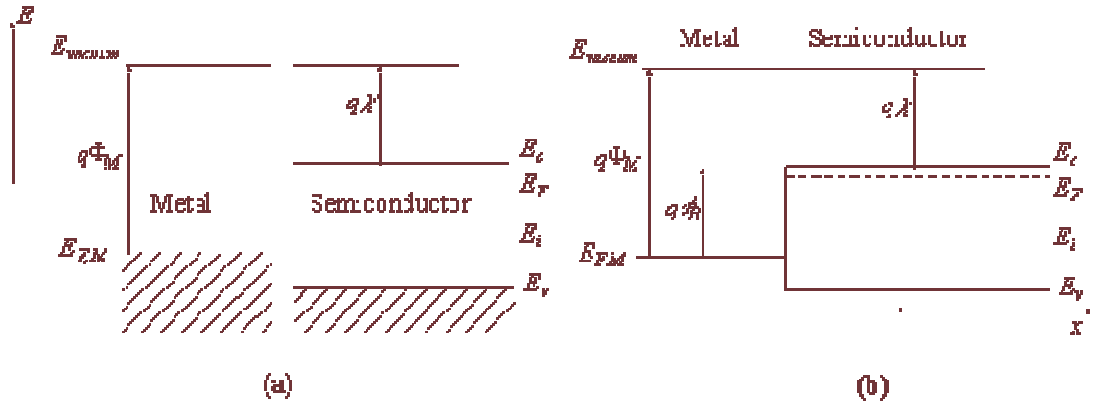


Figure 2.7: Energy diagram of metal-semiconductor junction before (a) and after (b) making contact for an n-type semiconductor [52].

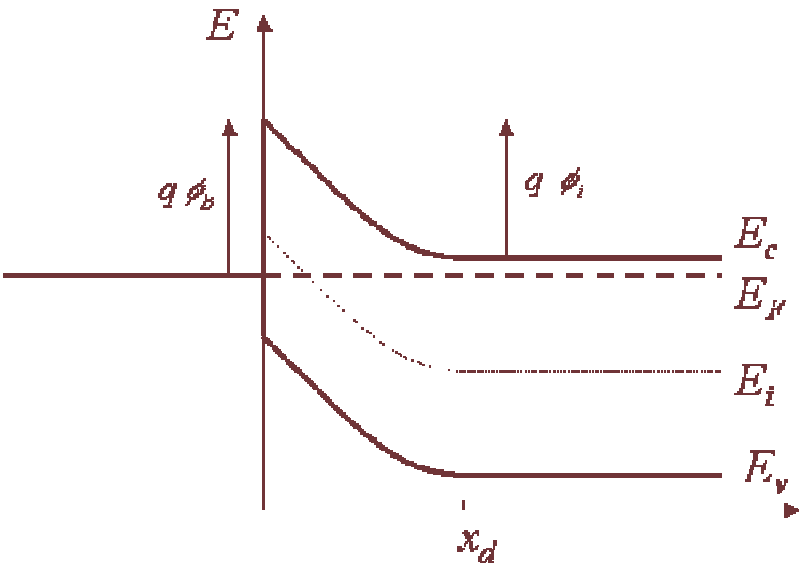


Figure 2.8: Energy band diagram of a metal-n-type semiconductor contact in thermal equilibrium. Where $_d$ is distance in the x direction [52].

Consider the formation of a metal-semiconductor junction by simply "attaching" a metal to a semiconductor. The energy of vacuum is used as reference to align the energy levels of the semiconductor and the metal. At equilibrium the Fermi energy is equal throughout the semiconductor and the

metal. But the Fermi energy of metal and semiconductor do not change right away. Figure 2.7 (b), is therefore not an equilibrium diagram, but Figure 2.8 is.

The electrons in the semiconductor reside in the conduction band and have energy larger than E_c. They can cross the metal-semiconductor junction and lower their energy by moving into the metal, which has continuous energy levels. These electrons leave behind a positive charge, and a resultant electrostatic field, which is directed from the semiconductor to the metal. This field lowers the band edges of the semiconductor.

The process of electron flow into the metal continues until the electric field created by ionized charges left behind in the semiconductor becomes strong enough to stop any further movement of electrons across the junction. In this condition, the diffusion of electrons from the semiconductor to the metal equals the drift of electrons caused by the electric field created by the ionized impurities. The Fermi energy is equal throughout the structure under these conditions.

Figure 2.7 shows contact between semiconductor and metal, called Schottky contact, and it is responsible for preventing the recombination of photo generated electrons and holes. This is because holes, which reside in the valence band have a tendency to "float" and move to upper energy levels in the valence band, while electrons, which lie in the conduction band have a tendency to move to lower energy levels in the conduction band. In case of an n-type semiconductor, the band edges near the interface are curved upward.

The absorption of photons can take place at the interface or the bulk of the semiconductor depending on the depth of penetration of light, but the holes produced always move to the interface where they can move to higher energy levels because of the upward curvature. The electrons, on the other hand, move to the bulk of the semiconductor, where they find lower energy than the interface. This effectively separates the electron-hole pairs. The recombination of electron-hole pairs would lead to short circuiting of the cell and reduce photo current and hence reduce power conversion efficiency. Hence, formation of Schottky barrier is a desirable phenomenon [52, 53].

2.4 Limitations of OPV Cells

The main limitations of OPV cells is the narrow absorption wavelength range, short shelf life span due to rapid degradation when exposed to atmospheric conditions such as moisture and oxygen, and reaction of the active layer with electrode materials. Polymer, polymer-fullerene, and polymer-Nan crystal photovoltaic cells, typically, absorb solar energy only in the wavelength interval between 450 nm and 750 nm, with the exception of one recent report which extend out to 1000 nm [52, 53]. Half of the sun's power spectrum lies beyond 700 nm and one third beyond 1000 nm of the spectrum hence outside the absorption range many organic systems.

On the other hand, organic semiconductors can be made more resistant to oxidation by the use of titanium oxide thin film layer between the active layer and the cathode. Oxidation is also avoided by either capping the reactive metal electrode with a less reactive one or by encapsulating the device to protect it from environmental effects during outdoor operations. Additionally, organic semiconductors can be made 'harder' by tuning their glass-transition temperature with cross-linking.

2.5 Determination of Organic Solar Cell Efficiencies

In order to determine the power conversion efficiency (η) and electrical characteristics of the solar cells, current-voltage measurements are performed, both in dark and under illumination conditions. A typical current-voltage (I-V) characteristic of a solar cell under illumination is shown in Figure 2.9 (A). The fourth quadrant represents the voltage and current that is generated by the cell. An externally applied voltage is necessary to obtain data points in the first and third quadrant. The shaded area in Figure 2.9 (A) corresponds to the maximum power that the solar cell can supply. When current density under illumination is zero, it is known as the open-circuit voltage V_{oc}.

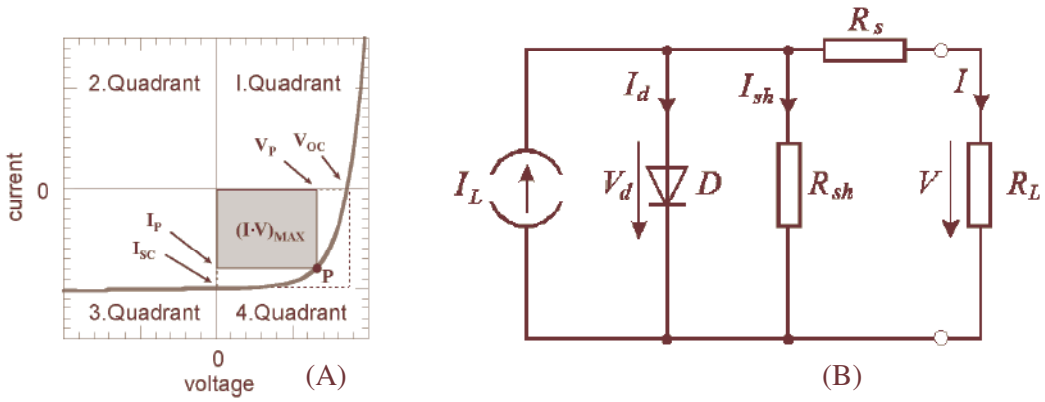


Figure 2.9: (A) Typical ccurrent – voltage (I-V) of a solar cell in and (B) typical ECD of a solar cell [53].

Figure 2.9 (B) is the Equivalent Circuit Diagram (ECD) of a solar cell. The circuit consists of the current source I_L that considers the light-generated current, a diode that accounts for the nonlinear voltage dependence and a shunt as well as a series resistor, a load resistor R and its voltage drop and current. I_{sh} is the shunt resistance. V_d is diode voltage while I_d is the diode current. R_s and R_L are series and load resistances, respectively.

The current arrows point into the direction the holes flow - according to the standard in electronics. The current I is negative if $V > V_{oc}$ and it flows “into” the device, otherwise it is positive [53]. The current under illumination at zero applied voltage, that is, $V_p = 0$ (V_p corresponds to positive biasing of the anode voltage) is called the short-circuit current, I_{sc}. The maximum voltage that the cell can supply, that is, the voltage where the current under illumination I_p is zero is designated as the open-circuit voltage V_{oc}.

The fill factor (FF) is defined as

$$FF = \left(\left| I_p V_p \right|_{\max}\right) / \left(V_{OC} I_{SC}\right), \qquad (2.11)$$

relating the maximum power that can be drawn from the solar cell to the open-circuit voltage and short-circuit current. The power conversion efficiency η is related to these three quantities by

$$\eta = \frac{I_{SC} V_{OC} FF}{I} \qquad (2.12)$$

where I is the incident light intensity. Because of the temperature and light intensity dependence of the photovoltaic response, the efficiency must be measured under standard test conditions. The standard test conditions are temperature of the cell of 25 ℃, the light intensity of 1000 W/m^2 and the spectral distribution of light at Air Mass of 1.5 [18].

Since the spectral width of the light used for the solar radiation (SR) measurements is set at the same value as the chosen spectral resolution, the integral could be obtained by simple addition of all obtained values together. The mean values of the open circuit voltage and FF can be taken and the equation below can be applied:

$$\eta_{AM1.5d} \approx \frac{\left(\sum_{\lambda_1}^{\lambda_2} J_{SCAM1.5}(\lambda) \right) . \bar{V}_{OC} . \bar{FF}}{P_{AM1.5d}} \qquad (2.13)$$

where $P_{AM1:5d}$ = 100 mW/A, (A is the area of the sample cell (1 cm^2)) being the sum (integral) of the light power over the entire AM 1.5d spectrum and J_{SC} is short circuit current (I_{SC}) per unit area. As an alternative to this method, the power per device area $J_{scAM1:5d}.V_{oc}$ for each wavelength interval before building the integral (sum) can be calculated as in Equation 2.14.

$$\eta_{AM1.5d} \approx \frac{\left(\sum_{\lambda_1}^{\lambda_2} J_{SCAM1.5}(\lambda).V_{OC}(\lambda) \right) . \bar{FF}}{P_{AM1.5d}} \qquad (2.14)$$

This method is reported as giving more accurate results. Since both methods can be justified equally, the mean of both numbers is taken for the final results.

Chapter 3

Characterization of Starting Materials for the Solar cells

The materials used for the fabrication of the solar cells were characterized before being used to ascertain their chemical and physical properties such as material behavior, composition and particle sizes. Methods such as X-ray diffraction (XRD) spectroscopy, Fourier transform infrared (FTIR) spectroscopy, high-resolution transmission electron microscopy (HR-TEM), and atomic force microscopy (AFM) as described in the sub-sections below were used to determine structure and morphology of the materials. The electrical properties were evaluated using 4-point probe.

3.1 Electrical Properties of the Solar Cell Materials

ITO is used as an electrode material in solar cells. Its conductivity is influenced by the ambient gas. It is therefore important to identify gas media that favours conductance for the material. The media that provides low electrical resistance can then be introduced either during the application of the device or during the processing of the semiconductor as is in the case of annealing of the thin films. Studies have shown that ITO thin films annealed in an inert atmosphere have better conductivity than the one annealed in air [54].

3.1.1 Experimental

ITO pellets were made from the ITO powder and the sheet resistance measured by means of a 4 - point probe method (Keithley, 2400 source meter). The electrical behaviour of bulk ITO was investigated by changing the environment using argon, hydrogen and air. The dc electrical measurement gas chamber was heated at 120 ^{o} C with the initial resistance in the chamber set at 33.63 Ω. The resistance was investigated by changing the composition surrounding the sample initially in air, then in an air - argon and finally air – argon – hydrogen gas mixture. These experiments were carried out to establish the effect of different gas media on the conductivity of ITO.

3.1.2 Results and Discussion

Figure 3.1 shows the resistance behaviour of ITO under different gas environments. The resistance of bulk ITO in air is shown between points ***a*** and ***b***. At point ***b*** argon gas was introduced into the chamber and gave a sharp fall in resistance. The resistance following the introduction of argon exhibited an exponential fall as more inert atmosphere continued to be established. Between points ***c*** and ***f***, hydrogen gas was gradually introduced through a tap and a slight increase in resistance was observed momentarily due to the disturbance in the atmosphere. The period after point ***f*** *on the* graph corresponds to the period when the hydrogen tap was fully opened. The resistance slightly reduced but later showed minor increase. The results clearly show that the electrical resistance is affected by the environment and was observed to be lower in an inert environment than in air.

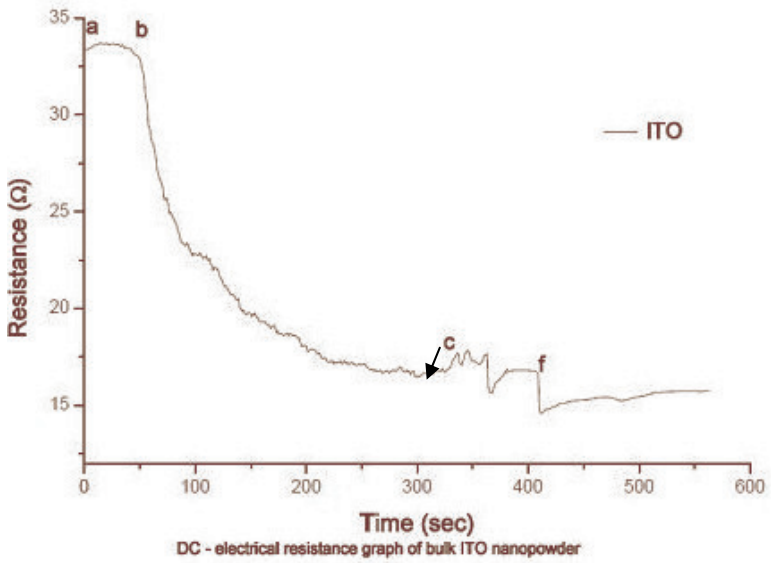


Figure 3.1: dc Electrical Resistance of Bulk ITO in various gas media

3.2 Structural Properties of the Solar Cells and Materials

The chemical composition, structure and morphology of materials have a profound influence on absorption and conductivity of solar cells. It is therefore pertinent to characterize the starting materials to determine their material properties. The results from the experiments also provide information on the particle size and integrity of the materials to be used in the construction of the solar cells. Chemical and structural characteristics were obtained using XRD and FTIR whilst HR-TEM and AFM were used to examine the morphology of the materials.

3.2.1 X-Ray Diffraction (XRD) of Nanopowders

The behaviour of solids stems from the arrangement and properties of constituent atoms. The arrangement leads to bulk properties that include rigidity, brittleness and electrical conductivity. Since the wavelength of x-rays is comparable to the size of atoms, they are ideally suited for probing the

structural arrangement of atoms and molecules in a wide range of materials. Energetic x-rays can penetrate deep into the materials and provide information about the bulk structure. Information from XRD measurements provides “finger prints” of materials that can be used for identification or verification of the integrity of the materials. This is because the distribution of diffraction angles, and therefore peak position and intensities for each material is unique.

3.2.2 Experimental XRD of ITO

The crystallinity of ITO powder was assessed from powder x-ray diffraction (XRD) patterns. XRD measurements were performed on a Rigaku D/MAX-RC apparatus. The incident wavelength was CuK_{α} = 0.154056 nm and the detector was moved between 2θ equal to 15 ° and 75 °. The scan speed was set at 3 °/min. The specific surface area of the ITO particles was measured by BET (Brunauer-Emmet-Teller) method whilst the chemical composition was determined by WDS (Wavelength Dispersive Spectrometry) technique. Results and discussion are given in the section that follows.

3.2.3 Results and Discussion

The results of the XRD analysis of ITO powder with a composition of 90 % indium oxide (In_2O_3) and 10 % tin oxide (SnO_2) are shown in Figure 3.2. The diffraction pattern and intensities were due to indium oxide only since tin oxide is not detectable at 10 % doping levels [54]. The ITO spectrum in Figure 3.2 is consistent with the “finger print” typical of ITO. This was confirmed by comparing the known ITO spectrum stored in the database with the ITO spectrum produced from the experiment. The two spectra matched hence confirming the two materials were identical.

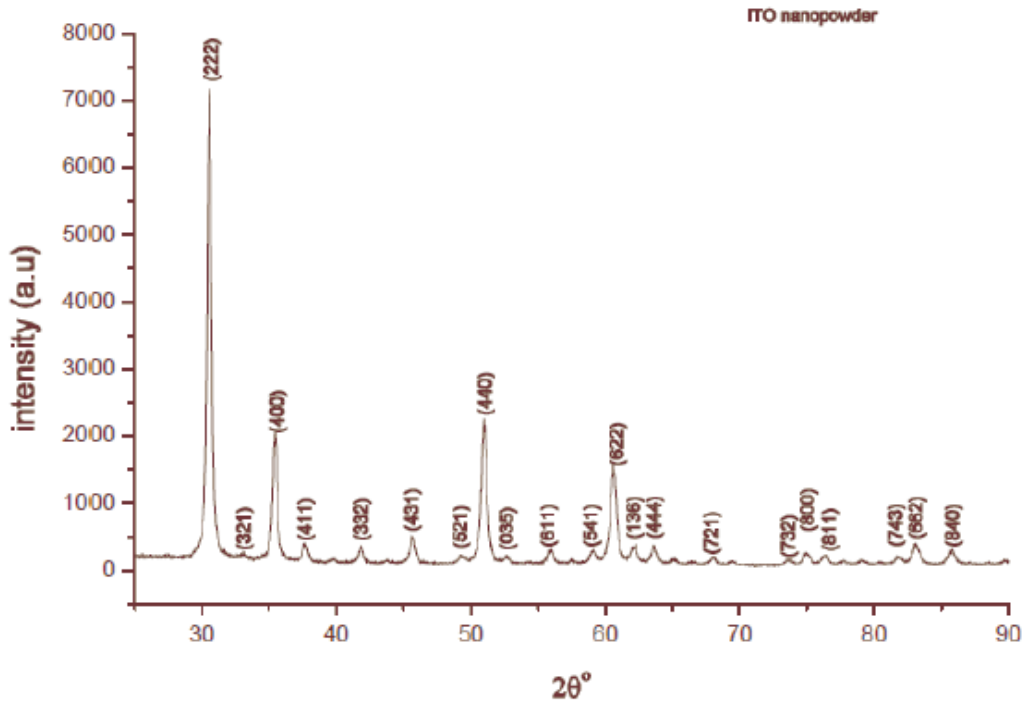


Figure 3.2: XRD spectrum of indium tin oxide ($In_2O_3.SnO_2$) nanopowder.

The ITO in the pattern above has a bcc structure with lattice constant a = 10.12 Å .The wavelength of the x-rays used was λ = 1.5406 Å. Using Equation (3.1) the value of the crystal's inter-planner spacing (d_{hkl}) were calculated and are shown in Table 3.1.

Table 3. 1: The ITO parameters for selected peaks from XRD pattern and the calculated particle (crystallite) size.

2ɵ °	ɵ °	d_{hkl} (Å)	(hkl)	β_{hkl} (rads.) x 10^{-3}	Particle size (L_{hkl}) in nm
30.559	15.280	2.921	(222)	6.109	20.941
33.029	16.515	2.705	(321)	5.672	25.212
35.437	17.719	2.530	(400)	6.240	23.069
37.658	18.829	2.385	(411)	5.662	25.586
41.810	20.905	2.158	(332)	4.515	32.507
45.629	22.814	1.985	(431)	6.109	24.351
50.964	25.482	1.789	(440)	7.283	20.854
60.595	30.297	1.526	(622)	7.857	20.212
83.096	41.548	1.161	(662)	6.141	29.831
					$< L_{hkl} > = 24.729 \pm 4.185$

$$d_{hkl} = \frac{a}{\sqrt{h^2 + k^2 + l^2}} \quad \text{or} \quad d_{hkl} = \frac{n\lambda}{2\sin(\theta_{hkl})} \qquad (3.1)$$

The particle size or crystallite length (L_{hkl}) was calculated using Scherer's equation given as Equation (3.2).

$$L_{hkl} = \frac{K\lambda}{\beta_{hkl}\cos\theta_{hkl}} \qquad (3.2)$$

β_{hkl} is the width of the peak at half maximum intensity of a specific phase (hkl) in radians and K is a constant that varies with the method of taking the breadth and takes values in the range 0.89 < K < 1. The most accurate methods take K = 0.89, λ is the wavelength of incident x - rays, θ is the centre angle of the peak or Bragg angle, and L is the crystallite length in meters. The method used in this study for determining the value of β_{hkl} is accurate up to 5 decimal points hence K = 0.89 was used.

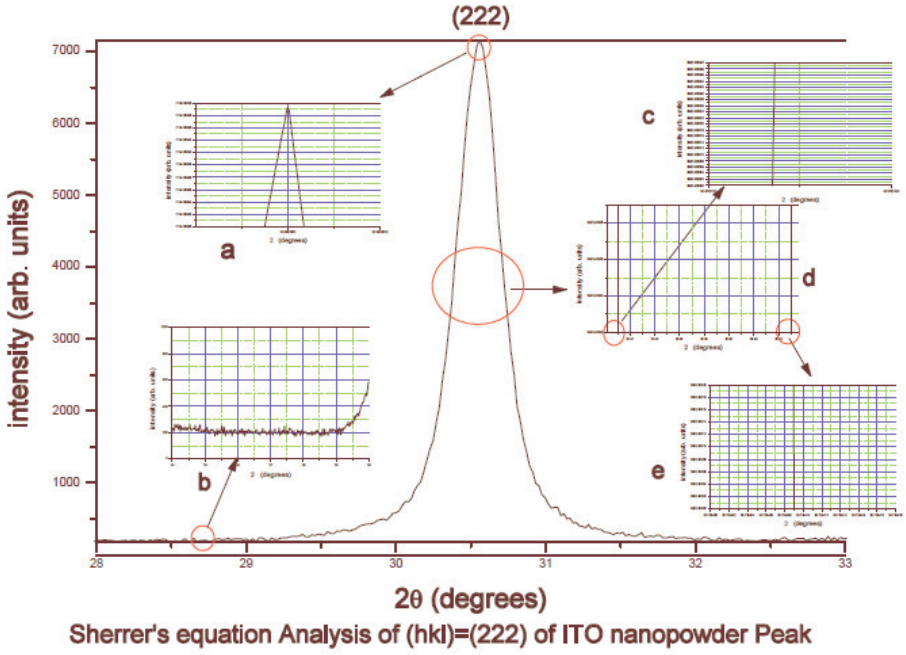


Figure 3.3: Example of β_{hkl} determination using a selected peak occurring at 2θ = 30.5 °.

Figure 3.3 above shows the evaluation carried out to determine the peak width at half maximum (β_{hkl}). The inserts (a) gives the maximum value of the peak and the exact diffraction angle ($2\theta_{hkl}$), (b) gives the minimum value of the peak, (c) and (e) give the details of the two arms at half maximum provided by (d). Using this method, the calculated average particle size for ITO powder was 24.729 ± 4.185 nm. The standard deviation in the calculated size was observed to be large which showed that the particles size was not uniform.

3.2.4 Experimental XRD of TiO_2

The experimental method used to characterize TiO_2 is similar to one described in sections 3.2.2 and 3.2.3 above for ITO. The values of the lattice constants are a = 4.5925 and c = 2.9578. The results of XRD on TiO_2 are shown in Figure 3.4 and the calculated values of lattice parameters are shown in Table 3.2. The results are given and discussed in the section that follows.

3.2.5 Results and Discussion

Figure 3.4 shows the XRD spectrum of titanium dioxide (TiO_2) nanopowder at different diffraction angles. The TiO_2 used in this study confirmed a rutile crystal form with a tetragonal structure. The highest intensity of the rutile TiO_2 was the (110) followed by the (211) peak as shown in Figure 3.4. The peak positions in Figure 3.4 matched with the positions of the peaks from known spectrum of TiO_2 confirming that the material was TiO_2. The average calculated particle size was 19.864 ± 2.122 nm. The small standard deviation of ± 2.122 nm in the calculated particle size showed that the particles were almost of the same size.

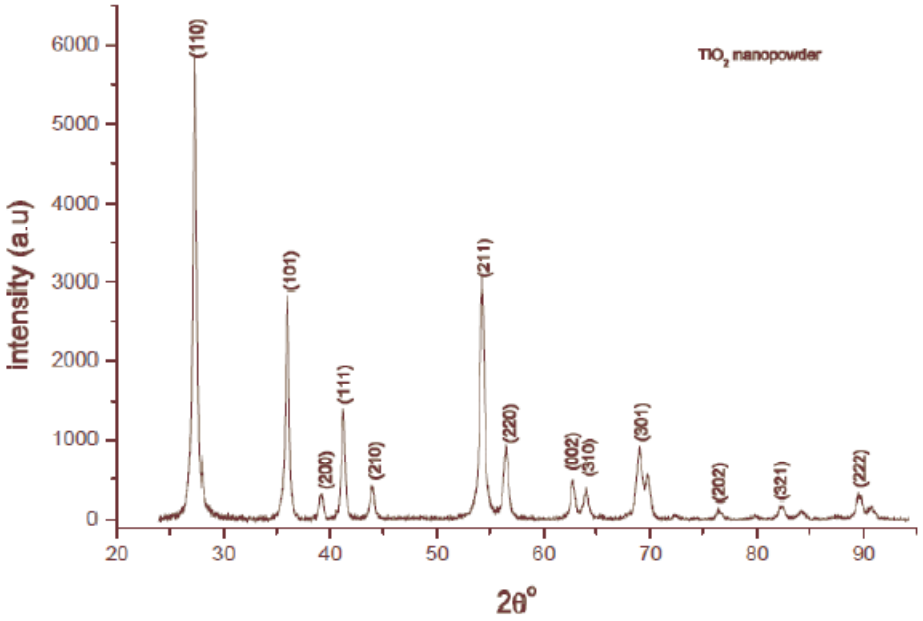


Figure 3.4: XRD spectrum of rutile TiO_2 nanopowder.

Table 3. 2: The TiO_2 parameters for selected peaks from XRD pattern and the calculated particle (crystallite) size.

2ɵ °	ɵ °	d_{hkl} (Å)	(hkl)	β_{hkl} (rads.) x 10^{-3}	Particle size (L_{hkl}) in nm
27.383	13.692	3.254	(110)	7.533	18.734
36.039	18.020	2.490	(101)	6.434	22.411
41.228	20.614	2.188	(111)	6.685	21.915
54.285	27.142	1.689	(211)	8.431	18.275
56.568	28.284	1.626	(220)	8.657	17.986
					$< L_{hkl} >$ =19.864 ± 2.122

3.2.6 Experimental XRD of P3HT and PCBM

The experimental method used to characterize PCBM and P3HT is similar to one described in sections 3.2.2 and 3.2.3 for ITO. The resulting graphs were plotted and prominent peaks were identified and analysed for different parameters such as brag angle and half maximum width. The crystallite size

was also determined and results were later summarized in a table. The results and discussion are given in the sections that follow.

3.2.7 Results and Discussion

Typical XRD spectra for P3HT and PCBM are shown in Figure 3.5 and 3.6 respectively. The highest and dominant XRD intensity peak of P3HT nanopowder was recorded at θ = 12.5 º. The other peaks were not well defined in intensity as can be seen from Figure 3.5.

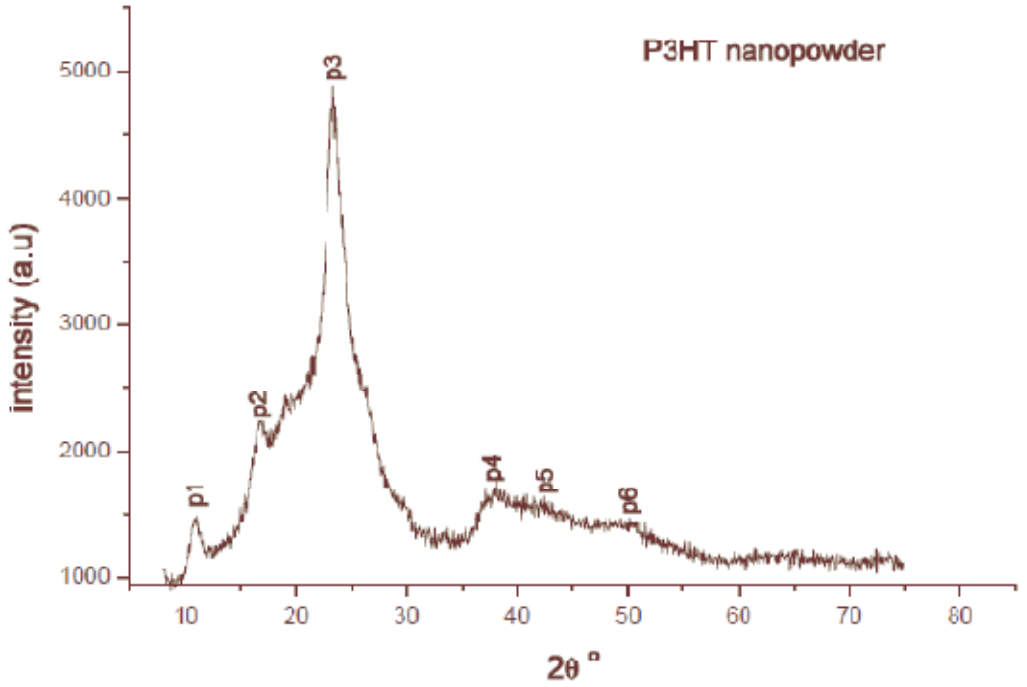


Figure 3.5: XRD spectrum of P3HT nanopowder

The system used for XRD analysis did not provide a database for P3HT and C_{60}- PCBM. Therefore the (hkl) values for the peaks are not available for the polymer so that this result is not normalized. However, the values of d_θ, β_θ, L_θ were calculated for the selected peaks and entered into the respective tables (Table 3.3 and 3.4).

Table 3. 3: The P3HT parameters for selected peaks from XRD pattern and the calculated particle (crystallite) size.

Peak	2ɵ °	ɵ °	$d_ɵ$ (Å)	$\beta_ɵ$ (rads.) x 10^{-3}	Particle size ($L_ɵ$) in nm
P1	11.100	5.550	7.965	35.503	3.88
P2	16.718	8.359	5.299	43.111	3.215
P3	23.353	11.677	3.806	71.007	3.066
P4	38.029	19.014	2.364	62.554	2.318
P5	42.436	21.218	2.128	37.195	3.954
P6	50.089	25.044	1.820	74.388	2.034
					$<L_ɵ>$ = 3.078 ± 0.787

The determination of the sizes of the crystallites for both P3HT and PCBM was difficult due the irregularity of the peaks. The exact position of the bottom of the peaks and hence the half - maximum height could be easily be determined. The average calculated particle size for P3HT was 3.078 ± 0.787 nm. A standard deviation of ± 0.787 nm is observed to be small and therefore the particles were considered to be have a narrow particle size distribution.

The highest XRD intensity on PCBM nanopowder was observed at about θ = 10 º as shown in Figure 3.6. Most of the peaks in the PCBM spectrum are not clearly resolved making it difficult to determine the half-maximum value. From the calculated values, the mean crystallite size for PCBM was 12.432 ± 2.427 nm as shown in Table 3.4. The large standard deviation could, in part, have originated from the fact that it was difficult to locate the exact location of bottom of peaks in determining particle size for individual peaks.

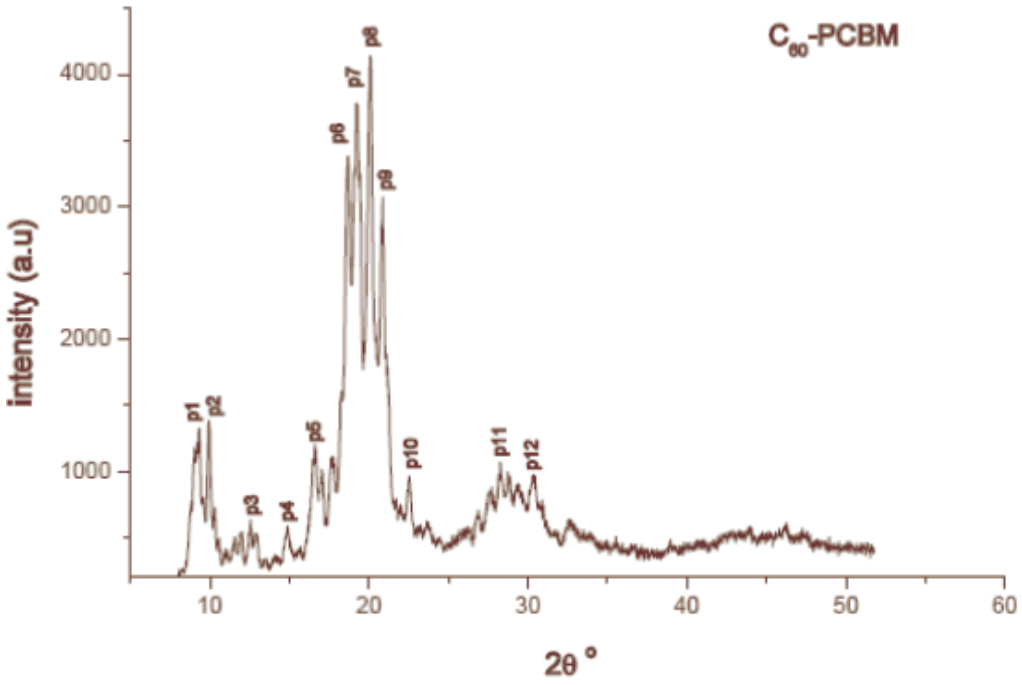


Figure 3. 6: XRD spectrum of C_{60} –PCBM nanopowder at different diffraction angles.

Table 3. 4: The C_{60} -PCBM parameters for selected peaks from XRD pattern and the calculated particle (crystallite) size.

Peak	2ɵ °	ɵ °	$d_ɵ$ (Å)	$\beta_ɵ$ (rads.) x 10^{-3}	Particle size ($L_ɵ$) in nm
P1	9.308	4.654	4.747	16.664	8.255
P2	9.930	4.965	8.900	11.594	11.871
P3	12.546	6.273	7.050	8.332	16.555
P4	14.891	7.446	5.944	10.868	12.724
P5	16.593	8.297	5.338	12.680	10.928
P6	18.690	9.345	4.744	8.693	15.985
P7	19.209	9.605	4.617	13.404	10.375
P8	20.081	10.041	4.418	10.505	13.255
P9	20.869	10.435	4.253	12.680	10.995
P10	22.509	11.255	3.947	12.317	11.350
P11	28.259	14.129	3.156	9.420	15.010
P12	30.335	15.167	2.944	11.956	11.882
					$< L_ɵ > = 12.432 \pm 2.427$

3.3 FTIR Analysis of Nanopowders

Fourier Transform Infrared (FTIR) spectroscopy is a widely used technique for characterizing materials. The spectrum produced from the analysis gives the identity of that particular sample. The absorption peak frequencies correspond to characteristic vibrations of bonds between atoms that make up the material. Thus, the FTIR spectrum is characteristic of a material and provides positive identification. The atoms in a molecule do not maintain fixed positions but vibrate back and forth about average bond distances [54, 55]. Since this motion is microscopic, it is quantized into discrete energy states by the laws of quantum mechanics and is referred to as Phonons. The laws indicate that for the simple stretching motion of a diatomic molecule with atoms that have masses m_1 and m_2, the vibration frequency (υ) depends on the stiffness of the chemical bond as determined by its force constant (k) and on the mass of the atoms as determined by the reduced mass (μ).These vibrations are best understood by the study of the first Brillion Zone as shown in Figure 3.7.

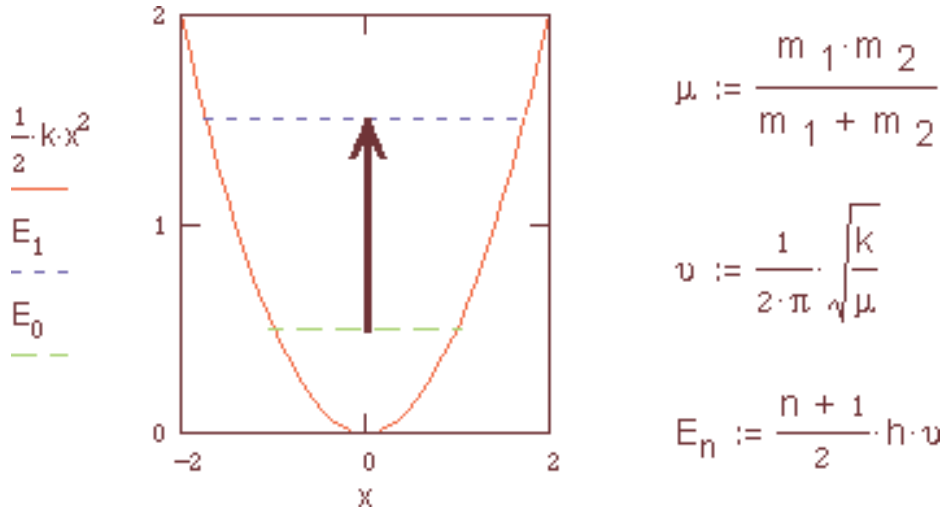


Figure 3.7: The first Brillion Zone of molecular vibrational energy [55].

The energy of a vibrating molecule E_n is given by a vibrational quantum number (n) Planck's constant (h) and the fundamental vibration frequency (υ). $h\upsilon$ is the fundamental quantum of energy and equals the energy spacing between each energy level. At room temperature most of the molecules will be in their lowest vibration energy state or zero-point energy E_0. This is the stable vibrating state of a molecule. Absorption of light with the appropriate energy ($h\upsilon = E_1 - E_0$) allows the molecule to become "excited" into the next higher vibration energy state E_1. The energy absorption peaks of the materials represented the characteristics of the particular functional groups.

Figure 3.8 shows the different vibration modes giving rise to various photo-absorptions. Stiff double bonds with large force constants vibrate faster than less stiff single bonds, and heavy atoms will vibrate slower than light atoms [55]. For this reason organic functional groups that have characteristic masses and bond strengths fall into particular regions in the infrared spectrum.

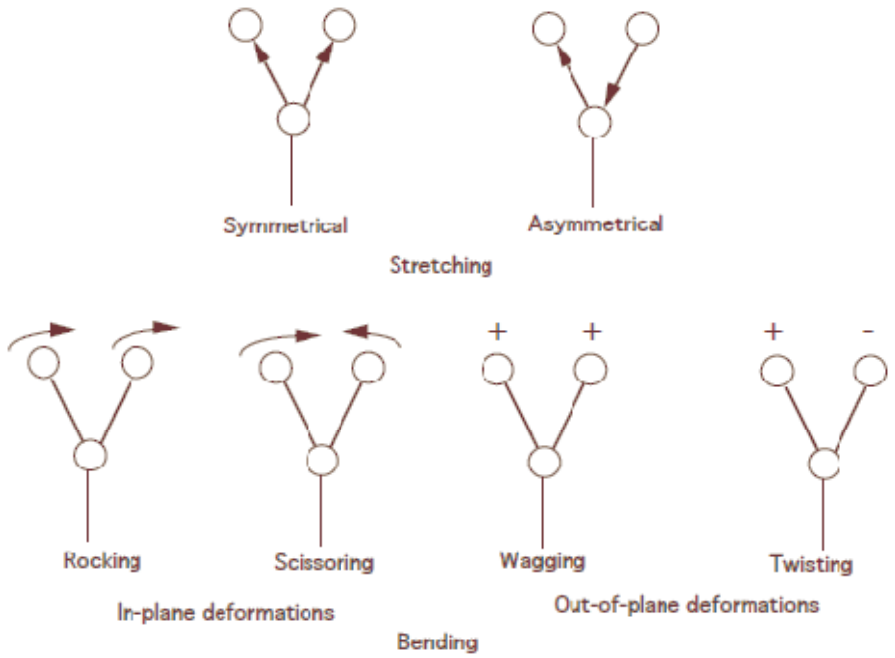


Figure 3.8: Various vibrations modes of molecules [55].

Figure 3.9 shows a simplified chart of the common functional groups and their characteristics absorptions bands. For example, the C = O double bonds vibrate in the range 1600 cm^{-1} to 1800 cm^{-1} whilst S = O bonds vibrate at around 1000 cm^{-1} as shown in Figure 3.9.

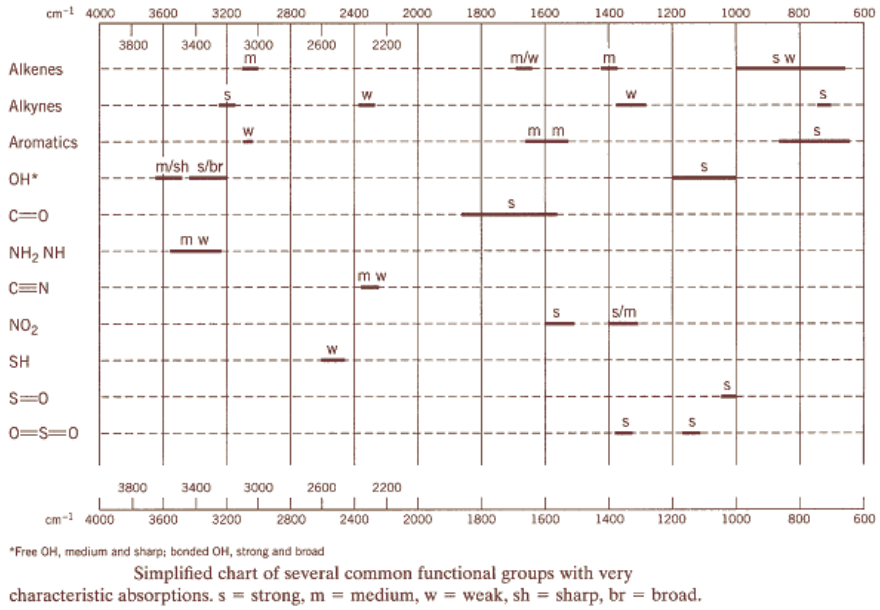


Figure 3.9: Simplified chart of several common functional groups [56]

Stretching frequencies in inorganic complexes occur at low frequencies because the atoms are heavy and weakly bonded. For example, Mo-Cl bond stretching occurs in the far infrared region at around 250 cm^{-1} wave number [56]. In organic compounds the bonds' bending force constants are much smaller than stretching force constants as a consequence, it is common to find bending modes at lower wave numbers while stretching modes are common at higher wave number values.

3.3.1 Experimental on the Nanopowders

The nanopowders were each placed in a small container and then inserted into the FTIR machine (Perkin Elmer 1600). The FTIR worked very well on

the polymers but some difficulties were encountered when analysing the inorganic nanopowders. This was because the range of the vibration mode for inorganic materials is in the short wave length, which was to the large extent out of range for the machine.

3.3.2 Results and Discussion

The spectra of the various materials used in this study are shown and discussed in sections that follow. The spectra show the characteristic absorption peaks and associated functional groups of vibrational modes of the bonds. Figure 3.10 shows the FTIR results of P3HT nanopowder . The peaks show the presence of carbon-to-carbon (C = C) double bonds stretching vibrations at 1515 cm^{-1} wave number. There are also strong stretching vibrations at 2906 cm^{-1} due to the presence of aliphatic CH_2 bonds. The presence of carbon-to-sulphur (C-S) deformation vibrations was detected at 816 cm^{-1} whilst that of C-H deformation vibrations was detected at 726 cm^{-1} as shown in Figure 3.10. The presence of these molecules was consistent with the chemical structure of P3HT and hence confirmed the integrity of the P3HT nanopowder [56, 57].

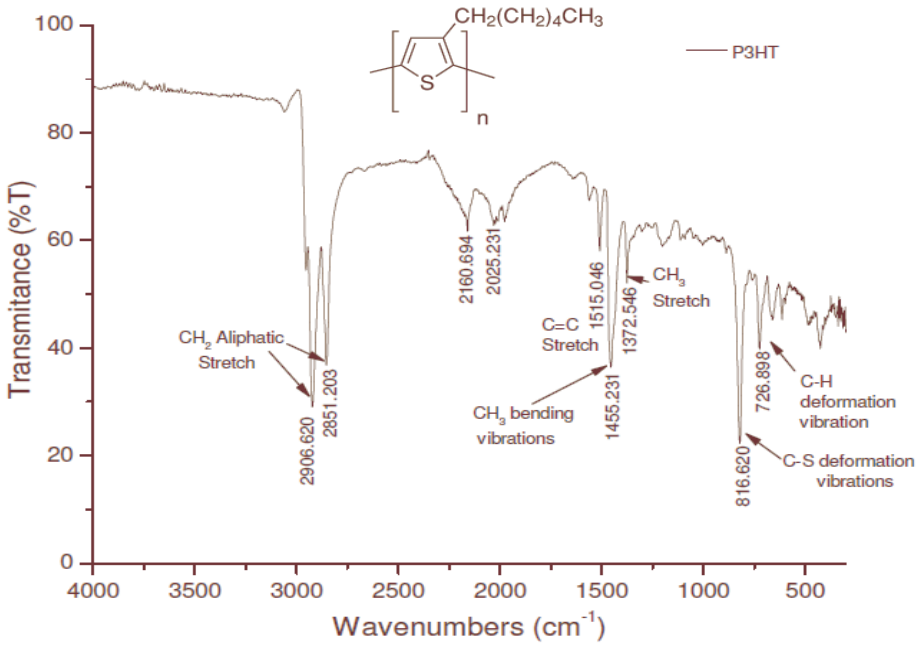


Figure 3.10: FTIR spectrum of the P3HT nanopowder

The FTIR results for PCBM are shown in Figure 3.11. The spectrum reveals a strong presence of C-H bonds bending and ring puckering vibrations at 692 cm^{-1} frequency. The PCBM spectrum also showed a strong presence of carbon-to-oxygen (C = O) double bonds stretching at 1732 cm^{-1} frequency. CH_3 bending was detected at 1424 cm^{-1} whilst oxygen-to-carbon (O – C) vibrations were detected at 1147 cm^{-1}. The presence of these peaks at the specified wave number was consistent with that of PCBM and hence confirmed its structure and integrity [57].

The peaks observed at 2157 cm^{-1} and 2008 cm^{-1} were due to instrumental error as they are consistent in the spectra for all the materials analysed

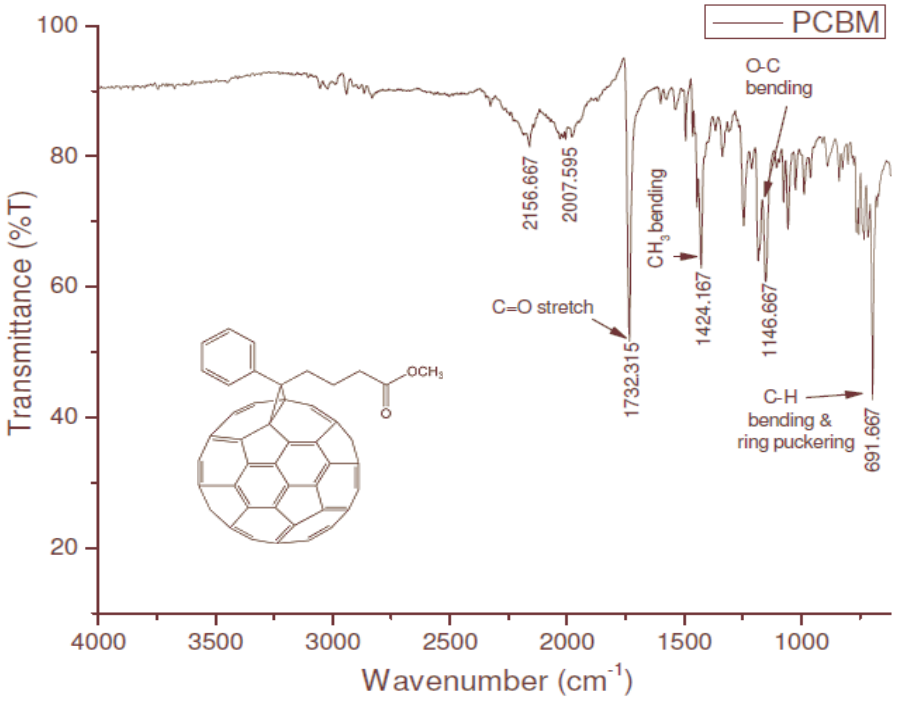


Figure 3.11: FTIR spectrum of the PCBM nanopowder

Figure 3.12 shows the FTIR spectrum of TiO_2 powder. The spectrum reveals the presence of rutile titanium-to-oxygen (Ti-O) single bond vibrations at 1026 cm^{-1} frequency. The presence of anatase Ti - O vibrations was detected at about 471 cm^{-1} frequency. The presence of both anatase and rutile forms of

TiO_2 in the spectrum shows that the TiO_2 powder was not pure rutile but a mixture of the rutile and anatase [58].

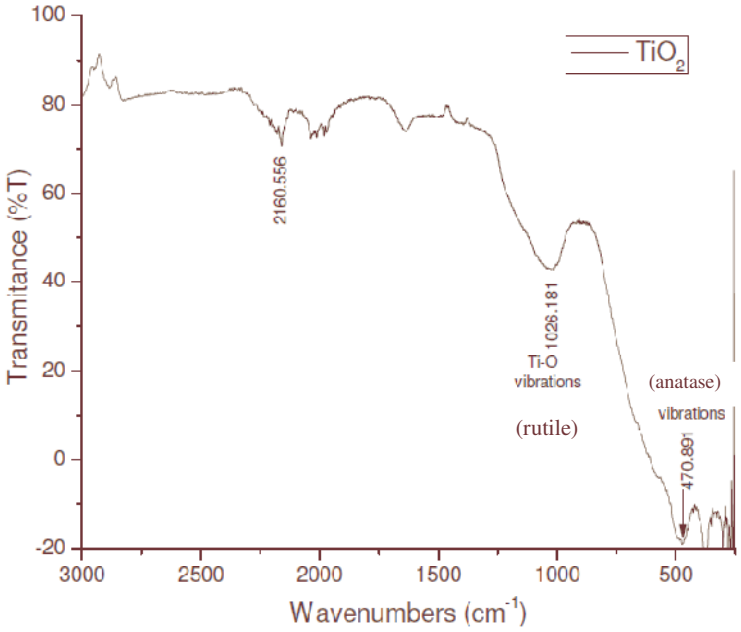


Figure 3.12: FTIR spectrum of the TiO_2 nanopowder

The FTIR spectrum of ITO is shown in Figure 3.13. The In-O bond vibrations in ITO were detected at 721 whilst the vibrations due to Sn-O were detected at 303 cm^{-1} as shown in Figure 3.13.

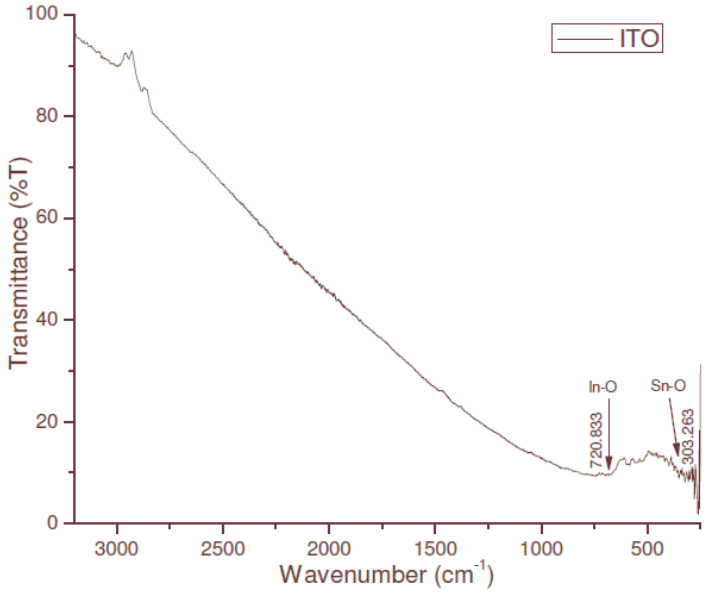


Figure 3.13: FTIR spectrum of the ITO nanopowder

This ITO spectrum is consistent with the material composition of the ITO powder and is also consistent with spectra reported from other studies [58].

3.4 Particle Size and Distribution Determination

The particle size and distribution were determined by means of high resolution transmission electron microscopy (HR-TEM). Knowledge of particle size and particle size distribution of the materials is important as it gives an indication of physical nature of the material at microscopic level. Knowledge of the size and shape may give guidance to tunable properties that influence the performance of the bulk material. Additionally, knowledge of particle size gives insight on the type of deposition method that can be used when developing thin films from these materials. High resolution TEM allows viewing of particle size as small as 5 nm of diameter and their size distribution. The shapes of particles are also discernable form the micrographs. For HR-TEM to be effectively used to analyze samples, the specimen needs to be in form of a thin film (few micrometers) to allow the transmission of electrons.

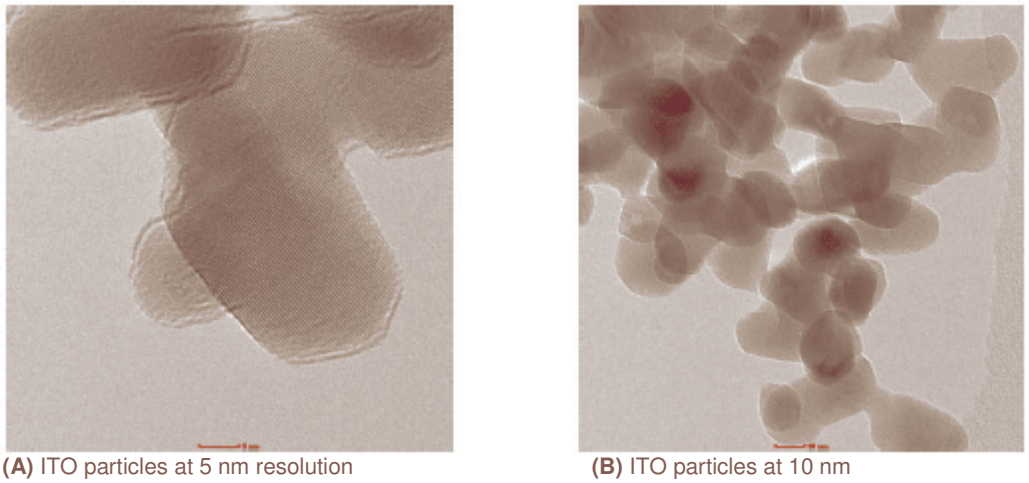
Furthermore, the sample needed to be conducting or semiconducting for electrons to be conducted from the HR-TEM tip, on the upper side, through the sample to the copper grid sample holder, on the lower side, which in turn transmits the information to the HR-TEM machine for analysis. Since both the organics and inorganics under investigation in this study were semiconducting, the use of HR-TEM was possible. The requirement for a thin film was met by making a suspension of the powders in an appropriate liquid and later dropping a small amount of the suspension on the sample holder (copper grid). The liquid was allowed to thereby forming a film. The details of the experimental and results are given in the subsequent sections.

3.4.1 Experimental on HR- TEM of the Nanopowders

The micrographs of the nanopowder particles were obtained using a High Resolution Transmission Electron Microscopy (HR-TEM, EM912 Omega). The samples were prepared by mixing the powders with ethanol followed by sonication. A drop of the powder dispersion was then placed onto a standard microscope copper grid. After evaporation of the solvent, a thin film formed on the grid which was placed in the instrument for evaluation of the particles size, size distribution and morphology. For each sample, four images were taken at typical resolutions of 5 nm, 10 nm, 20 nm, and 100 nm. The particle size from the micrographs analysis was achieved using Image Magic software. The results and discussion are given in the section that follows.

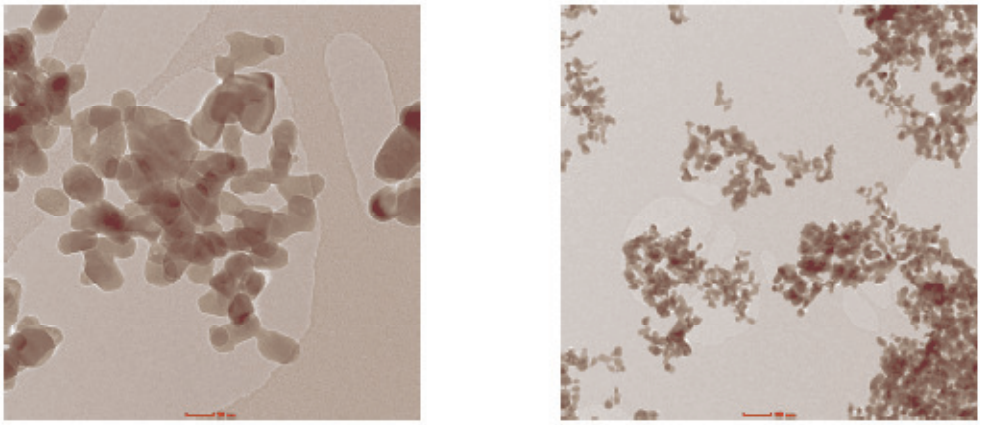
3.4.2 Results and Discussion

Typical HR-TEM micrographs for the ITO powder are shown in Figure 3.14 whilst the particle size distribution is shown in Figure 3.15. The micrographs show particles that are clearly cylindrical in nature (nano-rods) at 5 and 10 nm resolutions as shown in Figure 3.14 (A) and (B). At lower resolutions of 20 and 100 nm, the particles are seen in clusters consisting of several nano-rods as shown in Figure 3.14 (C) and (D).



(A) ITO particles at 5 nm resolution **(B)** ITO particles at 10 nm

Figure 3. 14: HR-TEM Micrographs showing at **(A)** 5nm and **(B)** 10 nm resolution of ITO particles distribution.



(C) ITO particles at 20 nm resolution

(D) ITO particles at 100 nm resolution

Figure 3. 14: HR-TEM Micrographs showing at **(C)** 20 nm and **(D)** 100 nm resolutions of ITO particles distribution.

The clustering of the particles could have been due to agglomeration of the primary particles which could be attributed to either van der walls forces or incomplete evaporation of the ethanol.

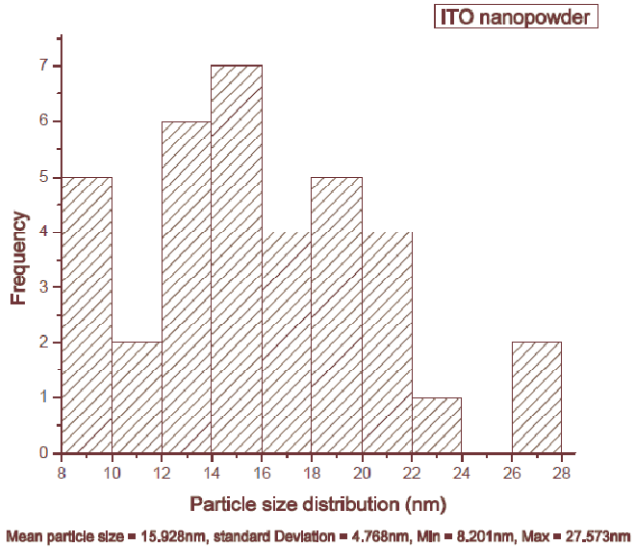
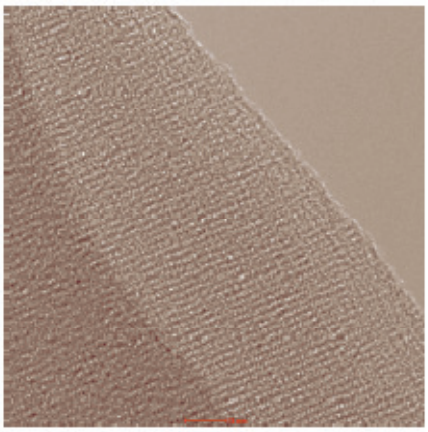


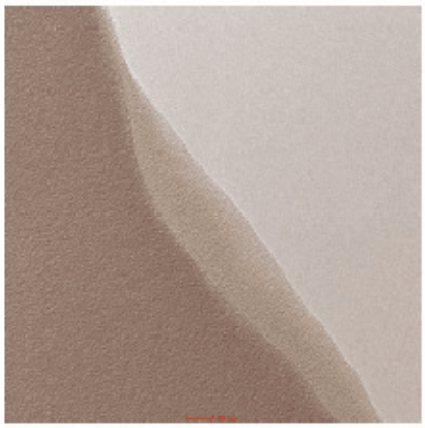
Figure 3.15: Particle size and distribution from HR-TEM results for ITO film of Fig 4.14 **(C)**

The average particle size for the ITO film was found to be 15.93 ± 4.77 nm. The distribution of the majority of the particles was between 12 and 22 nm as shown by Figure 3.15. The graph shows a broad distribution of particles size that is reflected in the standard deviation.

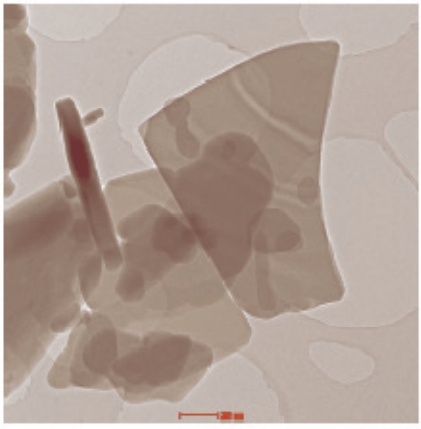
Figure 3.16 shows the TEM micrographs of PCBM at four different resolutions of 5, 10, 100, and 200 nm. Nano - sheets are clearly visible at 5 and 10 nm resolution as shown in Figure 3.16 (A) and (B). The micrograph at 5 nm resolution shows a porous structure of the nano - sheets.



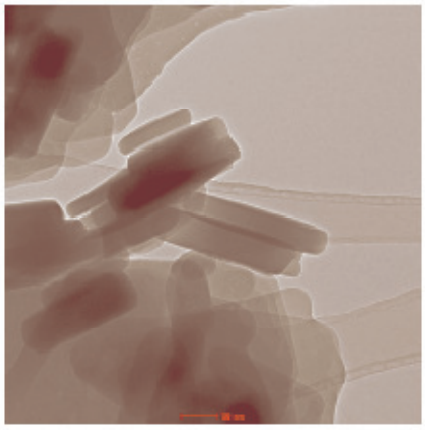
(A) PCBM at 5 nm resolution



(B) PCBM at 10 nm resolution



(C) PCBM at 200 nm resolution



(D) PCBM at 100 nm resolution

Figure 3.16: HR-TEM Micrographs of PCBM nanopowder at various resolutions of selected areas

Figure 3.16 (C) and (D) show the presence of nano-tablets at 100 and 200 nm resolution whose walls are made of nano-sheets. The latter are visible at 5 and 10 nm resolution.

The size of nano-sheets are shown in Figure 3.17 and observed to vary considerable in size. The calculated average was 291.596 ± 147.785 nm. The standard deviation was observed to be too large. The nano-sheet size distribution for PCBM could have been affected by the solvent (ethanol) used, which could have broken the polymer in non-uniformly manner, and this could have contributed to the large standard deviation. P3HT was not analysed under TEM due to its poor solubility in ethanol.

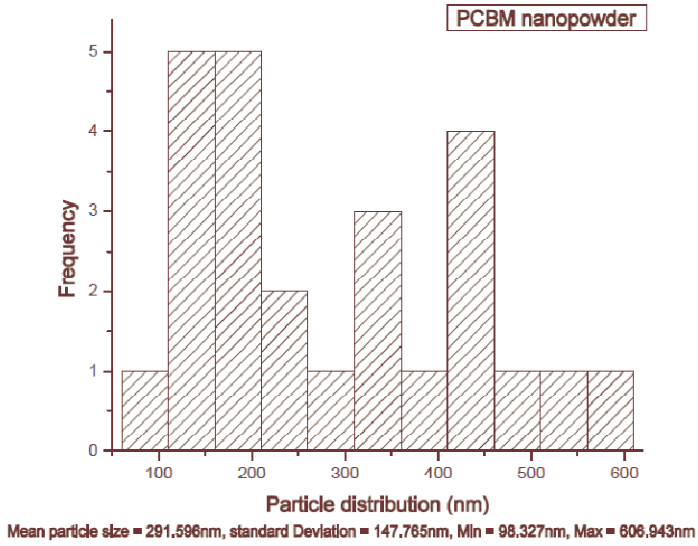
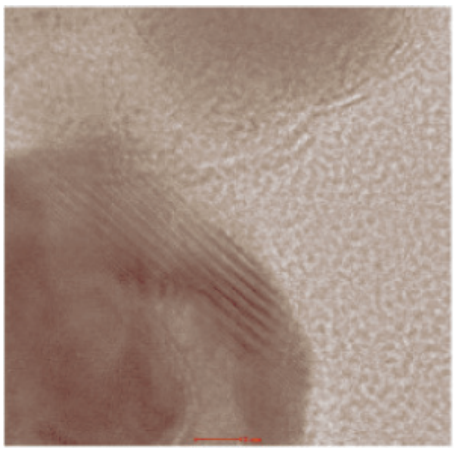


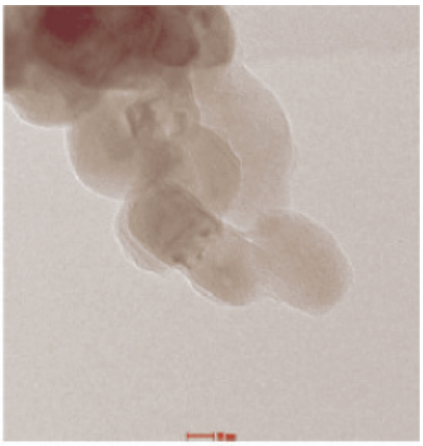
Figure 3.17: Particle size analysis of HR-TEM Micrograph of PCBM nanopowder from Figure 3.16 **(C)** and **(D)**

The calculation of the particle size was difficult because of the nano-sheet clustering. Despite having an average particle size of 292 nm, the majority of the particles were observed to have a size of about 150 nm as can be seen from Figure 3.17.

The particle distribution results of TiO_2 nanopowder at different resolutions is shown in Figure 3.18 (A), (B), (C), and (D).

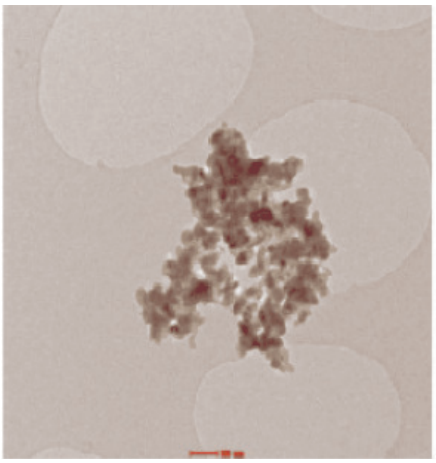


(A) TiO_2 powder at 5 nm resolution

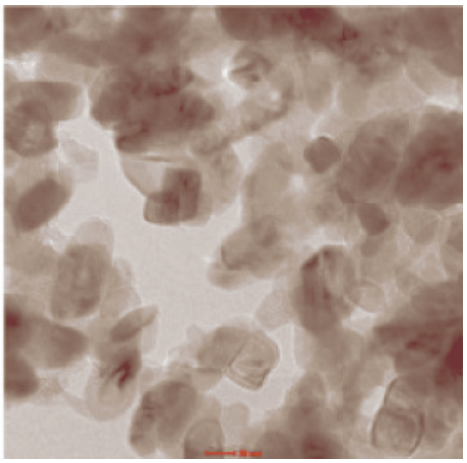


(B) TiO_2 powder at10 nm resolution

Figure 3.18 A: TiO_2 nanopowder HR-TEM Micrographs at **(A)** 5 nm and **(B)** 10 nm resolutions



(C) TiO_2 at 20 nm resolution



(D) TiO_2 at 100 nm resolution

Figure 3.18 B: TiO_2 nanopowder HR-TEM Micrographs at **(C)** 20 nm and **(D)** 100 nm resolutions.

The micrographs show heavy clustering of particles due to agglomeration. This made it difficult to analyse the individual particles using Image Magic.

Figure 3.19 shows the particle size and distribution of the TiO_2 film prepared from an ethanol suspension.

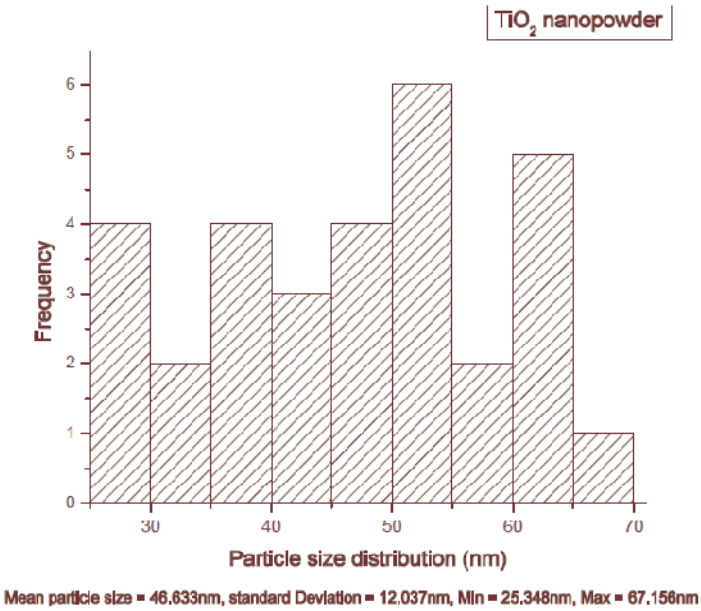


Figure 3.19: Particle size analysis of HR-TEM results of PCBM nanopowder from Figure 4.18 **(D)**

The average particle size for the TiO_2 powder was estimated at 46.633 ± 12.037 nm (Figure 3.19). The large standard deviation means that the particles size distribution is wide.

Chapter 4

Evaluation of the Solar Cell Thin Films

In order to build solar cells, thin films needed to be developed on substrates. Thin films were developed from TiO_2 powder and solutions of P3HT, PCBM, P3HT: PCBM, and PEDOT. Prior to developing thin films from P3HT and PCBM, the two polymers were tested for solubility in chloroform based on refractive index measurements. The solubility of these polymers in the solvent (chloroform) was crucial for achieving good blending from the two. The thin films developed were evaluated for photon absorbance and transmittance using UV-Vis spectroscopy. Additionally, the TiO_2 thin film was evaluated for surface morphology using AFM microscopy. A heat annealing process was carried out aimed at optimizing the photon absorbance of the P3HT and PCBM based thin films. The optimized thin films were then used to construct solar cells whose efficiency was subsequently determined. The details of the methods of preparation and evaluation are discussed in the sections that follow.

4.1 Solubility of P3HT and PCBM in Chloroform based on Refractive Index Measurement

The refractive index (*n*) value of a solution, formed from a given solvent and solute can be used as a measure of the solubility of the solute in that solvent. The solutes used in this study were P3HT and PCBM whilst the solvent was chloroform. The refractive index of pure chloroform was measured and then compared to the refractive indices of the solutions of P3HT and PCBM in chloroform. Having value of *n* of a solvent close to the *n* value of the solution implies good solubility of the solute, according to Equation 4.1. This is because light would be travelling at the same speed in the two media.

$$n = \frac{c}{V} \qquad (4.1)$$

In equation (4.1), c is the speed of light in air and V is speed of light in the solution.

4.1.1 Experimental

To test for the solubility of P3HT, PCBM and P3HT: PCBM in chloroform, solutions of these materials were prepared in various volumes of chloroform. About 20 mg of P3HT and PCBM were each dispersed in 3 mL of chloroform, separately. The dispersions were ultra - sonicated for 10 minutes to make solutions and their refractive indices were measured. About 0.5 mL from each of these two solutions was taken and mixed together to form a 1: 1 blend ratio of P3HT: PCBM by volume. The resulting solution from the two was ultra - sonicated for 10 minutes and its refractive index was measured. Another 20 mg of P3HT and PCBM were each dispersed in 5 mL of chloroform. The dispersions were again ultra - sonicated and refractive indices measured. A mixture of the two solutions was made in a 1: 1 ratio and refractive index measured. All the refractive indices were measured using the PAL - 3 refractometer.

4.1.2 Results and Discussion

The refractive index of pure Chloroform was n = 1.444. The refractive index of 20 mg of P3HT dissolved in 3 mL of chloroform was n = 1.449 whilst the refractive index of 20 mg of PCBM dissolved in 3 mL of chloroform was n = 1.451. The n value of the 1: 1 mixture of 0.5 mL of the P3HT solution and 0.5 mL of the PCBM solution in chloroform was n = 1.451. Similarly, the refractive of 20 mg of P3HT dissolved in 5 mL of chloroform was n = 1.449 whilst a similar solution of PCBM gave n = 1.449. The results are summarized in Table 4.1.

Table 4.1: Refractive indices of various preparations of P3HT, PCBM and PCBM: PCBM

Solution Type	mg/mL	Refractive index (*n*)
chloroform	0	1.444
P3HT	6.667	1.449
PCBM	6.667	1.451
P3HT: PCBM (1: 1)	6.667	1.451
P3HT	4.000	1.449
PCBM	4.000	1.451
P3HT: PCBM (1: 1)	4.000	1.451

By comparing the refractive index of chloroform at n = 1.444 and that of the solution with largest refractive index value of n = 1.451, it is clear that P3HT and PCBM as well as their mixtures are very soluble in chloroform. However, P3HT, with an n value of its solution closer to that of chloroform, is more readily soluble in chloroform compared to PCBM. The good solubility of P3HT: PCBM mixture in chloroform implied that a good blending of the two polymers was possible in this solvent. Good blending is desired in achieving good interaction of molecules at microscopic level. The refractometer used in this study could only measure the refractive indices of solution. As a result the measurement of refractive indices of thin films was not possible.

4.2 Surface Morphology and Band Gap Determination of Titanium Oxide thin films

Examination of surface morphology is used to measure the roughness of any given surface. The surface roughness of thin films is crucial to their performance in applications. For example, a rough surface reflects less of the incident photons and has better adhesion compared to a smooth surface. Atomic Force Microscopy (AFM) was employed to determine the surface morphology of the TiO_2 thin films, which were deposited by the e-beam technique. The band gap of the thin films was investigated by means of the

Tauc model from transmittance and reflectance data [59, 60]. The band gap size plays a crucial role in the photo-absorption performance of thin films. The determination of the band gap value also acts as a test of the integrity of the material under investigation. The details of the determinations are covered in the subsequent sections.

4.2.1 Experimental on e-bean deposition and AFM analysis of TiO_2 thin films

A thin film of TiO_2 was deposited on glass substrate by e-beam method. TiO_2 powder was placed on copper crucibles inside the e-beam chamber. The pressure inside the e-beam chamber was allowed to drop to about 6×10^{-6} Torr while the deposition rate was set to 2×10^{-5} per second. The low pressure was necessary to avoid unnecessary collisions of TiO_2 atoms with air molecules, which could have resulted in overheating and eventual damage to the chamber. The pressure of 6×10^{-6} Torr was reached only after pumping out air from the chamber for 48 hours. Parameters of the e-beam chamber were set which allowed the deposition of a thin film of 6 nm thickness. The thickness of 6 nm was, however, not verified by another method. The thin films of TiO_2 were later annealed in air in an oven for 5 hours at 400 ^oC. The annealing process helps in rearranging and reordering of particles within a thin film. The films formed were analyzed by means of AFM to determine the surface morphology in terms of root mean square roughness (RMSR).

4.2.2 Results and Discussion

Figure 4.1(A) shows 2D images of uncoated aluminium, as deposited TiO_2 thin film on aluminium, and annealed TiO_2 thin film on aluminium surfaces. The surface of uncoated aluminium is less rough compared to the surface of the TiO_2 coated aluminium. Thus, the presence of TiO_2 thin film on the aluminium surface increased the roughness of the surface. Additionally at microscopic level, the surface roughness of the as-deposited TiO_2 thin film was less than that of annealed TiO_2 film as can be seen of the analysis of

Figure 4.1 on Table 4.2. This result showed that the annealing process changed the orderliness of the particles in the thin film shown by the change in morphology.

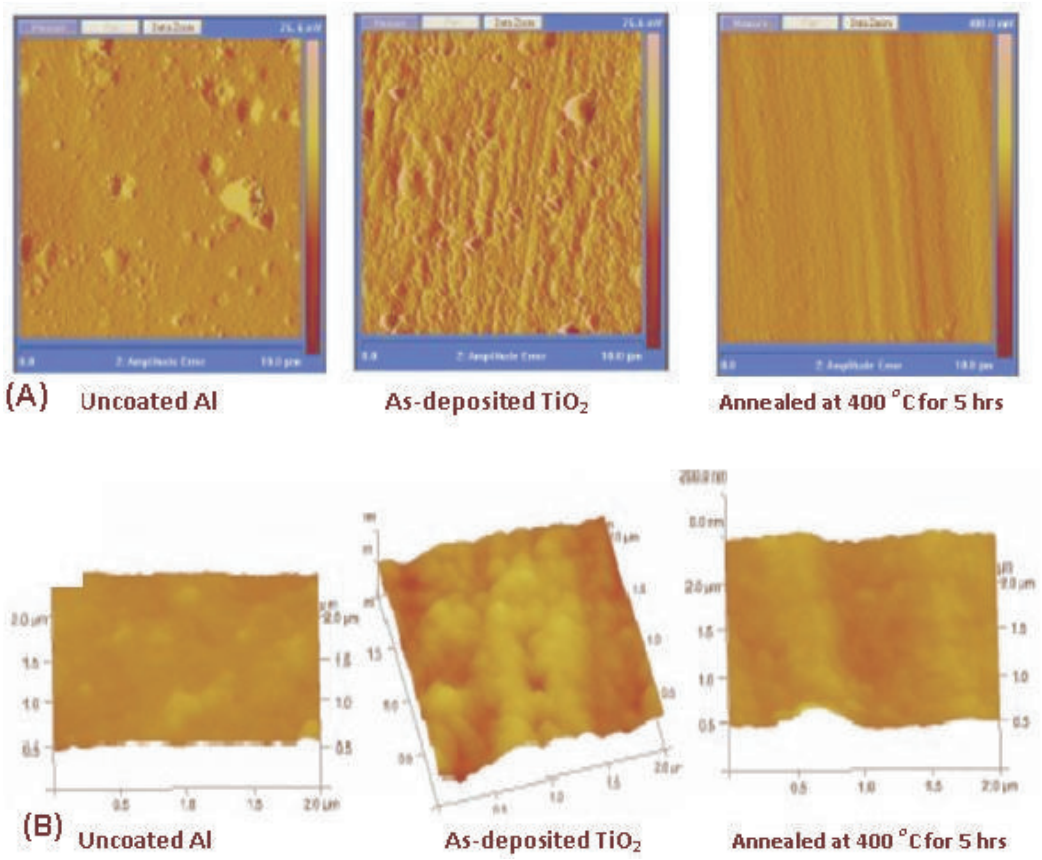


Figure 4.1: **(A)** 2D AFM images of uncoated Aluminium, as-deposited TiO_2 thin film, and annealed showing the surface roughness, and **(B)** 3D AFM images of uncoated Aluminium, as-deposited TiO_2 thin film and annealed showing the surface roughness.

Figure 4.1 (B) shows a 3D surface roughness of selected local areas of the same thin film and show that the TiO_2 coated aluminium are rougher compared to the uncoated one. The root mean square roughness of the uncoated aluminium, as-deposited TiO_2 thin film, and the annealed TiO_2 thin film (as obtained from the AFM instrument) are summarised in Table 4.2.

Table 4.2: Root Mean Square Roughness o TiO_2 thin films

	Root Mean Square Roughness (nm)		
	At 10 µm Magnification	At 5 µm Magnification	At 2 µm Magnification
Uncoated Al	34.9	10.1	4.3
TiO_2 as-deposited on Al	33.9	23.3	13.6
TiO_2 annealed at 400°C on Al for 5 hours	63.8	25.3	15.6

Table 4.2 shows that the root mean square roughness of the uncoated aluminium, as-deposited TiO_2 thin film, and the annealed TiO_2 thin film magnified at different levels. The roughness measured at 10 µm show almost the same level of roughness for the uncoated and as deposited. However, examination of images at higher magnification of 2 and 5 µm indicate substantial modification of surface roughness after coating with TiO_2. For example, the roughness for uncoated aluminium, as-deposited TiO_2 thin film, and annealed TiO_2 thin film at 2 µm magnification were 4.3, 13.6, and 15.60, respectively. The values show that coating and subsequent annealing resulted in increased surface roughness. Increased surface roughness after annealing of the films has been attributed to the formation of nano-rod following the annealing process [58, 59]. The large RMSR of annealed TiO_2 thin films are desired for good adhesion to other films such as polymer thin films, when used in solar cells.

4.2.3 Transmittance, Absorbance and Reflectance Characteristics of TiO_2 thin film and Band Gap Determination

The transmittance, absorbance and reflectance of the TiO_2 thin films were measured in the UV-Vis region. These three properties are important because they determine the performance of the thin film when used in a solar cell. For

TiO_2 thin films, high reflectance and low absorbance of photons are desirable if the thin film is to be used as a back reflector in the back electrode of a solar cell. Back reflection of photons enhances solar cell performance by allowing light that is transmitted through the upper layers to be reabsorbed when reflected back by the back electrode. In this case TiO_2 serves to enhance back reflection. The transmittance data also enables determination of the optical band gap. The need for the determination of the band gap has already been outlined in section 4.2. The experimental method and results are given in the sections that follow.

4.2.4 Experimental

The transmittance, absorbance and reflectance measurements were done by using of a UV-Vis CECIL, 2000 series instrument. The UV-Vis spectrophotometer was allowed to initialise with air as a reference medium. The TiO_2 thin films on glass substrates were then mounted onto a sample holder, one at a time. The UV-Vis instrument was programmed to scan starting from a minimum of 200 nm and ending at a maximum of 1100 nm wavelength. The results were later plotted using *Origin software*. The results and discussion are given in the subsequent sections.

4.2.5 Results and Discussion

The photon absorbance and transmittance curves of the 6 nm thick TiO_2 film are shown in Figure 4.2. Figure 4.2 (A) shows negligible absorbance due to the 6 nm TiO_2 thin film. On the other hand, Figure 4.2 (B) shows transmittance of above 90 % for the uncoated glass and a transmittance of about 80 % for the TiO_2 thin film coated glass, giving a reduction in transmission of about 10 %. The negligible absorbance observed in Figure 4.2 (A) is correlated by the high transmittance in Figure 4.2 (B) for both the plain glass and coated.

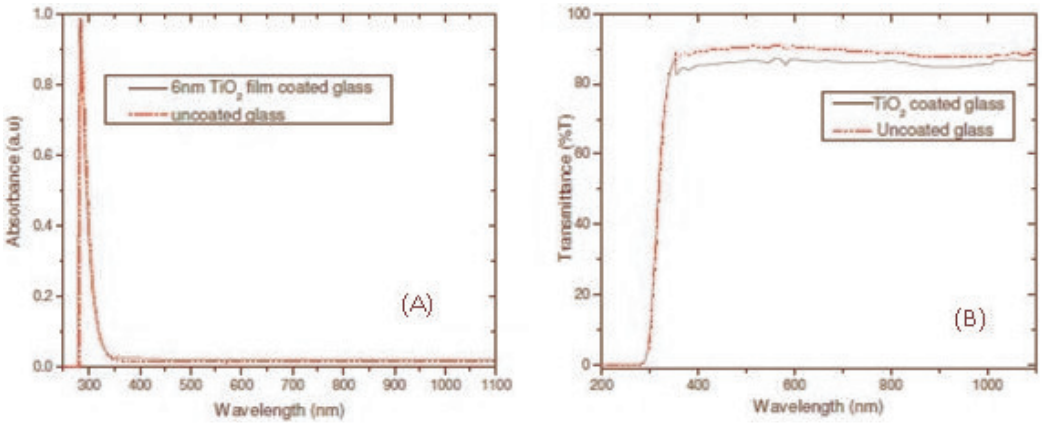


Figure 4. 2: (A) Absorbance curves of the uncoated and the 6 nm TiO_2 coated glass annealed at 400 ^oC for 5 hours, and **(B)** percentage transmittance curves of the uncoated and the 6 nm TiO_2 coated glass annealed at 400 ^oC for 5 hours

The reflectance curve as a percentage for the 6 nm thick TiO_2 film annealed at 400 ℃ for 5 hours is shown in Figure 4.3. The curve shows that the addition of TiO_2 thin film enhances the reflectivity of glass by about 10 %. This is desirable in a back reflector of a solar cell, which works to increases the efficiency of the cell.

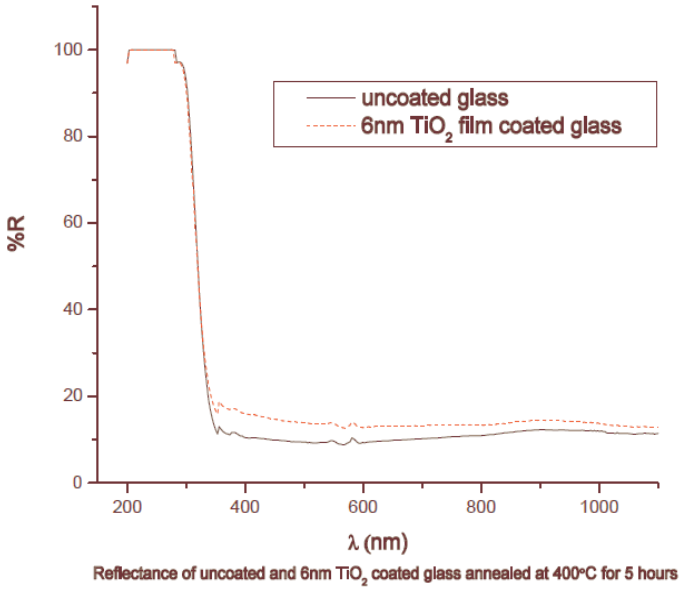


Figure 4.3: Reflectance curves of uncoated and the 6nm TiO_2 thin film coated glass annealed at 400 ^oC for 5 hours.

By using the values of transmittance from Figure 4.2 (B), the optical band gap value was calculated for TiO_2 thin films. The optical band gap was determined

by an indirect method from Tauc Model which employed Equation (4.2) [59 - 61].

$$\alpha h\nu = A\left(h\nu - E_g\right)^n \quad (4.2)$$

Where α is the absorption coefficient, hν is the photon energy in electron volts (eV), E_g is the optical band gap, A is a factor which does not depend on photon energy but on the transition probability and can be assumed to be constant within the optical frequency range, and n has four numerical values (1/2 for allowed direct, 2 for allowed indirect, 3 for forbidden direct and 3/2 for forbidden indirect electronic transitions in the **K**-space) [61].

To determine the band gap, a plot of $(\alpha h\nu)^{1/n}$ against $h\nu$ is necessary. The equation (4.3) can be re-written to

$$(\alpha h\nu)^{1/n} = B(h\nu - E_g) \quad (4.3)$$

Here, $B = A^{1/n} =$ constant. The values of α(λ) can also be obtained from the transmission (T) data by means of Equation (4.4) [62].

$$\alpha(\lambda) = \frac{\ln\left(1/T(\lambda)\right)}{d} \quad (4.4)$$

Where *d* is the film thickness in nanometres. An extrapolation of a straight line through $(\alpha h\nu)^{1/n}$ cutting $h\nu$ at $(\alpha h\nu)^{1/n} = 0$ gives the approximate values of E_g for the Forbidden Indirect, Allowed Indirect, Allowed Direct, and Forbidden Direct transitions for the different values of n, accordingly. The technique and values obtained are shown in graphs A, B, C, and D of Figure 4.4 for the 6 nm TiO_2 thin film annealed at 400 ºC for 5 hours in air. The relationship between α(λ) and $h\nu$ (eV) is also plotted in graph E of Figure 4.4.

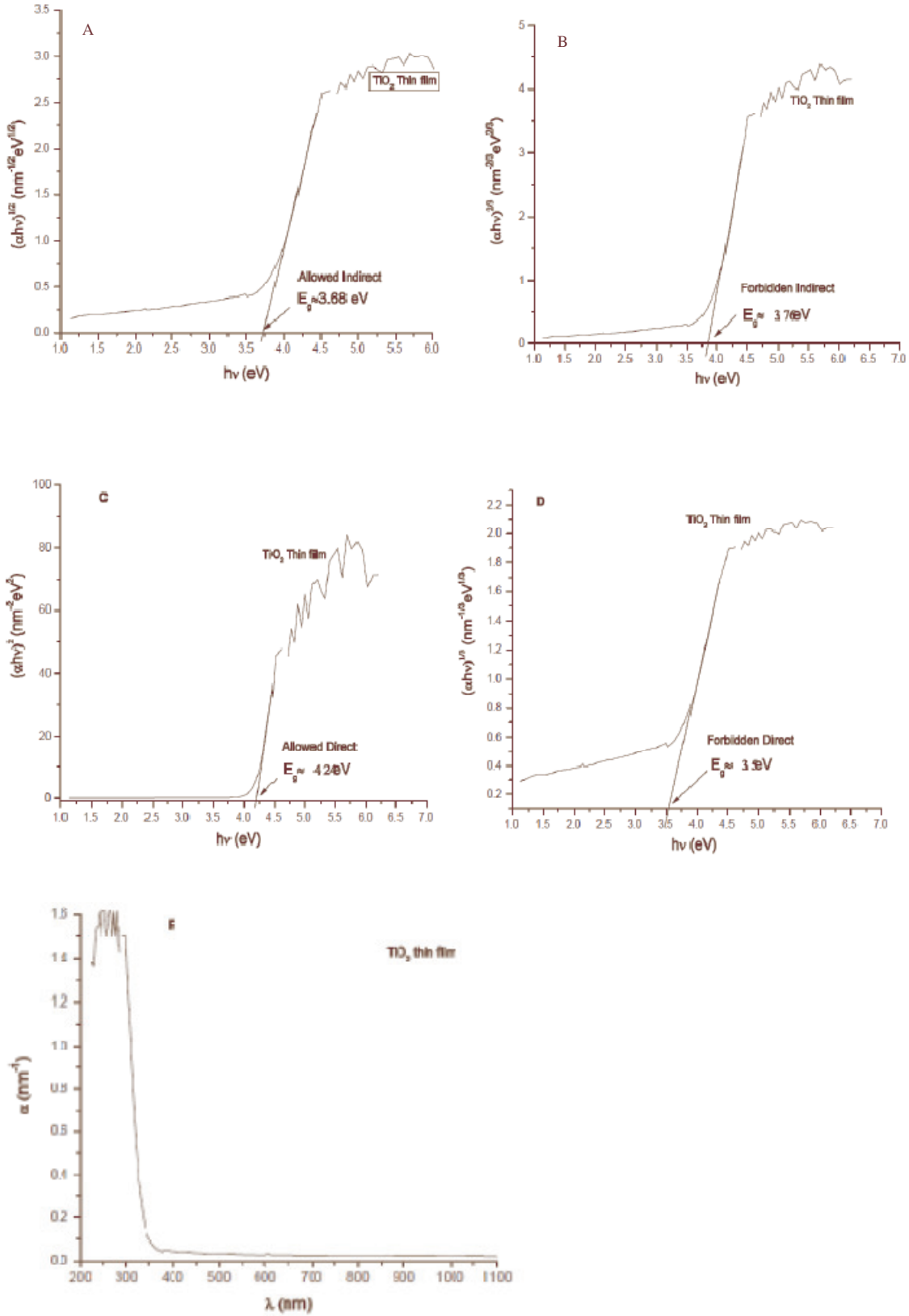


Figure 4.4: Various Band Gap Values Determination (**A**) - (**D**) of TiO_2 thin films, and (**E**) relation between absorption coefficient $\alpha(\lambda)$ and wavelength (λ).

The values obtained from Figure 4.4 are summarized in Table 4.3.

Table 4.3: Various values of determined band gaps in TiO_2 thin film

Allowed indirect	Allowed direct	forbidden indirect	forbidden direct
3.6 eV	4.2 eV	3.7 eV	3.5 eV

In semiconducting materials, conduction occurs through either allowed direct or allowed indirect band gap, depending on which of the two is smaller. A smaller value of band gap is preferred for conduction because it requires less energy for an electron to cross the band gap as it moves from the valence band to conduction band. From these values of band gap obtained, it is clear that conduction in TiO_2 thin films annealed at 400 ºC for 5 hours, like in other amorphous materials, is through indirect allowed band gap and has a value of $E_g \approx 3.68$ eV. This value is consistent with reported value of 3.5 eV for TiO_2 [60, 61]. The behaviour of the absorption coefficient, $\alpha(\lambda)$, in Figure 4.4 (E) is consistent with the absorbance graph of Figure 4.2 (A).

4.3 Optimization of Blend Ratios and Annealing Temperatures of P3HT: PCBM Thin Films

In order to increase the power conversion efficiency of the solar cells, fabrication parameters must be optimized. The main two parameters that needed optimization are blend ratios and annealing temperatures of the polymers during the fabrication process. Various blend ratios were considered within the range of 1: 0.80 to 1: 1.00 of P3HT: PCBM. The Blend ratio with the highest photon absorbance was considered to be the optimum of the blend ratios. Similarly, various annealing temperatures were considered within the range of 25 ℃ to 160 ℃. The annealing temperature that produced the highest absorbance was considered to be the optimum for that blend ratio. The thin film deposition process and the results of the optimizations are discussed in details in the sections that follow.

4.3.1 Spin Coating on Glass Experimental

To find the optimum blend ratio and annealing temperature of P3HT to PCBM, different weight ratios were considered for each 50 mg of P3HT as follows: 1: 1, 1: 0.98, 1: 0.96, 1: 0.94, 1: 0.92, 1: 0.90, 1: 0.88, 1: 0.86, 1: 0.84, 1: 0.82, and 1: 0.80 of P3HT:PCBM. The mixtures with different weight ratios were then dissolved in 5 mL of Chloroform each and blended using a shaker for 6 minutes running at 2500 rpm. The containers used for the different blend ratios were filled with argon gas prior to being used to provide an inert atmosphere. These containers with the blends were then covered with aluminium foil to keep out light and stored in a dark place. The blends were kept for 4 days and shaken each day before spin coating was done. Thin films of the solution of P3HT: C_{60}-PCBM in Chloroform was spin coated on glass substrates at 1000 rpm for 10 seconds.

4.3.2 Spin Coating Results and Discussion

During the spin coating process, the speed of the coater was kept at same speed hence it is assumed that the film thicknesses for all the blend ratios were the same. The thin films coating exhibited good adhesion to the substrates and were observed to have shiny surfaces. The UV-Vis results and analysis from the thin films are shown and discussed in the subsequent sections.

4.3.3 UV-Vis Characterization Experimental

Following deposition by spinning coating, the films were then analysed for photo-absorbance, transmittance, and reflectance before and after annealing at different temperatures. The UV-Vis measurements were done using a CECIL, 2000 series UV-Vis instrument. The measurements mainly focused on photo-absorbance since the main objective of this study was to optimise the photon absorbance for these polymer materials.

4.3.4 Results and Discussion

The results in Figure 4.5 of the as-deposited thin films show that P3HT has higher photo-absorbance as compared to the films of different blend ratio. The as-deposited P3HT thin film has a maximum peak at 551 nm wavelength whilst those of blends have maximum peaks at about 500 nm wavelength. The shifting in peak position to shorter wavelengths, exhibited by blends, can be attributed to the effect of PCBM on P3HT. Pure PCBM has high absorbance in the short wavelengths. The maximum absorbance values for the blend ratios from Figure 4.5 are shown in Table 4.4.

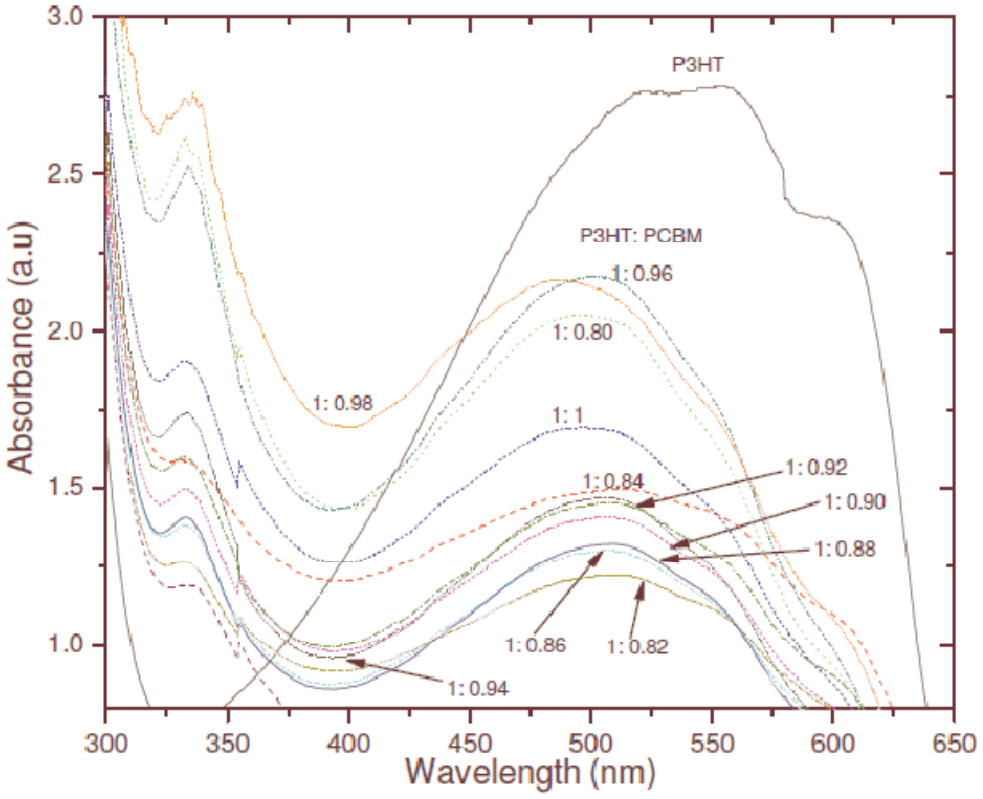


Figure 4.5: Photo-absorbance of various P3HT:PCBM blend ratios of the as-deposited films.

Table 4.4: Blend ratio values and their corresponding absorbance maximum values

Blend Ratio of P3HT: PCBM	Maximum Absorbance as-deposited
1: 0.80	2.0535
1: 0.82	1.2241
1: 0.84	1.5028
1: 0.86	1.3043
1: 0.88	1.3293
1: 0.90	1.4101
1: 0.92	1.4565
1: 0.94	1.4734
1: 0.96	2.1763
1: 0.98	2.1675
1: 1.00	1.694

A plot of the maximum absorbance values from Table 4.4 is shown in Figure 4.6 and shows that the optimum blend ratio for the as-deposited is 1: 0.96. The graph shows photo-absorbance characterized by an initial high value at 1: 0.80 followed by a sudden fall at 1: 0.82 then a small rise forming a 'hump' at 1: 0.84. The absorbance increases nearly linearly from 1: 0.86 through to 1: 0.94 followed by a sharp rise at 1: 0.96. The absorbance falls after 1: 0.96.

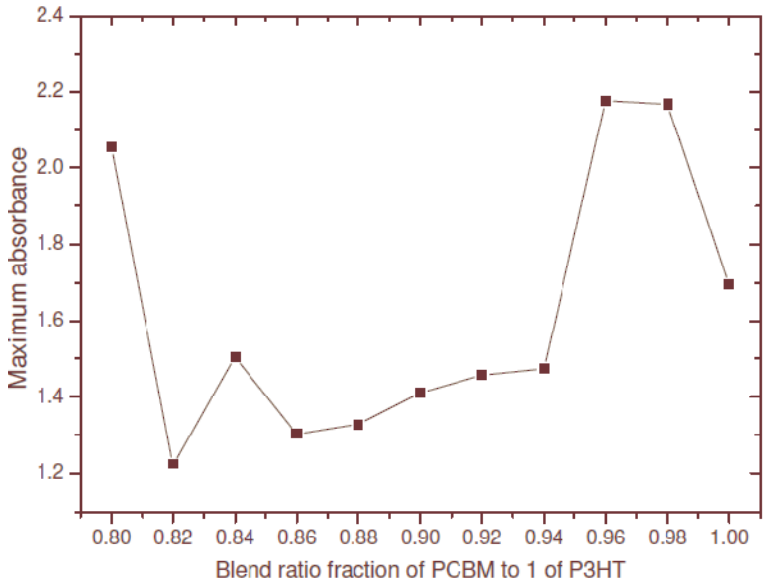


Figure 4.6: Maximum photon absorbance of various blend ratio fractions of PCBM to 1 of P3HT

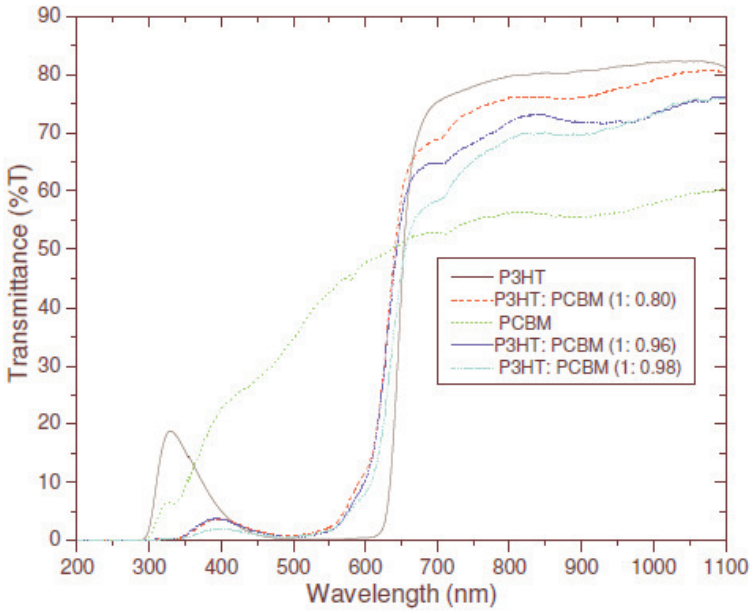


Figure 4.7: Photon transmittance of selected blends of P3HT: PCBM as deposited films

Figure 4.7 shows the transmittance of P3HT and selected blends. The figure reveals that photon transmittance in P3HT between 500 nm and 600 nm wavelengths is approximately zero. This implies that about 5 % of the solar radiation not absorbed (as can be obtained from Figure 4.5) is due to reflectance at the surface of the as-deposited P3HT thin films. This is supported by the fact that the as-deposited thin films were observed to have shiner surfaces compared to the annealed ones.

The results of evaluating the effect of annealing at different temperatures of various blend rations are shown in Figure 4.8 (B1-B3). Figure 4.8 (B1) shows that the absorbance of 1: 0.96 blend ratio approaches that of pure P3HT at 100 $^{\circ}$C annealing temperature. The absorbance of 1: 0.96 blend ratio showed a fall at 110 $^{\circ}$C while that of P3HT increased. The increase in absorbance observed in P3HT films annealed at 110 $^{\circ}$C can be attributed to P3HT's increase in the crystalline form [3, 9]. The blend ratios 1: 0.96 and 1: 0.80 show significant increase in absorbance at 130 $^{\circ}$C compared to the rest of the blends as can be seen from Figure 4.8 (B3). P3HT shows further increase in absorbance as it continues to crystallize at 130 $^{\circ}$C. Most of the blend ratios were observed to exhibit good absorbance at 130 $^{\circ}$C and thus this

temperature can be regarded as the common favourable temperature for the blend ratios.

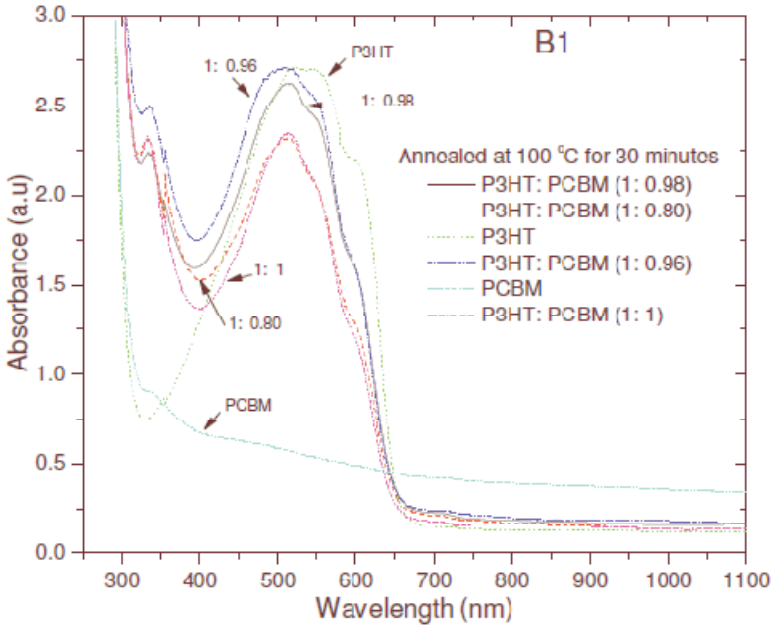


Figure 4.8 (B1): Photon Absorbance of various blends annealed at 100 °C

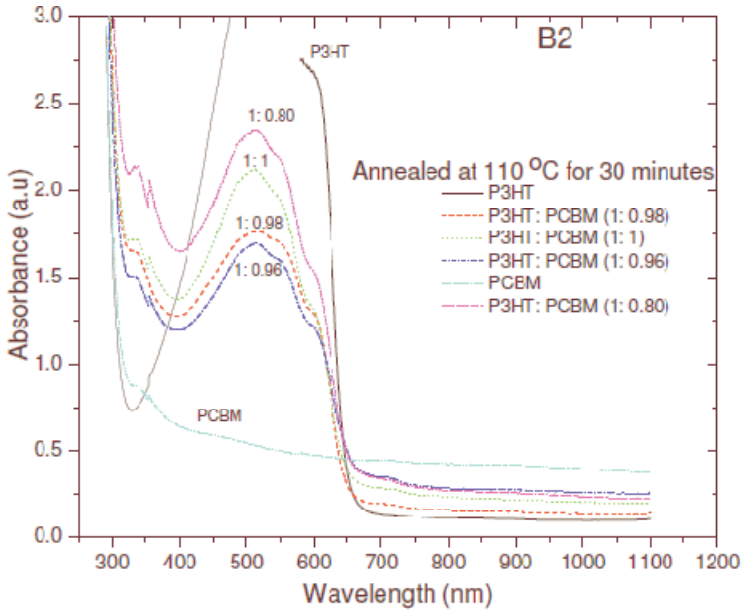


Figure 4. 8 (B2): Photon Absorbance of various blends annealed at 110 °C

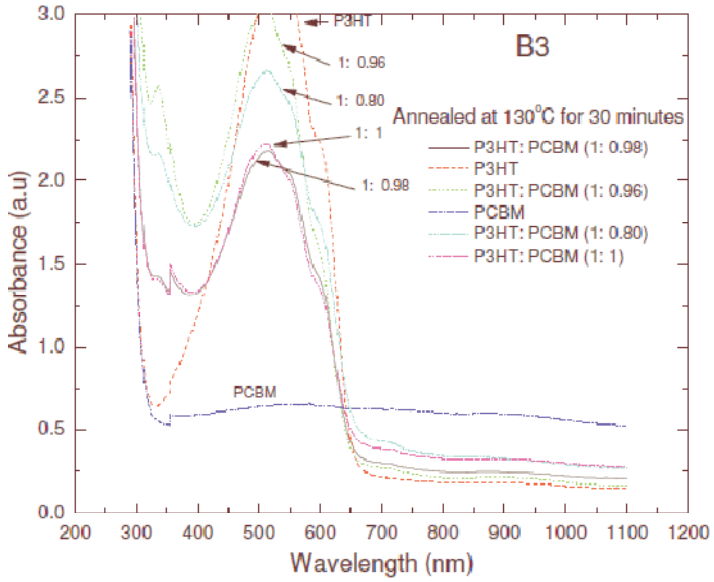


Figure 4. 8 (B3): Photon Absorbance of various blends annealed at and 130 °C

Figure 4.9 shows the photon absorbance of six selected blends annealed at 160 ℃. The absorbance of 1: 0.96 blend ratio is close to 100 %, slightly higher than that of pristine P3HT. It is observed that the performance of P3HT begins to decrease at 160 ºC whist PCBM remains almost constant. Selected blend ratios are plotted in Figure 5.9 and are observed that to have maximum absorbance values above 80 % at 160 ºC annealing temperature.

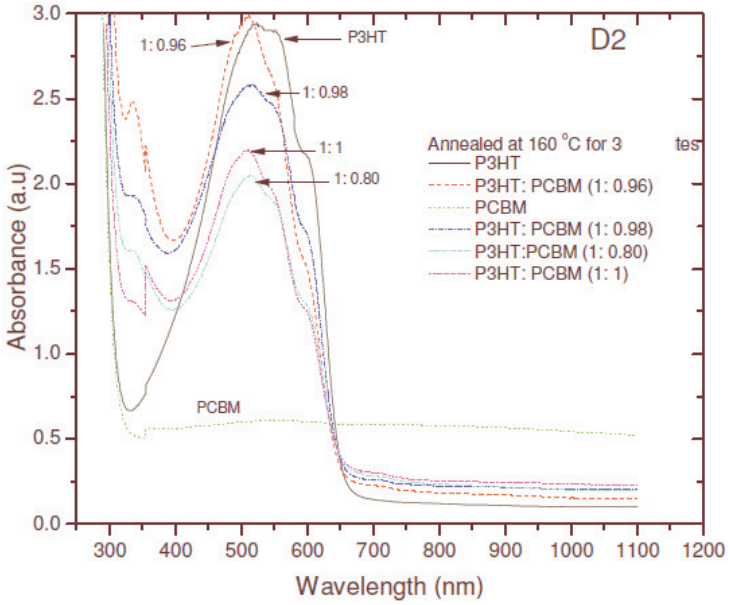


Figure 4.9: Photon Absorbance of various blends at 155 (D1), 160 (D2 and D3), and 165 °C (D4)

The other graph for the 135 ℃, 140 ℃, 145 ℃, and 150 ℃ annealing temperatures are given in Appendix B.

The behaviours of pristine P3HT and PCBM in relation to annealing temperature are shown in Figure 4.10.1 and Figure 4.10.2, respectively. From the two figures, it was observed that the change in photon absorbance in pristine P3HT and pristine PCBM before and after annealing was not significant.

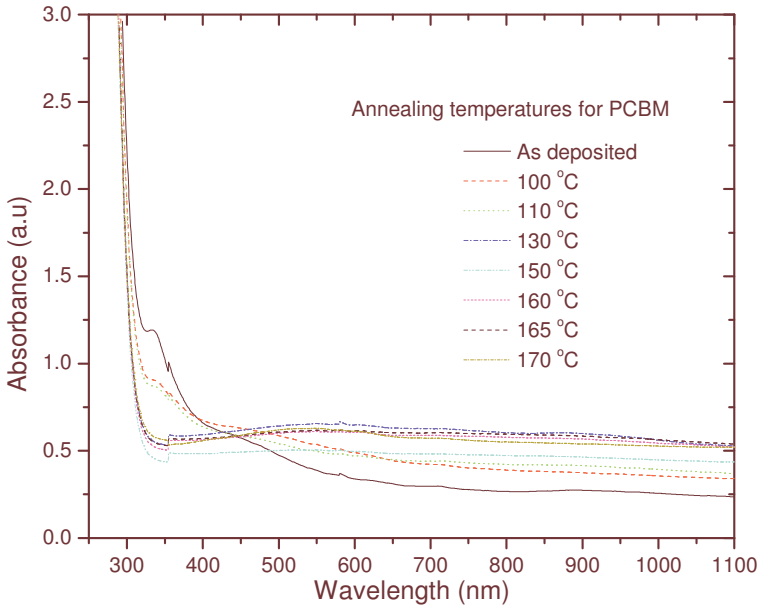


Figure 4.10.1: Photo-absorbance of pristine P3HT at different annealing temperatures.

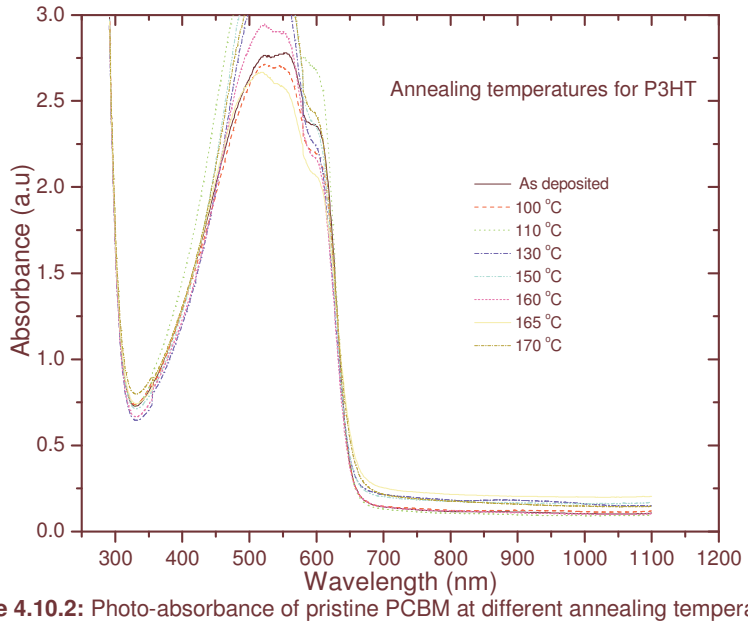


Figure 4.10.2: Photo-absorbance of pristine PCBM at different annealing temperatures

Figure 4.11 E1 to E5 shows the behaviour for different blend ratios between 1: 0.80 and 1: 1. The optimum annealing temperature for both pristine P3HT and pristine PCBM thin films is 130 ℃ as indicated by the graphs in Figure 4.11 E1 through E5.

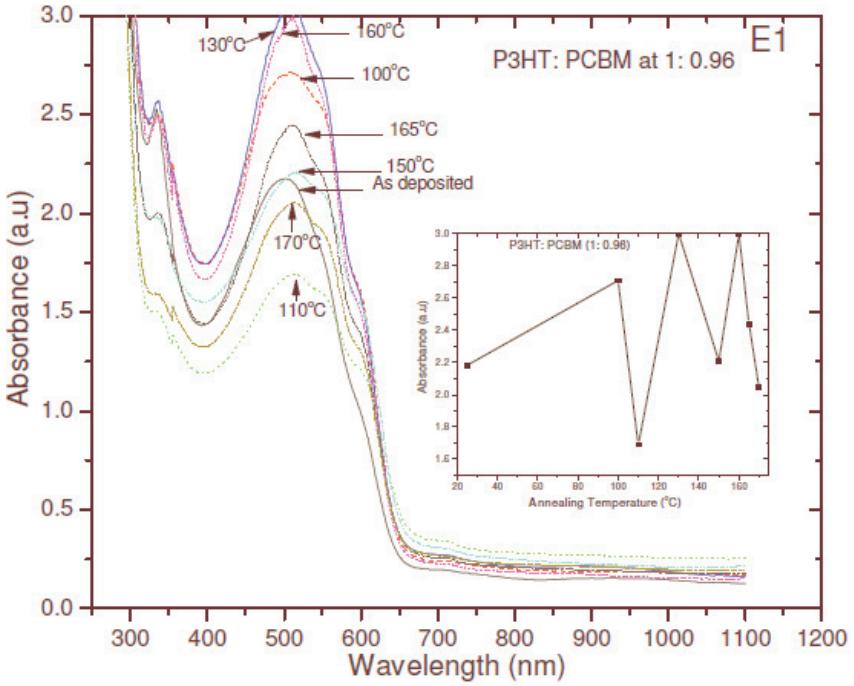


Figure 4.11 (E1): Photon Absorbance of 1: 0.96 blend at different annealing temperatures

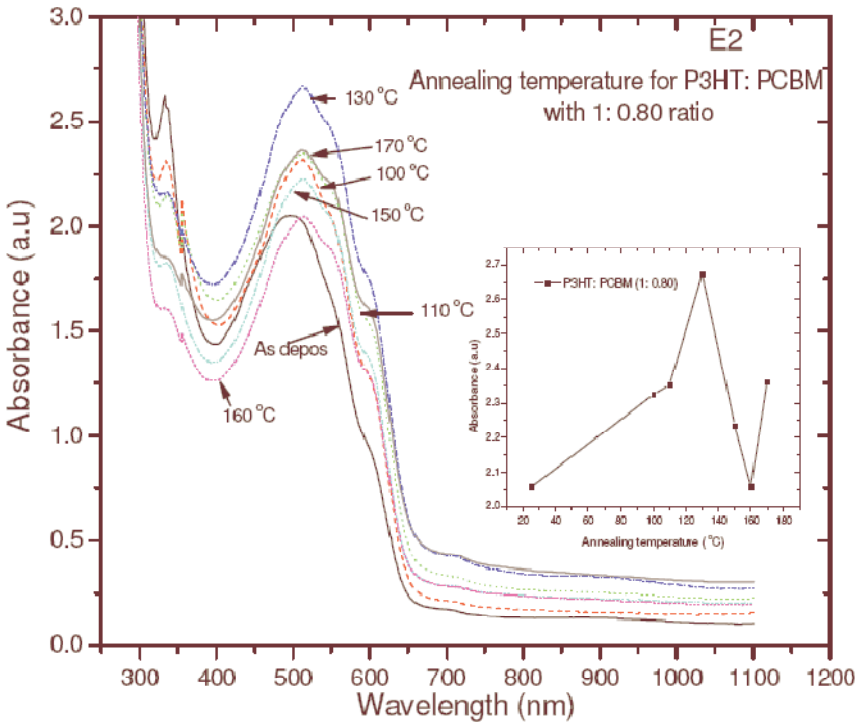


Figure 4.11 (E2): Photon Absorbance of 1: 0.80 blend at different annealing temperatures

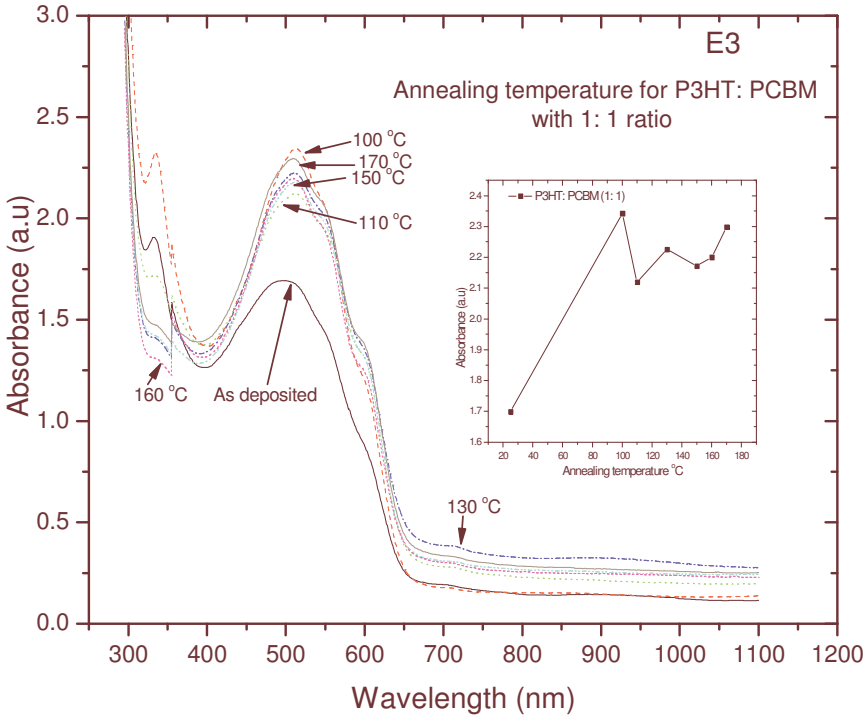


Figure 4.11 (E3): Photon Absorbance of 1: 1 blend at different annealing temperatures

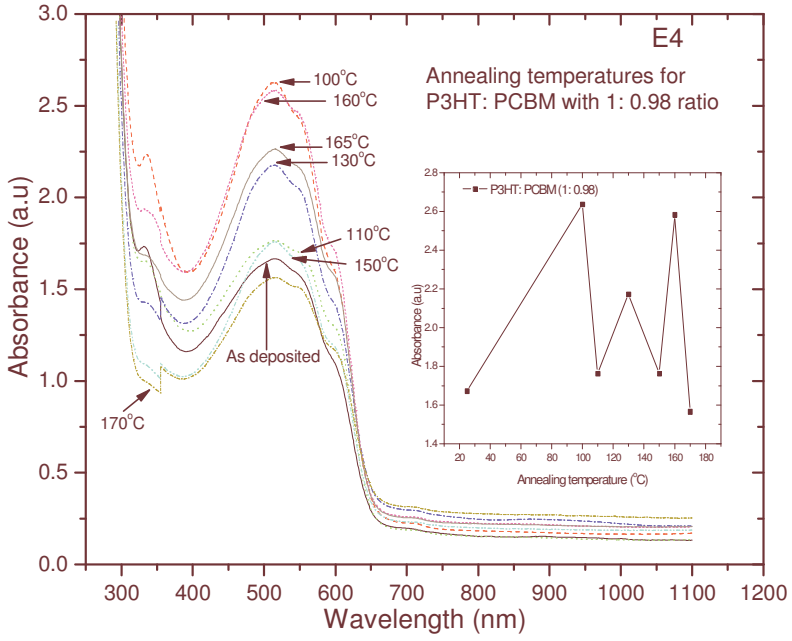


Figure 4.11 (E4): Photon Absorbance of 1: 0.98 blend at different annealing temperatures

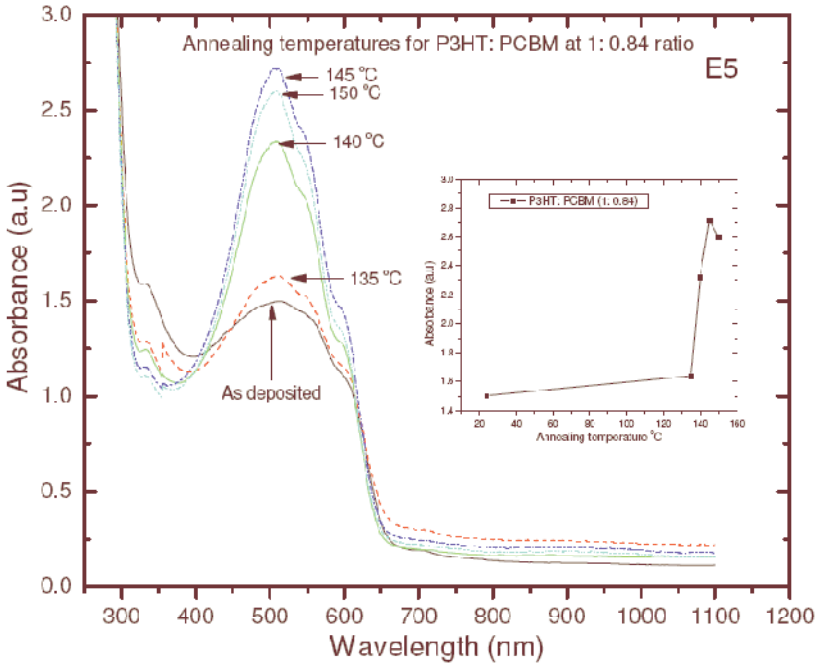


Figure 4.11 (E5): Photon Absorbance of 1: 0.84 blend at different annealing temperatures

From Figure 4.11, it is clear that the dependence of absorbance on annealing temperature is non-linear. To further explore the temperature-absorbance dependence, Table 4.5 shows data of the blend ratio, the associated optimum temperature, and absorbance values investigated in this study. Figure 4.12 shows the two graphs of optimum annealing temperature (A) and absorbance (B) for all the blend ratios.

Table 4.5: Optimum temperature and absorbance of each blend ratio

Blend ratio fraction of PCBM to 1 of P3HT	Optimum Annealing Temperature (℃)	Optimum Absorbance percentage (%)
0.80	130	88.80
0.82	140	51.03
0.84	145	90.23
0.86	150	76.03
0.88	155	55.17
0.90	165	62.03
0.92	160	58.77
0.94	135	74.83
0.96	130	100.00
0.98	115	87.60
1.00	100	78.37

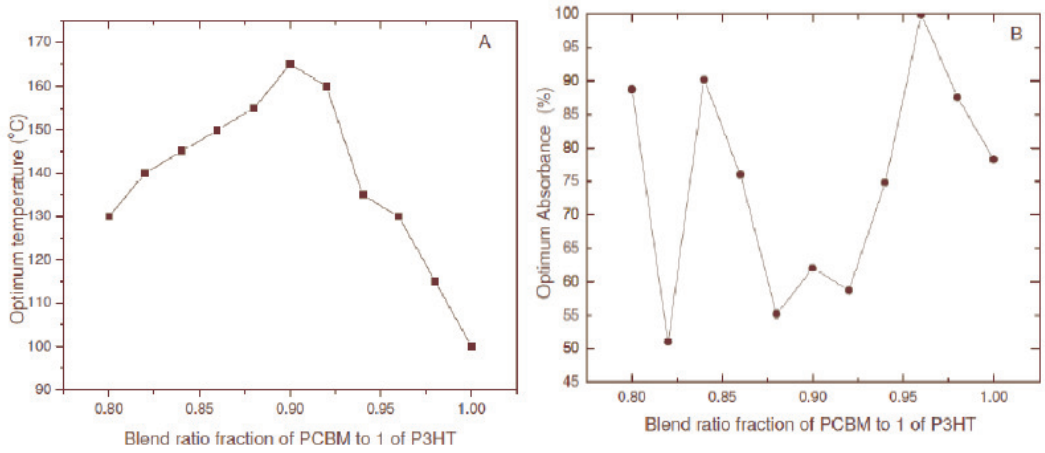


Figure 4.12: Optimum annealing temperature (**A**) and optimum absorbance (**B**) for different blend ratios. The graphs are derived from Table 4.5.

From Figure 4.12 *A* it is seen that each blend ratio of P3HT:PCBM has its own optimum annealing temperature and each blend ratio has a different optimum absorbance value. This can be explained from the understanding that each blend ratio has a unique glass transition and melting temperatures. Figure 4.12 *A* also shows that optimum annealing temperature increases with the increase in PCBM concentration until at 0.90 at which it begins to fall. Furthermore, the highest optimum annealing temperature for these organic blends was found to be at about 165º C corresponding to the 1:0.90 ratio. However, the highest optimized absorbance was about 99.99% and corresponded to the 1:0.96 at 130 ºC (Figure 4.12 *B*), and agrees with results by other scholars that found the optimal weight ratio for P3HT:PCBM was between 1:0.9 and 1:1 and an optimum annealing temperature of 130 ºC [3, 9].

4.4 Construction and Evaluation of the Optimized P3HT: PCBM Solar Cells

The solar cells were constructed and evaluated from the optimized P3HT: PCBM of 1: 0.96 blend ratio. The cells construction were done on both glass and aluminium substrates and cells were then compared for power conversion efficiency.

4.4.1 Construction of Solar Cells Experimental

Before constructing the cells, the substrates of aluminium and glass were prepared by cleaning using ethanol and acetone. Etching was done using acid to remove foreign particles and the unwanted layer of aluminium oxide from the aluminium. Thin film layers were then deposited on the substrates by using e-beam and spin coating methods. The details of the experimental are shown in the sections that follow.

4.4.2 Aluminium and Glass Substrate Preparation before Deposition

To remove Al_2O_3 from Al metal substrate, the Al substrates were first heated in a mixture of 10 mL of NaOH and 50 mL distilled H_2O at a temperature of about 60 ºC for 10 minutes. The Al substrates were then removed from the hot mixture and immersed in ethanol for 10 minutes. The Al_2O_3 thin film layers were then pilled off by hand or with help of forceps leaving a clean surface of Al metal.

The clean Al substrates were immediately stored in an inert environment prior to use. The inert environment is necessary to avoid Al_2O_3 re-forming on the clean Al substrates. This method of removing Al_2O_3 layer was observed to be more efficient than generally reported methods. The glass substrates were cleaned using acetone rinsed in ethanol and then stored in a clean environment before thin films were deposited. Preparation and conditioning of the aluminium substrate was followed by deposition of Mg, Ag, and TiO_2 layers of thin films.

The active layer, consisting of P3HT/PCBM blend was subsequently added and was followed by the addition of two thin layers of PEDOT: PSS and ITO. The materials forming the cathode layers were deposited using physical vapour e-beam method whilst the active and anode layers were deposited by the spin coating method. The architecture of the resultant cell is shown in Figure 4.13.

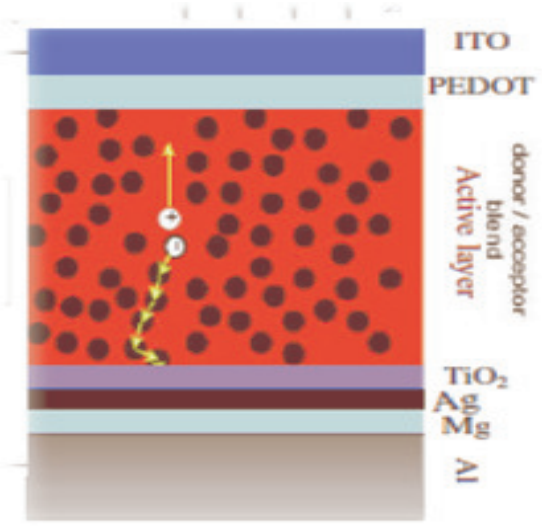


Figure 4.13: Typical Solar Cell Structure for the Optimized P3HT: PCBM Blend Ratio

4.4.3 Deposition of the Cathode Materials on Aluminium Substrate by the Physical Vapour e- Beam Method

The cathode materials consisted of aluminium (Al), magnesium (Mg), silver (Ag), and titanium oxide (TiO_2) as shown in Figure 4.13. A 200 nm thin film of magnesium (Mg) was deposited on 1 mm of aluminium followed by a 20 nm thin film of silver (Ag) and 6 nm thin film of TiO_2. These were deposited under air partial pressure of about 1 $X10^{-6}$ Torr. The cathode architecture is shown in Figure 4.14.

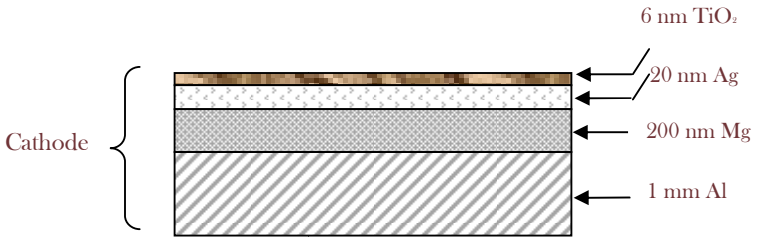


Figure 4.14: Cathode thin film layers for the P3HT: PCBM solar cells

4.4.4 Deposition of the Active Layer and Anode Materials by Spin Coating Method on Aluminium Substrate

The active layer to be deposited, P3HT: PCBM, blend ratio of 1: 0.96, was dissolved in 5 mL of chloroform and the thin films deposited using a spin coater. The detailed procedure is described in Section 4.3 while that of the spin coating technique is in Appendix A. The P3HT: PCBM blend was coated on top of the TiO_2 layer at spin speed of 1000 rpm for 10 seconds. In order to increase the wettability of PEDOT: PSS on P3HT: PCBM, a dilute solution of 1: 20 volume of PEDOT: PSS to ethanol was used. The dilute solution was prepared by dropping the aqueous PEDOT: PSS solution slowly into the alcohol while stirring vigorously. The spin conditions inside the spin coater were kept at room temperature and pressure. The P3HT: PCBM blend was then spin coated on top of the TiO_2 film at a spin speed of 1000 rpm for 10 seconds. The resulting thin film was then annealed at a temperature of 130 ℃ for 1 hour to allow crystallization to take place. The temperature of 130 ℃ the optimum temperature for the crystallization of the 1: 0.96 blend ratio.

The PEDOT: PSS thin film of about 80 nm thickness was deposited by spinning on top of the P3HT: PCBM layer at a speed of 1800 rpm for 10 seconds. The resulting thin film was then annealed at 130 ℃ for 1 hour. An ITO thin film was then spin coated on top of the PEDOT: PSS layer to a thickness of 100 nm at a speed of about 1000 rpm for 10 seconds. The resulting thin film was later annealed at 100 ℃ for 1 hour.

The resulting solar cells were then stored in an air tight container under Nitrogen atmosphere and kept in a dark room at room temperature. This was done to prevent degradation of the cell since OPV degrade exponentially in the presence of oxygen and strong light intensity.

4.4.5 Deposition of the Solar Cell layers on Glass Substrates

The preparation and conditioning of the glass substrates was followed by the deposition of the anode layers, which consisted of ITO and PEDOT: PSS thin

film layers. These layers were deposited on the substrates by spinning the solutions from these materials. An ITO thin film was first coated on glass substrate and annealed at 150 ℃ for 1 hour. A PEDOT: PSS thin film of about 80 nm was then spin coated on top of the ITO thin film and annealed at 100 ℃ for 1 hour to allow it to crystallise. The active layer of optimized P3HT: PCBM was later deposited on top of the PEDOD: PSS thin film using spin coating method. The cathode materials for the glass substrate consisted of TiO_2 and vanadium, which were deposited by the physical vapour e-beam method under air partial pressure of 1×10^{-6} Torr. The resulting solar cells were treated in the same way as the ones prepared from aluminium substrate. The solar cells were later evaluated for power conversion efficiency as described in the sections below

4.4.6 Evaluation of Solar Cells for Power Conversion Efficiency

A solar simulator (Figure 4.15) with an intensity of 53 mW/cm^2 was used to illuminate the cells at a standard temperature of 25 ℃ and AM 1.5. A Keitley, 2400 series source meter, was used to collect the current – voltage (I - V) data.

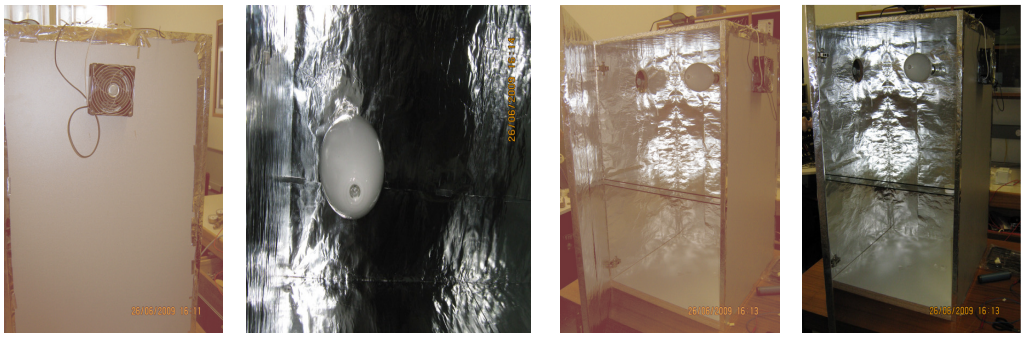


Figure 4.15: A solar simulator with an intensity of 53mW/cm^2

4.4.7 Results and Discussion

Figure 4.16 shows the I – V characteristic curve for a typical solar cell based on 1: 0.96 blend ratio of P3HT: PCBM. The I – V curve was plotted from data collected using the 2400 series Keitley source meter instrument. The voltage values were set on the instrument and increased step by step, and the corresponding current determined.

The I – V characteristic data under dark condition was collected initially, which was followed by the I – V characteristic data under luminous condition. The dark condition I – V characteristic data was collected inside the solar simulator with lamp turned off whilst the luminous condition I – V characteristic data was collected with the lamp turned on inside the simulator. The data collected under dark condition was later subtracted from that collected under illumination, as a correction. The resulting data was then plotted in Figure 4.16 to determine the power conversion efficiency.

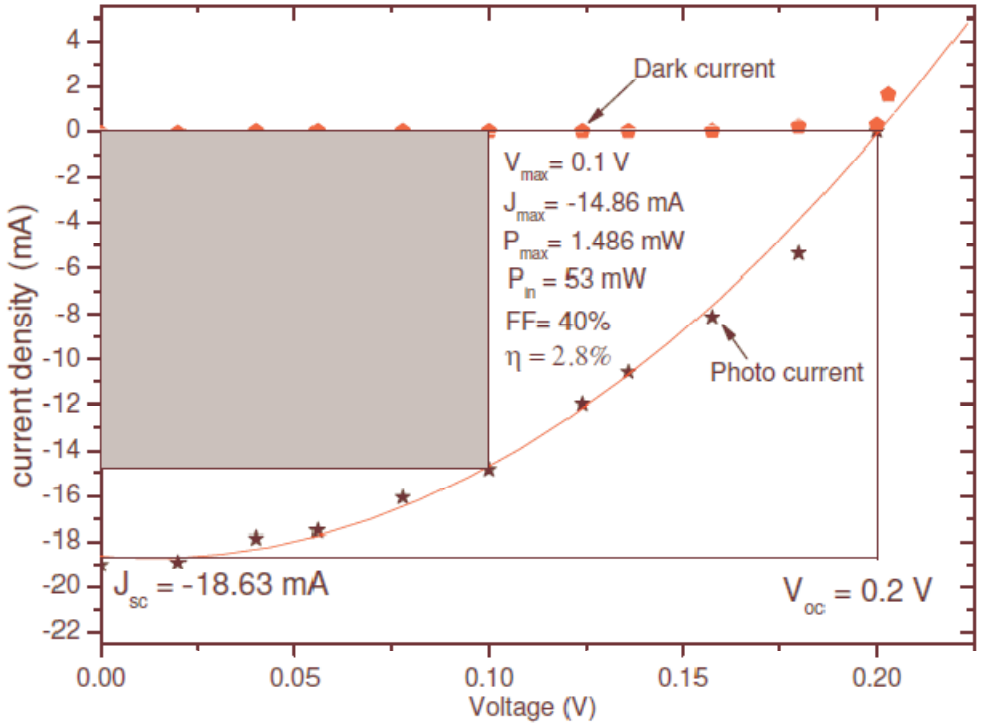


Figure 4.16: I – V characteristic curve of P3HT: PCBM (1: 0.96) solar cell.

The solar cells built on aluminium substrates gave a typical open circuit voltage (V_{oc}) of 0.2 V and short circuit current density (J_{sc}) of -18.63 mA. The maximum voltage (V_{max}) produced was 0.1 V whilst the maximum current was -14.86 mA, which produced a maximum power (P_{max}) of 1.486 mW. A typical fill factor (FF) of 40 % was obtained from the solar cells built on aluminium substrates which resulted into power conversion efficiency (η) of 2.8 %. On the other hand, the solar cells built on glass substrates gave a typical FF of 23 % and power conversion efficiency of 1.9 %.

The higher power conversion efficiency of 2.8 % attained by solar cells built on aluminium substrates can be attributed to the use of aluminium as substrate and the inclusion of the Mg thin film on top of the aluminium to enhance the low work function of the cathode. The use of TiO_2 as back reflector on the cathode could have also helped to increase the efficiency by allowing photon re-absorption as has been reported in other literature [1, 2].

Chapter 5

Conclusion and Further Work

5.1 Conclusion

The XRD results on ITO powder confirmed the presence of indium (In) and oxygen (O) molecules. The presence of tin (Sn) molecules was not detected because of the low doping percentage of 10 % of tin oxide (SnO_2) in ITO, which was consistent with literature. The XRD results on TiO_2 revealed the presence of rutile forms of TiO_2 and the resulting spectrum from the sample matched with that of the typical “finger print” spectrum of TiO_2, confirming the integrity of the TiO_2 powder. The XRD spectra results of P3HT and PCBM were not compared with the typical “finger print” spectra of these materials due to the non-availability of the XRD spectra in the database for these particular materials.

The FTIR results of P3HT powder revealed the presence of C = C carbon double bonds and aliphatic CH_2 bonds stretching vibrations. The presence of C - S and C - H deformations vibrations which were also detected at specific vibration wavelength provided evidence of the presence of these functional groups and were consistent with the chemical structure of P3HT. This confirmed the integrity of the P3HT nanopowder. The FTIR spectrum of PCBM revealed a strong presence of C - H, CH_2 and C - O bonds. The presence of these absorption bands at the specified frequencies was consistent with that of PCBM and hence confirmed its integrity. The FTIR spectrum for TiO_2 revealed the presence of both rutile and anatase forms of TiO_2 indicating that the powder was not pure rutile but a mixture of the two forms. The FTIR spectrum for ITO powder showed the presence of both In - O

and Sn-O vibrations consistent with the material composition of the ITO powder.

The HR - TEM results for ITO, and TiO_2 and PCBM showed the presence of particle agglomeration. This made size calculation difficult and hence the values obtained were only approximations. The TEM results also showed the particles in ITO and TiO_2 were typically in form nano-rods whilst the micrographs for PCBM show the presence of nano-sheets and nano-tablets.

The TiO_2 thin films deposited by e-beam method and annealed at 400 ℃ was found to be conducting through allowed indirect band gap of 3.6 eV. The conduction through allowed indirect band gap confirmed that the thin film was in amorphous form. Morphology study of the annealed TiO_2 thin film showed a mean square roughness of 63.8 whilst that of uncoated Al was 34.9 a.u at 10 µm magnification by AFM microscopy. The addition of the TiO_2 thin film was therefore found to double the surface roughness of aluminium. For thin films of P3HT: PCBM blend ratios that were deposited by spin coating method and optimized through annealing, the best photon absorbance was found to be that of 1: 0.96 blend ratio annealed at a temperature of 130 ^{o}C. The absorbance performance was followed by 1: 0.84, then by 1: 0.80 blends at 145 ^{o}C and 130 ^{o}C annealing temperatures respectively. The annealing temperature dependence of each blend ratio with respect to photon absorbance was found to be non-linear. Each blend ratio was found to have its own optimum annealing temperature. The UV-Vis results showed that the majority of the blend ratios had a common high photon absorbance at 130 ºC.

The solar cells built on aluminium substrates gave a typical open circuit voltage 0.2 V and short circuit current density of -18.63 mA. The maximum voltage produced was 0.1 V whilst the maximum current was -14.86 mA, which produced a maximum power of 1.486 mW. A typical fill factor of 40 % was obtained from this type of solar cells which resulted into power conversion efficiency of 2.8 %. On the other hand, the solar cells built on glass substrates gave a typical FF of 23 % and power conversion efficiency of 1.9 %.

5.2 Further Work

The work described in the preceding chapters is only one step in the direction to optimize and design of operative bulk hetero-junction P3HT: PCBM based solar cells. Future work should put attention to reducing short circuits during the design of the cells. The presence of short circuits in any solar cell device reduces the size of short circuit current and open circuit voltage, and hence the overall efficiency of the cell. Careful deposition of the successive layers during cell fabrication is required in order to realize the full potential of these polymer blends. The active layers must also be kept thin in the orders of 70 to 300 nm. This is because of the high possibility of recombination of charge carriers in these disordered systems with the increase in thickness.

Future work should focus on understanding the morphology and phase changes in P3HT: PCBM blend ratios that occur during the temperature annealing process as well as the effect of these changes to photo-absorbance.

References

1. **Li Gang, Shrotriya Vishal, Yao Yan, et al.** *Manipulating regioregular poly(3-hexylthiophene): [6,6]-phenyl-C-61-butyric acid methyl ester blends - route towards high efficiency polymer solar cells.* s.l. : Journal of Materials Chemistry, 2007. Vol. 17, 30, pp. 3126-3140.
2. **S. E. Shaheen, C.J. Brabec, N. S. Sariciftci, J.C Hummelen.** *2.5% efficient organic plastic solar cells.* s.l. : Appl. Phys. Lett, 2001. Vol. 78, pp. 841-843.
3. **D. Chirvase, J.C. Parisi, J. M. Hummelen, V. Dyakonov.** *Influence of nanomorphology on the photovoltaic action of polymer-fullerene composites.* s.l. : Nanotechnology, 2004. Vol. 15, pp. 1317-1323.

4. **A. Usami, et al.** *Theoretical simulations of optical confinement in dye-sensitized nanocrystalline solar cells.* s.l. : Solar Energy Material & Solar Cells, 2000. Vol. 64, 1, pp. 73-83.
5. **D. Woehrle, D. Meissner.** *Organic solar cells.* s.l. : Advanced Materials, 1991. Vol. 3, p. 129 .
6. **W. Shockley, H. J. Queisser.** *Detailed balance limit of efficiency of P N junction solar cells.* s.l. : J. Appl .Phys., 1961. Vol. 32, p. 510.
7. **N. S. Sariciftci, L. Smilowitz, A. J. Heeger, F. Wudl.** *Photoinduced Electron Transfer from a Conducting Polymer to Buckminsterfullerene.* s.l. : Science, 1992. Vol. 258, pp. 1474-1476.
8. **N. Camamaioni, G. Gidolfi, G. C. Miceli, G. Possamai.** *The effect of a mild thermal treatment on the performance of polymer-fullerene solar cells.* s.l. : Adv. Mater., 2004. Vol. 15, p. 288.
9. **Thomas Wellinger, et al.** *Efficiency Improvements of P3HT: PCBM Heterojunction Photovoltaic Cells.* s.l. : Light Technology Institute Department of Electrical Engineering and Information Technology Universität Karlsruhe (TH), 2005.
10. **S. M. Sze, et al.** *Physics of Semiconductor Devices, Second Edition.* 1981. pp. 792-793.
11. **Rafael Martin Lamaison, et al.** *Photovoltaic Solar Energy (ESF).* s.l. : Universitat Politècnica de Catalunya, 2004. pp. 1-11.
12. **C. J. Brabec, N. S. Sariciftci, J. C. Hummelen.** *Plastic Solar Cells.* s.l. : Adv. Funct. Mater., 2001. Vol. 11, pp. 15-26.
13. **M. Zeilik, E. V. P. Smith.** *Introductory: Astronomy and Astrophysics.* s.l. : CBS College Publishing, 1987. 2nd Edition.
14. **M. Granstrom, P. Klaus.** *multilayer photo-voltaic or photoconductive devices.* s.l. : Australia Patent Nr.: AU2433799A1, 02 Febr. 1999.
15. **M. Niggemann, B. Bl.asi, A. Gombert, A. Hinsch, H. Hoppe, P. Lalanne, D. Meissner, V. Wittwer.** *Trapping light in organic plastic solar cells with integrated diffraction gratings.* Munich, Germany : 17th European Photovoltaic Solar Energy Conference, 2001.
16. **M. A. Green, et al.** *Solar Cells - Operating Principles ,Technology and System Applications.* Kensington : University of New South Wales, 1992.

17. **D. Adam, F. Closs, T. Frey, D. Funhoff, D. Haarer, H. Ringsdorf, P. Schuhmacher and K. Siemensmeyer.** *Transient photoconductivity in a discotic liquid crystal.* s.l. : Phys. Rev. Lett., 1993. Vol. 70, pp. 457-460 .
18. **P. Klaus, et al.** *Organic Solar Cells Architectures.* s.l. : Technisch-Naturwissenschaftliche Fakultat der Technischen Universit¨at Graz (Austria), Cambridge and Graz, July 2000.
19. **Osamu Yoshikawa, Akinobu Hayakawa, Takuya Fujieda.** *Enhanced Efficiency and Stability in P3HT: PCBM Bulk Heterojunction Solar Cell by using TiO2 Hole Blocking Layer.* Uji, Kyoto, Japan : Institute of Advanced, Kyoto University, 2007. Vol. 965, pp. 611-0011.
20. **Lambert Jan Anton Koster, et al.** *Device physics of donor-acceptor/blend solar cells.* University of Groningen, The Netherlands : Dutch Polymer Institute (DPI), 2007. pp. 1-109. ISSN 1570-1530.
21. **C. Kim, J. W. Garland, H. Abad, P.M. Raccah.** *Modeling the optical dielectric function of semiconductors: Extension of the critical-point parabolic-band approximation.* s.l. : Phys. Rev. B, 1992. Vol. 45, 20, pp. 11749-11764.
22. **Y. M. M. Makame, and A. B. Malisa.** *Polymer Science.* University of Dar-es- Salaam, Tanzania : Ninth College on Thin Film Technology, 2006. Vol. 9.3.
23. **P. M. Borsenberger, et al.** *Hole transport in tri-p-tolylamine-doped bisphenol-A-polycarbonate.* s.l. : J. Appl. Phys., 1990. Vol. 68, p. 6263.
24. **W. D. Gill, et al.** *Drift mobilities in amorphous charge-transfer complexes of trinitrofluorenone and poly-n-vinylcarbazole.* s.l. : J. Appl. Phys., 1972. Vol. 43, p. 5033.
25. **G. Yu, J. Gao, J. C. Hummelen, F. Wudl, and A. J. Heeger.** *Polymer photovoltaic cells: enhanced efficiencies via a network of internal donor-acceptor heterojunctions.* s.l. : Science, 1995. Vol. 270, pp. 1789–1791.
26. **Eduard Johannes Meijer, et al.** *Charge transport in disordered organic field-effect transistors.* Netherlands : Delft University of Technology, 20 June 2003. pp. 1-132. ISBN 90-6734-306-4.

27. **P. A. Lane, J. Rostalski, C. Giebeler, S. J. Martin, D. D. C. Bradley, D. Meissner.** *Electroabsorption studies of phthalocyanine/perylene solar cells.* 15 June 2000. Vol. 63, 1, pp. 3-13.
28. **K. C. Kao, and W. Hwang.** *Electrical transport in solids with particular reference to organic semiconductors.* Oxford : Pergamon Press, 1981. p. xx + 663.
29. **F. Rowlands, J. Livingstone, C.P. Lund.** *Optical modeling of finely textured amorphous silicon solar cells.* s.l. : Sol. Energy Mater. Sol. Cells, 15 Feb. 2002. Vol. 71, 3, pp. 399-405.
30. **R. H. Friend, G. J. Denton, J. J. M. Halls, N. T. Harrison, A. B. Holmes, A. Koehler, A. Lux, S. C. Moratti, K. Pichler, N. Tessler and K. Towns.** *Electronic processes of conjugated polymers in semiconductor device structures.* s.l. : Synth.Met., 1997. Vol. 84, pp. 463-470.
31. **R. Brendel, and D. Scholten, et al.** *Modeling light trapping and electronic transport of waffle-shaped crystalline thin-film Si solar cells : Thin film solar cells.* s.l. : Appl. Phys. A, 1999. Vol. 69, pp. 201-213.
32. **H. Hoppe, M. Drees, W. Schwinger, F. Schaffler, N. S. Sariciftci** s.l. : Synth. Met., 2005. Vol. 152, p. 117.
33. **I. Elfallal, R. D. Rilkington, A. E. Hill.** *Formation of a statistical thermodynamic model for the electron concentration in heavily doped metal oxide semiconductors applied to the tin-doped indium oxide system.* s.l. : Thin solid films, Feb. 1993. Vol. 223, pp. 303-310.
34. **B. Sopori, J. Madjdpour, Yi-Zhang, Wei-Chen.** *PV optics: an optical modeling tool for solar cell and module design.* Pennington, NJ : Electrochemical Society Proceedings, 1999. Vol. 138, pp. 99–101.
35. **D. H. Dunlap, P. E. Parris, and V. M. Kenkre.** s.l. : Phys. Rev. Lett., 1996. Vol. 77, p. 542.
36. **S. V. Novikov, D.H. Dunlap, V.M. Kenkre, P. E. Parris, and A. V. Vannikov.** s.l. : Phys. Rev. Lett., 1998. Vol. 81.
37. **C. Tanase, E. J. Meijer, P. W. M. Blom, and D. M. de Leeuw.** s.l. : Phys. Rev. Lett. , 2003. Vol. 91, p. 216601.
38. **C. Tanase, P. W. M. Blom, and D. M. de Leeuw.** s.l. : Phys. Rev. Lett., 2004. Vol. 70, p. 193202.

39. **W. F. Pasveer, J. Cottaar, C. Tanase, R. Coehoorn, P. A. Bobbert, P. W. M. Blom, D.M. de Leeuw and M. A. J. Michels.** s.l. : Phys. Rev. Lett. , 2005. Vol. 94, p. 206601.

40. **J. Yamashita, and T. Kurosawa.** s.l. : J. Phys. Chem., 1958. Vol. Solids 5, p. 34 .

41. **Kwanghee Lee, et al.** *Fabrication optimization improves thermal stability and efficiency of polymer solar cells.* Center for Polymers and Organic Solids, University of California at Santa Barbara, Santa Barbara, CA : SPIE Let., 2006. pp. 1-2.

42. **M. Zeman, R. A. C. M. M. van Swaaij, M. Zuiddam, J.W. Metselaar, R. E. I Schropp.** *Sol. Energy Mater. Sol. Cells.* 2001. Vol. 66, p. 353.

43. **M. Zeman, R. A. C. M. M. van Swaaij, J.W. Metselaar, R.E.I. Schropp.** s.l. : J. Appl. Phys., 2000. Vol. 88, p. 6436.

44. **F. Padinger, Rittberger R.S., Sariciftci N.S.** s.l. : Adv. Funct. Mater., 2003. Vol. 13, 1, pp. 85-88.

45. **A. R. Brown, C.P. Jarrett, D.M. de Leeuw, and M. Matters.** s.l. : Synth. Met. , 1997. Vol. 88, p. 37 .

46. **Ge Weihao, et al.** *An overview on P3HT:PCBM, the most efficient organic solar.* UTK : s.n., 2009. pp. 1-11.

47. **Juan Bisquert, Germà Garcia-Belmonte, Antoni Munar, Michele Sessolo, Alejandra Soriano, Henk J. Bolink.** *Band unpinning and photovoltaic model for P3HT:PCBM organic bulk heterojunctions under illumination.* s.l. : Chemical Physics Letters, 2008. Vol. 465, pp. 57–62.

48. **Harald Hoppe, and N. Serder Sariciftci** *Polymer Solar Cells.* Technical University of Ilmenau, Germany : Institute of Physics, Experimental Physics I, 2007.

49. **Thomas Moehl, Vladimir G. Kytin, Juan Bisquert, et al.** *Relaxation of Photogenerated Carriers in P3HT:PCBM Organic Blends.* s.l. : ChemSusChem, 2009. Vol. 2, pp. 314 – 320.

50. **J. Moons, M. Eschle and M. Graetzel.** *Determination of the energy diagram of the dithioketopyrrole /SnO2:F heterojunction by surface photovoltage spectroscopy.* s.l. : Appl. Phys. Lett., 1997. Vol. 71, pp. 3305-3307.

51. **L. J. Rothberg, M. Yan, S. Son, M. E. Galvin, E. W. Kwock, et al.** *Intrinsinc and extrinsinc constraints on PPV electroluminescence.* s.l. : Synth.Met., 1996. Vol. 78, pp. 231-236 .
52. **H. J. Lewerenz, and H. Jungblut.** *Photovoltaic.* Berlin : Springer, 1995.
53. **M. Forster, K. O. Annan, and U. Scherf.** *Conjugated Ladder Polymers Containing Thienylene Units.* s.l. : Macromolecles, 1999. Vol. 32, p. 3159.
54. **Jung-Chul Park, et al.** *The removal of Tin from ITO-scrap Using Molten NaOH, Department of Engineering in Energy & Applied Chemistry.* s.l. : Silla University, Busan, Korea, 14 November 2008. Vol. 29, pp. 617-736.
55. **R. Robert Gotwals, et al.** *Visualizing the Vibrations of Water.* Durham, NC : the Shodor Center for Computational Science Education, 2002.
56. **John Coates, et al.** *Interpretation of Infrared Spectra, A Practical Approach.* Chichester : John Wiley and Sons Ltd, 2000.
57. **Vishal Shrotriya, Jianyong Ouyang, et al.** *Absorption spectra modification in poly (3-hexylthiophene): methanofullerene blend thin films.* s.l. : chemical physics letter, 2005. Vol. 411, pp. 138-143.
58. **A. M. Bobrova, and I. G. Zhigun.** *Infrared Absorption Spectra of various Titanium Compounds.* s.l. : chemical physics letter, 1968. Vol. 8, pp. 96-108.
59. **M. M. Hasan, et al.** *Effects of Annealing Treatment on Optical Properties of Anatase TiO2 Thin Films.* s.l. : University of Malaya, 2008.
60. **M. F. Zaki, et al.** *Gamma-Induced Modification on Optical Band Gap of CR-67 SSNTD .* s.l. : Experimental Nuclear Physics Department, Cairo, Egypt, 2008.
61. **Y. Meng, X. Yang, H. Chen, J. Shen, Z. Zhang, and Z. Hua.** s.l. : Thin Solid Film, 2001. Vol. 394, pp. 219–223.
62. **G. P. Joshi, et al.** *Band Gap Determination of Ni-Zn ferrites.* s.l. : University of Rajasthan, India, 2003.

APPENDIX A

The Spin Coating Method

The sol-gel process is a versatile solution process for making advanced materials, including ceramics and organic-inorganic hybrids. In general, the sol-gel process involves the transition of a solution system from a liquid "sol" (mostly colloidal) into a solid "gel" phase. Utilizing the sol-gel process, it is possible to fabricate advanced materials in a wide variety of forms: ultrafine or spherical shaped powders, thin film coatings, fibers, porous or dense materials, and extremely porous aerogel materials. The starting materials used in the preparation of the "sol" are usually inorganic metal salts or metal organic compounds such as metal alkoxides.

In a typical sol-gel process, the precursor is subjected to a series of hydrolysis and polymerization reactions to form a colloidal suspension, or a "sol". Further processing of the "sol" makes it possible to make materials in different forms. Durable thin films with a variety of properties can be deposited on a substrate by spin-coating. When the "sol" is cast into a mold, a "wet gel" will form. With further drying and heat treatment, the "gel" is converted into dense materials. If the liquid in a wet "gel" is extracted under a supercritical condition, a highly porous and extremely low-density material called "aerogel" is obtained.

As the viscosity of a "sol" is adjusted into a given viscosity range, fibers can be drawn from the "sol”

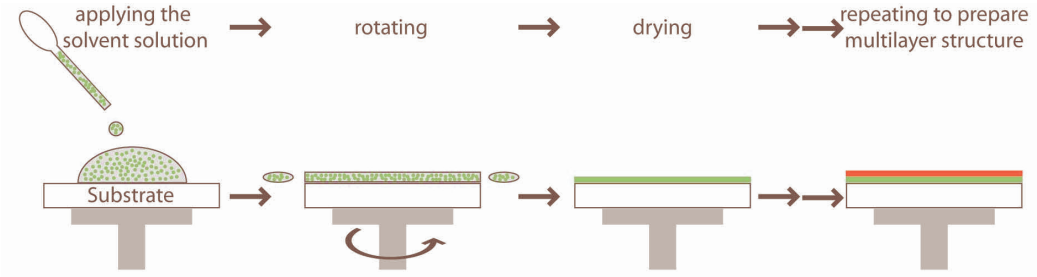


Figure A1: Before and after Centrifuging



Figure A2: The spin Coating unit at Chemistry department of the University of Zambia

In the spin coating process, the substrate spins around an axis which should be perpendicular to the coating area. The spin-on process has been developed for the so-called spin-on glasses in microelectronics and substrates with a rotational symmetry, for example in optical lenses such as eye glass lenses. The schematics are shown in Figure A1 and Figure A2 above.

The typical spin curve is shown in Figure A3. The dependence of the final thickness of a spin coated layer on the processing and materials parameters like angular velocity, viscosity and solvent evaporation rate by the semi-empirical formula is shown in Equation A1.

$$h = (1 - \rho_A / \rho_{A0}) \left(\frac{3\eta . m}{2\rho_{A0} . \omega^2} \right)^{1/3} \qquad \text{(A1)}$$

Where,

ρ_A =mass of volatile solvent per unit volume,

ρ_{Ao} = initial value of ρ_A,

h = final thickness,

η = viscosity,

ω = angular speed, and

m = evaporation rate of the solvent.

Since m has to be determined empirically any way, the more simple formula, given in Equation A2 may be used:

$$h = A.\omega^{-B} \qquad \text{(A2)}$$

where A and B are constants to be determined empirically. B is in the interval between 0.4 and 0.7, which is in rather good agreement with Equation (A1), where the exponent for ω is 0.67.

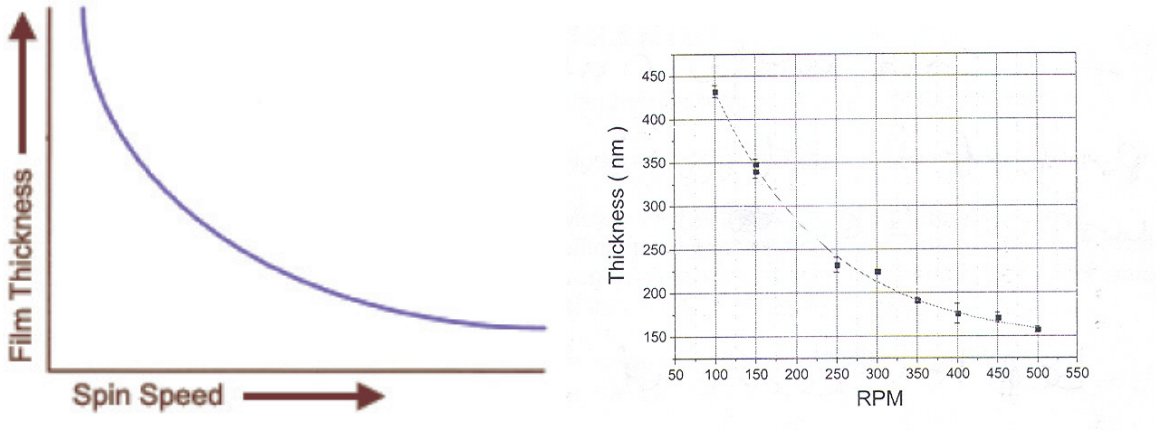
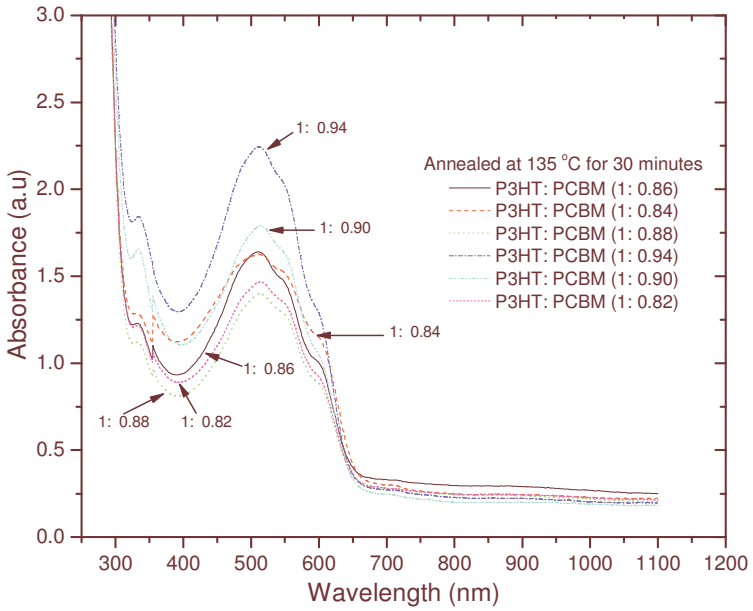
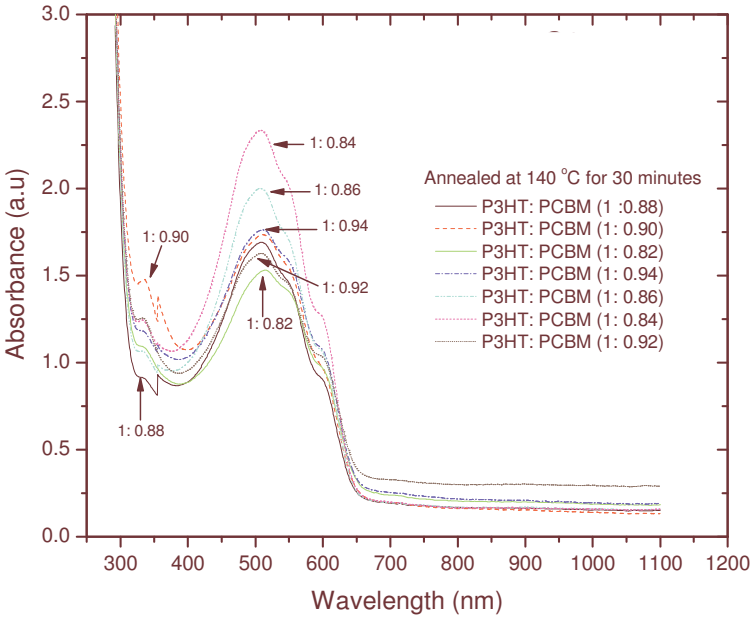


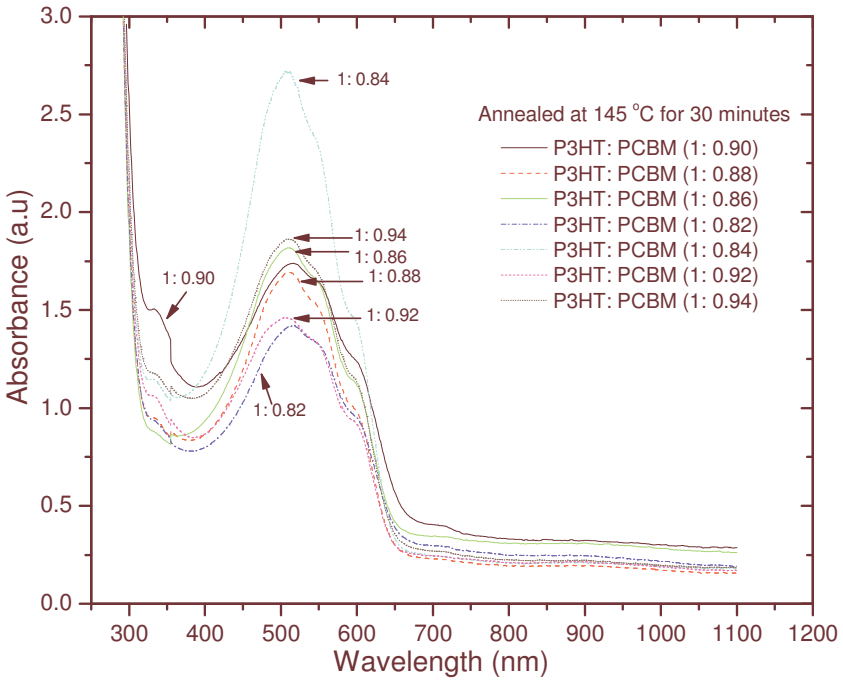
Figure A3: Typical spin curve solutions. The dependence of thickness on spin speed is exponential.

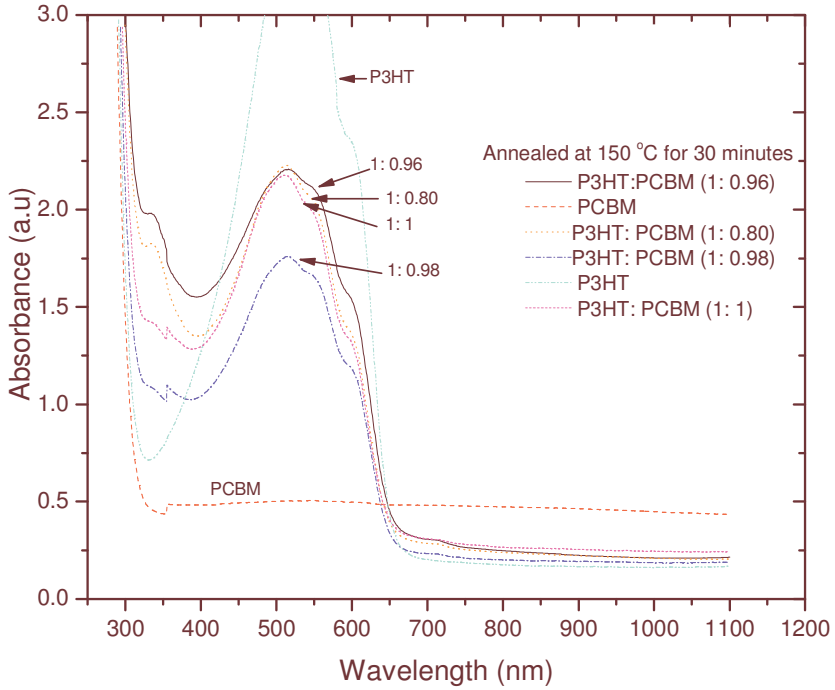
APPENDIX B

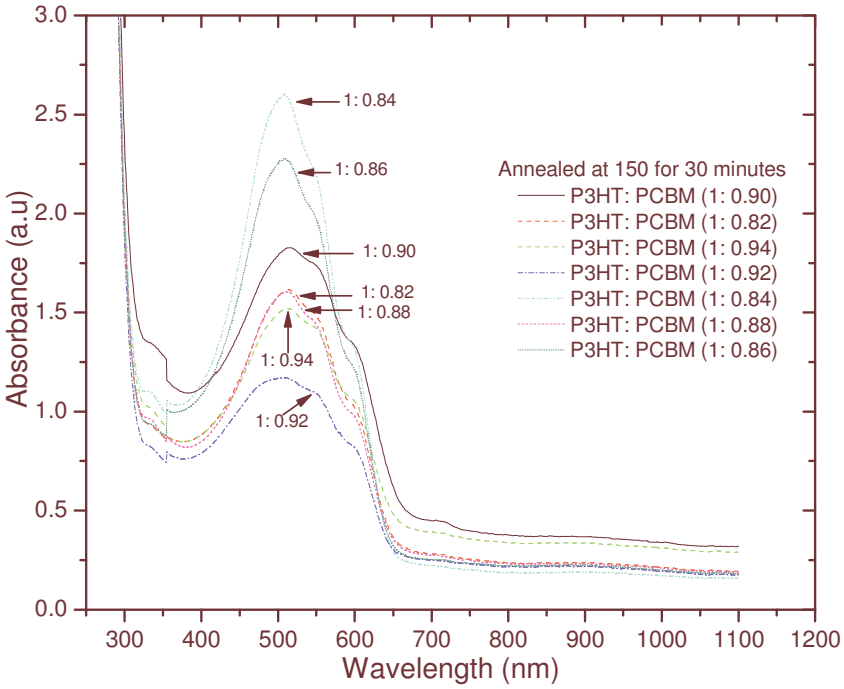
Photon Absorbance of various blends of P3HT: PCBM at different temperatures.

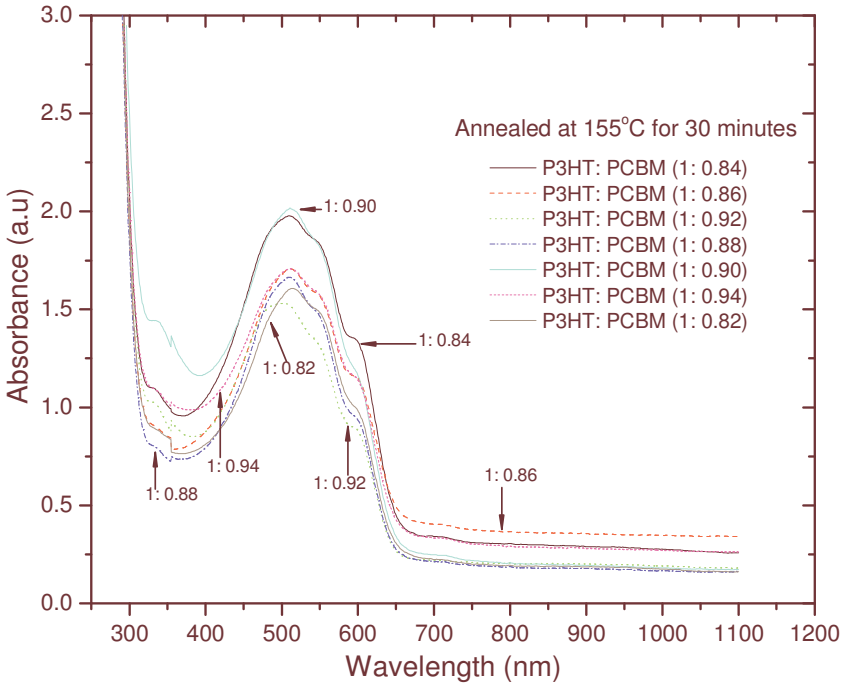


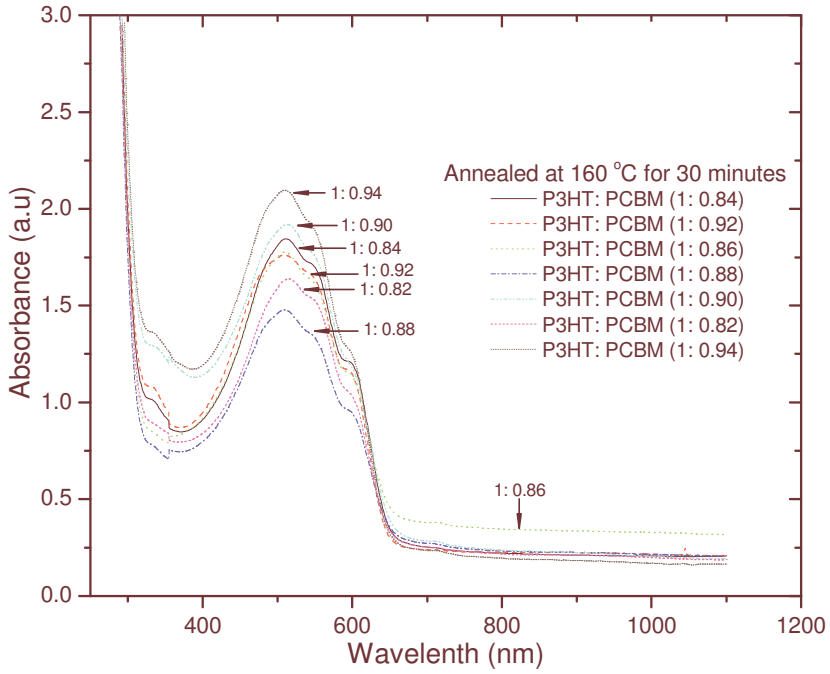


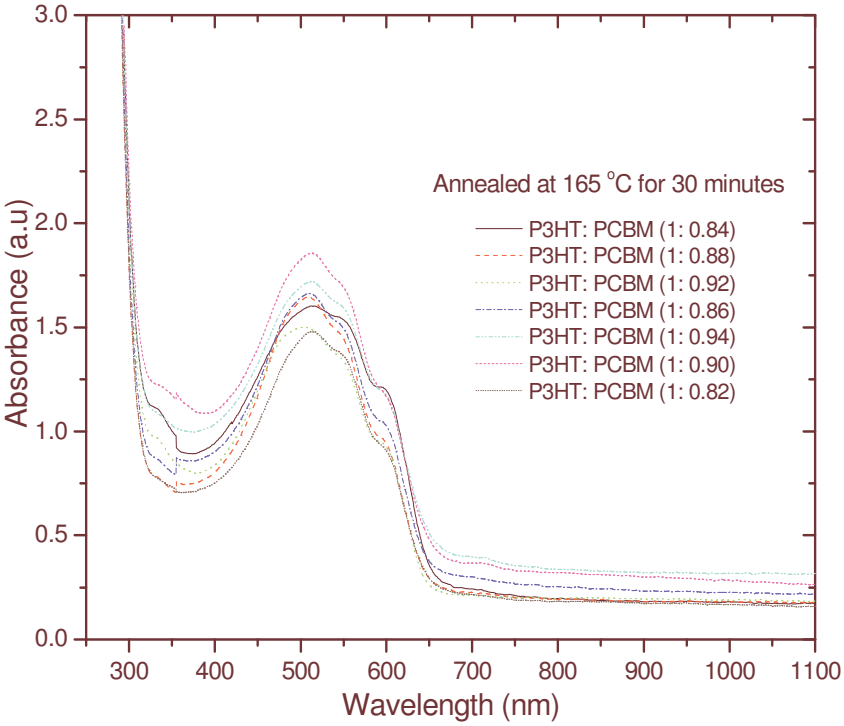

Absorbance (a.u)
Wavelength (nm)
Annealed at 145 °C for 30 minutes
P3HT: PCBM (1: 0.90)
P3HT: PCBM (1: 0.88)
P3HT: PCBM (1: 0.86)
P3HT: PCBM (1: 0.82)
P3HT: PCBM (1: 0.84)
P3HT: PCBM (1: 0.92)
P3HT: PCBM (1: 0.94)
1: 0.84
1: 0.94
1: 0.86
1: 0.88
1: 0.92
1: 0.90
1: 0.82


Absorbance (a.u)
Wavelength (nm)
Annealed at 150 °C for 30 minutes
P3HT:PCBM (1: 0.96)
PCBM
P3HT: PCBM (1: 0.80)
P3HT: PCBM (1: 0.98)
P3HT
P3HT: PCBM (1: 1)
P3HT
1: 0.96
1: 0.80
1: 1
1: 0.98
PCBM


Absorbance (a.u)
Wavelength (nm)
Annealed at 150 for 30 minutes
P3HT: PCBM (1: 0.90)
P3HT: PCBM (1: 0.82)
P3HT: PCBM (1: 0.94)
P3HT: PCBM (1: 0.92)
P3HT: PCBM (1: 0.84)
P3HT: PCBM (1: 0.88)
P3HT: PCBM (1: 0.86)
1: 0.84
1: 0.86
1: 0.90
1: 0.82
1: 0.88
1: 0.94
1: 0.92


Absorbance (a.u)
Wavelength (nm)
Annealed at 155°C for 30 minutes
P3HT: PCBM (1: 0.84)
P3HT: PCBM (1: 0.86)
P3HT: PCBM (1: 0.92)
P3HT: PCBM (1: 0.88)
P3HT: PCBM (1: 0.90)
P3HT: PCBM (1: 0.94)
P3HT: PCBM (1: 0.82)
1: 0.90
1: 0.84
1: 0.82
1: 0.94
1: 0.88
1: 0.92
1: 0.86


Annealed at 160 °C for 30 minutes
P3HT: PCBM (1: 0.84)
P3HT: PCBM (1: 0.92)
P3HT: PCBM (1: 0.86)
P3HT: PCBM (1: 0.88)
P3HT: PCBM (1: 0.90)
P3HT: PCBM (1: 0.82)
P3HT: PCBM (1: 0.94)
1: 0.94
1: 0.90
1: 0.84
1: 0.92
1: 0.82
1: 0.88
1: 0.86
Absorbance (a.u)
Wavelenth (nm)


Annealed at 165 °C for 30 minutes
P3HT: PCBM (1: 0.84)
P3HT: PCBM (1: 0.88)
P3HT: PCBM (1: 0.92)
P3HT: PCBM (1: 0.86)
P3HT: PCBM (1: 0.94)
P3HT: PCBM (1: 0.90)
P3HT: PCBM (1: 0.82)
Absorbance (a.u)
Wavelength (nm)